

**DESIGN OF ROBOTIC PLATFORMS TO MODEL CONFINED ACTIVE  
MATTERS**

A Thesis  
Presented to  
The Academic Faculty

By

Ross J. Warkentin

In Partial Fulfillment  
of the Requirements for the Degree  
Master of Science in the  
School of Mechanical Engineering

Georgia Institute of Technology

December 2017

Copyright © Ross J. Warkentin 2017

**DESIGN OF ROBOTIC PLATFORMS TO MODEL CONFINED ACTIVE  
MATTERS**

Approved by:

Dr. Daniel Goldman, Advisor  
School of Physics  
*Georgia Institute of Technology*

Dr. David Hu, Committee Co-Chair  
Woodruff School of Mechanical  
Engineering  
*Georgia Institute of Technology*

Dr. Magnus Egerstedt  
School of Electrical and Computer  
Engineering  
*Georgia Institute of Technology*

Date Approved: July 24, 2017

Don't look for the big, quick improvement. Seek the small improvement one day at a time. That's the only way it happens—and when it happens, it lasts.

*John Wooden*

*To friends and family*

## ACKNOWLEDGEMENTS

I have been fortunate enough to have fallen into a wonderful position at Georgia Tech, surrounded by insightful, intelligent, and supportive peers and mentors that have inspired me in my time here. I would like to thank Professor Daniel Goldman for his guidance and mentorship over the course of this thesis research, as well as Professor Magnus Egerstedt and Professor David Hu for their time spent on the thesis reading committee. I would also like to thank Professor Dana Randall from the Georgia Tech School of Mathematics and Professor Andrea Richa from Arizona State University for their collaboration on the supersmarticle research.

I am incredibly grateful to the fantastic members of the CRABLab, for their energizing tenacity and seemingly unbounded curiosity. A special thanks is extended to Will Savoie, Xiaobin Xiong, Shengkai Li, Bahnisikha Dutta, Christian Hubicki, Jennier Reiser, and Jeff Aguilar for their assistance and discussions regarding the various projects I have had the privilege of working on. I would also like to thank Daniel Soto for his help in designing the next iteration of the ant robots, and Shea Wells for his numerous contributions to the smarticle projects.

## TABLE OF CONTENTS

<b>Acknowledgements</b> . . . . .	v
<b>List of Tables</b> . . . . .	xii
<b>List of Figures</b> . . . . .	xiii
<b>Chapter 1: Introduction</b> . . . . .	1
1.1 Robophysics and Robotic Active Matter . . . . .	1
1.2 Objectives . . . . .	2
1.3 Background and Previous Work . . . . .	4
1.3.1 Robotic Ants . . . . .	4
1.3.2 Granular and Active Materials . . . . .	5
<b>I Robotic Ants</b>	<b>8</b>
<b>Chapter 2: Robotic Ant System Overview</b> . . . . .	9
2.1 Design Parameters . . . . .	10
2.1.1 Safety . . . . .	10
2.1.2 Autonomy . . . . .	11
2.1.3 Robustness . . . . .	11
2.1.4 Durability . . . . .	12

2.1.5	Scalability . . . . .	12
2.1.6	Maintainability and Availability . . . . .	13
2.1.7	Testability . . . . .	13
2.2	Test Bed Design . . . . .	14
2.2.1	Tunnel Geometry . . . . .	14
2.2.2	Excavated Material . . . . .	15
<b>Chapter 3: Robotic Ant Electrical Design . . . . .</b>		<b>18</b>
3.1	Microcontroller . . . . .	18
3.2	Sensors . . . . .	20
3.2.1	Pheromone Trail Detector . . . . .	20
3.2.2	Navigation . . . . .	22
3.2.3	Gripper Sensors . . . . .	27
3.2.4	Charging and Deposit Site Detector . . . . .	31
3.2.5	Digging Site Detect . . . . .	31
3.2.6	Power Consumption . . . . .	32
3.2.7	Physical Contact Sensors . . . . .	32
3.2.8	Sensor Summary . . . . .	33
3.3	Actuators . . . . .	34
3.3.1	Servo Motors . . . . .	34
3.3.2	Drive Motors . . . . .	34
3.4	Circuitry . . . . .	35
3.4.1	Power Board . . . . .	36

3.4.2	Central Electronics Board . . . . .	37
3.4.3	Anterior Sensor Board . . . . .	39
3.4.4	Battery Selection . . . . .	39
<b>Chapter 4:</b>	<b>Robotic Ant Mechanical Design . . . . .</b>	<b>45</b>
4.1	Design Approach . . . . .	45
4.2	Computer-Aided Design Overview . . . . .	46
4.3	Assembled Robot . . . . .	53
<b>Chapter 5:</b>	<b>Robotic Ant Software Design . . . . .</b>	<b>58</b>
5.1	Arduino Due . . . . .	58
5.2	Pixy Camera Supporting Software . . . . .	71
5.3	MATLAB Vision Tracking System . . . . .	72
<b>Chapter 6:</b>	<b>Robotic Ants Results and Discussion . . . . .</b>	<b>73</b>
6.1	Observations . . . . .	73
6.1.1	Granular Media Manipulation . . . . .	73
6.1.2	Navigation . . . . .	75
6.1.3	Precision . . . . .	76
6.1.4	Robot Interactions . . . . .	76
6.1.5	Processing Capability . . . . .	77
6.2	Preliminary Data . . . . .	77
6.3	Conclusions and Future Works . . . . .	78

<b>II Smart Particles — <i>Smarticles</i></b>	<b>85</b>
<b>Chapter 7: Smarticle System Overview</b>	<b>86</b>
7.1 Design Parameters	86
7.1.1 Safety	86
7.1.2 Form Factor	86
7.1.3 Autonomy and Control	87
7.1.4 Robustness	87
7.1.5 Durability	88
7.1.6 Scalability	88
7.1.7 Maintainability and Availability	89
7.2 Smarticle Ensemble	89
7.3 Test Bed Design	92
<b>Chapter 8: Smarticle Electrical Design</b>	<b>94</b>
8.1 Microcontroller	94
8.2 Sensors	94
8.2.1 Interoceptive Sensors	95
8.2.2 Exteroceptive Sensors	95
8.2.3 Sensor Summary	96
8.3 Actuators	96
8.3.1 Servo Motors	97
8.4 Circuitry	99
8.4.1 Main Board	99

8.4.2	Battery Selection . . . . .	99
8.5	Electrical Design Conclusion . . . . .	100
<b>Chapter 9:</b>	<b>Smarticle Mechanical Design . . . . .</b>	<b>103</b>
9.1	Design Approach . . . . .	103
9.1.1	Smarticle Case Design . . . . .	103
9.2	Assembled Smarticles . . . . .	109
<b>Chapter 10:</b>	<b>Smarticle Software Design . . . . .</b>	<b>112</b>
10.1	Design Approach . . . . .	112
10.2	Arduino Pro Mini Code . . . . .	112
10.3	OptiTrack . . . . .	115
10.4	msdalyzer . . . . .	115
<b>Chapter 11:</b>	<b>Smarticle Research Methods . . . . .</b>	<b>117</b>
11.1	Light-Based Experiments . . . . .	117
11.1.1	Manually Controlled System . . . . .	118
11.1.2	Light Pipe Controlled System . . . . .	118
11.2	Sound-Based Experiments . . . . .	118
<b>Chapter 12:</b>	<b>Smarticle Results and Discussion . . . . .</b>	<b>122</b>
12.1	Flat Smarticles Controlled by Light . . . . .	123
12.2	Light Pipes Smarticles Controlled by Light . . . . .	123
12.3	Light Pipe Smarticles Controlled by Sound . . . . .	130
12.4	Flat Smarticles Controlled by Sound . . . . .	131

12.5 Conclusions and Future Works . . . . . 134

**Appendix A: Robotic Ant Minimum Parts List . . . . . 138**

**Appendix B: Smarticle Minimum Parts List . . . . . 139**

**References . . . . . 140**

## LIST OF TABLES

3.1	Summary of Robotic Ant Sensors . . . . .	34
5.1	Summary of Robotic Ant States . . . . .	60
8.1	Summary of Smarticle Sensors . . . . .	96
12.1	Comparison of Experimental Results . . . . .	131

## LIST OF FIGURES

1.1	Assembled flat smarticle front view . . . . .	6
1.2	Inspiration for the smarticles . . . . .	7
2.1	Top-down view of tunnel setup . . . . .	14
2.2	Charging station setup . . . . .	16
2.3	Magnetic granular material . . . . .	17
3.1	Standard voltage divider schematic . . . . .	19
3.2	Raw Pixy camera perspective of digging site prior to filtering . . . . .	22
3.3	Pixy camera perspective of digging site after filtering . . . . .	23
3.4	Raw heading readings prior to calibration. . . . .	26
3.5	Visualization of calibration results for IMU 1 . . . . .	28
3.6	Visualization of calibration results for IMU 2 . . . . .	29
3.7	Visualization of calibration results for IMU 3 . . . . .	29
3.8	Visualization of calibration results for IMU 4 . . . . .	30
3.9	Visualization of calibration results for IMU 5 . . . . .	30
3.10	Capacitive sensor materials . . . . .	33
3.11	Power Board schematic . . . . .	41
3.12	Assembled Power Board . . . . .	42

3.13 Central Electronics Board schematic . . . . .	43
3.14 Assembled Central Electronics Board . . . . .	43
3.15 Anterior Sensor Board schematic . . . . .	44
3.16 Assembled Anterior Sensor Board . . . . .	44
4.1 Ant robot isometric view . . . . .	47
4.2 Ant robot front view . . . . .	48
4.3 Ant robot side view . . . . .	49
4.4 Exploded view of electronics scaffolding . . . . .	51
4.5 Exploded view of motor and caster mount assembly . . . . .	52
4.6 Exploded view of gripper assembly . . . . .	54
4.7 Assembled robot from the front . . . . .	55
4.8 Assembled robot from the side . . . . .	56
4.9 Assembled robot from the back . . . . .	57
5.1 Overview of robot ant state machine modes and transitions . . . . .	59
5.2 Overview of robot ant <code>setup()</code> . . . . .	62
5.3 Overview of robot ant <code>loop()</code> . . . . .	63
5.4 Overview of <code>goingInMode()</code> . . . . .	64
5.5 Overview of <code>diggingMode()</code> . . . . .	65
5.6 Overview of <code>exitTunnelMode()</code> . . . . .	66
5.7 Overview of <code>goingOutMode()</code> . . . . .	67
5.8 Overview of <code>turnHeading()</code> . . . . .	68
5.9 Overview of <code>depositMode()</code> . . . . .	69

5.10 Overview of <code>restMode()</code> . . . . .	70
5.11 Example of the Hough transform image processing . . . . .	72
6.1 Current drawn by two robots over the course of a trial . . . . .	78
6.2 Battery voltage of two robots over the course of a trial . . . . .	79
6.3 Instantaneous power consumption of two robots over the course of a trial . . . . .	80
6.4 Space-time diagrams for ensembles of eager robots which always participate in excavation . . . . .	82
6.5 Isometric view of new robotic ant platform with C-shaped legs . . . . .	83
6.6 Side view of new robotic ant platform with C-shaped legs . . . . .	83
6.7 Top-down view of new robotic ant platform with C-shaped legs . . . . .	84
7.1 Five smarticle ring . . . . .	90
7.2 Four smarticle ring . . . . .	91
7.3 Components of the kinematic mount . . . . .	93
8.1 Square gait joint space trajectory traced by smarticle . . . . .	98
8.2 Smarticle electronics schematic . . . . .	101
8.3 Top-down view of the smarticle assembled electronics board . . . . .	102
9.1 Angle of incidence test setup . . . . .	105
9.2 Light sensor readings as a function of angle of incidence at varying distances from the light source . . . . .	105
9.3 Light sensor readings for the new smarticle case as a function of angle of incidence at varying distances from the light source . . . . .	106
9.4 Isometric view comparison of two smarticle cases . . . . .	107
9.5 Front view comparison of two smarticle cases . . . . .	107

9.6	Top view comparison of two smarticle cases . . . . .	107
9.7	Isometric view comparison of two smarticle cases . . . . .	108
9.8	Front view comparison of two smarticle cases . . . . .	108
9.9	Top view comparison of two smarticle cases . . . . .	108
9.10	CAD model of assembled light pipe smarticle, isometric view . . . . .	109
9.11	Exploded assembly of light pipe smarticle . . . . .	110
9.12	Assembled flat smarticle front view . . . . .	110
9.13	Assembled flat smarticle back view . . . . .	111
10.1	Overview of smarticle <code>setup()</code> . . . . .	113
10.2	Overview of smarticle <code>light-controlledloop()</code> . . . . .	114
10.3	Overview of smarticle <code>sound-controlled loop()</code> . . . . .	115
11.1	Top-down view of the test bed set up for light bar tests . . . . .	119
11.2	Moving from the world frame to the smarticle frame . . . . .	120
12.1	Displacement tracks for the unbiased trials with flat faced smarticles . . . . .	124
12.2	MSD plot for unbiased trials with flat faced smarticles . . . . .	125
12.3	MSD log-log plot for unbiased trials with flat faced smarticles . . . . .	126
12.4	Displacement tracks for the manually biased trials . . . . .	127
12.5	MSD plots for all manually biased trials . . . . .	128
12.6	MSD log-log plots for all manually biased trials . . . . .	129
12.7	Displacement tracks for the light bar biased trials with light source located at four different locations . . . . .	130

12.8 Displacement tracks for the sound biased trials with the initial position of  
the inactive smarticle at four different locations . . . . . 132

12.9 Corrected smarticle ring tracks in the frame of the inactive smarticle . . . . 133

## SUMMARY

The abstraction of agents acting in environments is a common method used to simplify and reduce complex systems into more manageable pieces to elucidate the physics which govern the original system behavior. Scientific abstractions can take on many forms, whether it be the mathematical neglect of friction or the development of a physical platform with which to draw analogies to another system. The subject of this thesis focuses on the development and use of robotic platforms which abstract two unique systems of active granular matter.

The first system is inspired by biological observations made while studying colonies of the species *Solenopsis invicta*, commonly known as the fire ant. Colonies of fire ants build shelters by excavating extensive tunnel networks underground, though not all members of the colony participate in this nest construction equally. The task of excavation performed by the colony can be thought of as an execution of a swarm algorithm accomplishing the task of material transport, which must address a number of issues at various scales within the system. The behaviors seen in fire ant colonies addresses the individual agent issues such as navigating in a dark, confined environment, while addressing the higher-level systematic coordination of sometimes thousands of agents without any centralization. Hypotheses have been developed, and robotic implementations have been tested in the lab which have probed the effects of heterogeneous behavior distributions within a task-oriented ensemble, though the capabilities of the robots were found to be somewhat limited. A new robotic model with improved navigation and sensory capabilities was needed to further investigate the aspects of the fire ant ensembles which may inform and govern the individual agent behaviors in order to optimize the collective operation.

The second system discussed concerns the field of active and granular materials more directly. While the field of granular matter has a rich literature, the realm of active granular materials, in which particles exhibit individual behaviors, is a subject which may prove

fruitful to a number of fields in the coming years. Granular media are often investigated in the standard context of spherical, convex particles, though atypical, nonconvex particles such as those studied presented in [1] are demonstrated to have interesting entanglement dynamics which demonstrate a rich and diverse physics which may be exploited by biological systems such as the social insect assemblies studied in [2].

This thesis is segmented into two parts, the first regarding the design of a new robotic ant platform and the second regarding the development of a sono- and photosensitive smart active matter system. Chapter 1 introduces the previous work related to both platforms and motivates the design and implementation of each robot, after which Part I begins with an outline of the robotic ant system and the design parameters in Chapter 2. Chapters 3, 4, and 5 detail the electrical, mechanical, and software design of the robotic ant platform and the supporting systems, followed by Chapter 6 which outlines observations, data, and conclusions drawn from the new platform. Similarly, Part II begins with an overview of the smart active particle system in Chapter 7, followed by a review of the electrical engineering methods in Chapter 8, the mechanical engineering methods in Chapter 9, and the software design in Chapter 10. Lastly, a review of the observations, data, conclusions, and future work for this second system are given in Chapter 12.

# CHAPTER 1

## INTRODUCTION

Collections of agents which can interact with their environment and one another can have numerous behaviors at the collective-scale which are emergent and not implicitly defined by the individual agent behaviors. P.W. Anderson captured this concept eloquently in his 1972 Science article *More is Different: Broken symmetry and the nature of the hierarchical structure of science*, in which he explores and decomposes the fallacy that the ability to reduce everything into its most fundamental equations implies the ability to then start from those same laws and in turn reconstruct the original system [3]. Insights from the reductionist approach to collective dynamics, in which the individual is studied in isolation, are incapable of capturing the rich physics of the conglomeration thereof. A different approach is necessary. Rather than pluck the complex agents from the environment to study them in vacuo, a different reduction is performed at the level of the agent within the system, such that the ensemble is maintained while the elements of the aggregate are more easily characterized.

### 1.1 Robophysics and Robotic Active Matter

Research into the fundamental principles which govern the movement of complex physical systems has significant importance in the context of robotics. Current technologies in the field of locomotion have yet to develop the efficient and robust navigation capabilities of biological organisms, particularly in heterogeneous environments characterized by uneven terrain and surfaces which can yield and flow. The study of the physics of these moving systems is necessary, particularly in the field of locomotion robophysics, in developing capable robotic platforms. The philosophy of this perspective allows the field of robotic engineering, tasked with developing complex systems capable of movement in generalized

environments, and the field of physics, which employs reductionist scientific studies in well-defined lab environments, to inform one another [4].

Biological swarms of individual organisms are capable of organizing in a variety of fashions, ranging from complex flocking behaviors to constructions of self-composed shelters [2, 5, 6]. However, in many of these systems any individual, plucked from the collective, would be incapable of expressing the behavior of the swarm.

The methodology of robophysics is relevant not only to the subject of locomotion, but also to the more general field of active matters. Swarms of robots can be considered as a task-oriented active matter, in which each particle of the aggregate behaves in such a way to accomplish a task on a scale well beyond that of any particular individual. Furthermore, the behavior of the ensemble need not be defined explicitly by the actions of the individual agents. The use of robophysics in the context of swarm robotics encourages the development and exploration of agents which are individually incapable of the globally defined task.

## **1.2 Objectives**

The first subject of this thesis is the redesign of robot platform to test hypotheses inspired by observations by members of CRABLab on workload distributions in biological fire ant colonies, which suggest that populations in which some ants infrequently excavate may be more efficient. The development of a robotic platform allows various behaviors to be implemented and executed in a deterministic fashion. The robophysical implementation of this task-oriented active material allows us to probe the system dynamics in response to changes in individual agent behaviors.

The second subject presented in this thesis studies a system of smart active particles, *smarticles*, which are incapable of direct communication and locomotion which ultimately can confer information and produce diffusive locomotion. Developing the aforementioned robust walking robots is an arduous task which requires a harmonious cooperation of many

engineering fields to operate well. However, another possible robophysical perspective approaches the issue of locomotion from a different direction. Rather than designing an excellent robotic locomotor, using well engineered and costly components, we ask: how does a poor locomotor move? One particular solution is given, in which an ensemble of robots which are devoid of any locomotion abilities are coordinated to produce biased locomotion.

Systems composed of smarticles represent a new type of active granular material ensemble which exhibit dynamics that individual robots within the system are incapable of performing. Furthermore, there is no hint in the individual behavior states which directs the movement of the overall system. The objective of this research was to investigate one particular behavior exhibited by these ensembles, biased diffusion.

Each individual smarticle is constructed in such a way that all actuation capabilities are restricted to a two-dimensional plane. As a result, smarticles placed on a surface parallel to the plane in which the robots actuate are unable to move in any direction; a single smarticle in this orientation is incapable of any sort of locomotion. When several smarticles are placed in a confined perimeter, with the perimeter free to move, the smarticle joint movements will push against the neighboring smarticles and the ring. These interactions produce small displacements of all of the components, which are forced to continuously interact with one another by the confining ring. In a frictionless environment, the net displacement of the system as a result of these interactions remains zero. However, in environments with frictional forces, these small displacements are asymmetric such that over a given period of time the overall ensemble can translate. In spite of the fact that no individual deterministic component of the system can move, the overall system is capable of stochastic locomotion. The design and methods to control this locomotion phenomena via external biases is given in Part II.

## 1.3 Background and Previous Work

### 1.3.1 Robotic Ants

The first system discussed will be relevant to the lab's previous research on the study of work load distributions in fire ant colonies. Previous investigations have been conducted to develop an understanding of the effect of unequal workload distributions and reversal behavior on overall system productivity. This research has been performed by intentionally manipulating and enforcing the distribution of labor among a population of simulated or robotic agents. While this subject was inspired by biological observations, the realizations from this research pertain to robotic swarm theory. This topic straddles two subjects of research in collective robotic systems: task allocation and interference. With regards to task allocation, a bulk of the literature focuses on centralized control and market-based task distribution, though some decentralized ant-emulating methods have been researched, with the most relevant work being presented in [7] and [8]. Both utilized activation threshold equations which enabled robots to determine behaviors based on various local inputs. However, these studies investigated the best way for systems to manage energy consumption in situations where energy must be expended to forage and find more energy sources. The focus of this literature was on local algorithms to manage energy consumption, while the research of CRABLab thus far is not concerned with the robotic control algorithm. Instead the intent of the research has been to identify the workload distribution that swarming robotic control algorithms such as those by Krieger et al. and Yang et al. should attempt to produce when engaged in high-interference transportation tasks [7, 8].

Physical interference in robot-dense systems has been explored in [9], which presents data similar to data collected within CRABLab for systems composed of many industrious robots competing for spatial resources. Many methods have been employed in literature to mitigate interference, such as workspace partitioning, or to at least reduce interference cost, such as the aggression interactions studied in [10]. However, interference management

has not been handled by intentionally modulating workload distribution. The agents in other interference-management papers perform varying tasks with equal engagement; the excavating fire ants in biological systems all perform the same task with varying rates of engagement.

Previous robotic ant iterations were sufficient to probe the initial hypotheses of workload distribution and reversal behaviors, but in order to further examine potential behavioral effects at play in these confined active matter systems a new robotic platform was developed with the intention of increasing the sensory and navigation capabilities of the robots while also increasing the mobility.

### 1.3.2 Granular and Active Materials

Systems of granular media are composed of macroscopic athermal particles, which exhibit dynamics which are dominated by contact interactions. Given this dependence on the contact interactions, the rheology of these systems is in turn governed by the geometries of the individual particles which comprise the media. Some granular materials are composed of aggregates which are capable of entanglement, which can result in conglomerations with solid and fluid-like properties. Gravish et al. present a studies in [1, 11] which examine the bulk properties of aggregations of "u"-shaped particles, seen in Figure 1.2(a).

Ensembles composed of nonconvex particles exhibit bulk rheological properties which are fundamentally governed by the ability of the particles to mechanically entangle. The geometries of the particles yields a form of cohesion induced by the interpenetration of particles within the ensemble. Aggregates of staples with varying length:width aspect ratios were studied in [1], though these particles were geometrically static; the interpenetrative properties of the nonconvex particles were constant with respect to time. In contrast, biological aggregates which exhibit entanglement have the ability to modulate individual particle geometries independently, yielding a more refined control over the bulk ensemble properties. Social insects such as ants, bees, and wasps utilize this control to produce com-

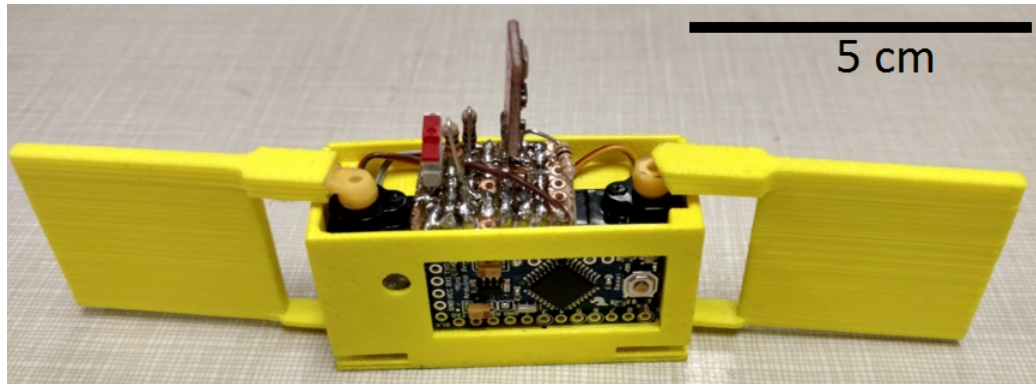
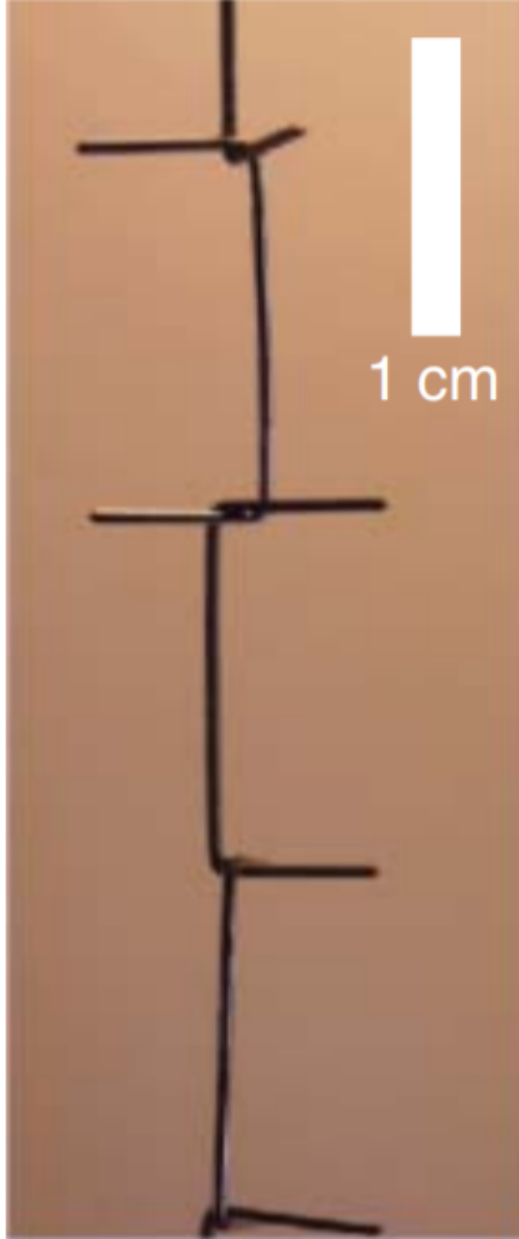


Figure 1.1: Assembled flat smarticle front view

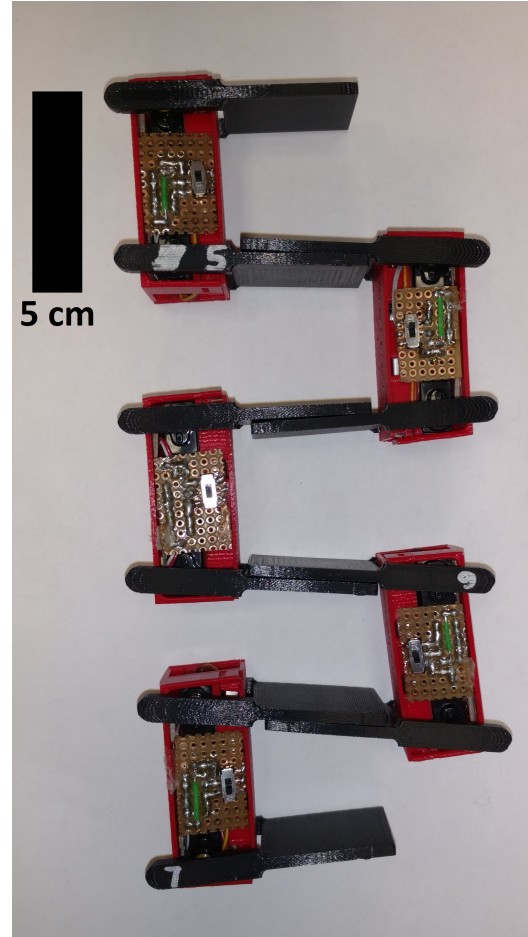
plex swarm self-assemblages of structures such as tunnels, walls, ladders, chains, and even bivouac shelters for other members of the colony [2].

Ensembles of active matters have been studied in the past, which includes colloidal solutions of self-propelled Janus particles [12] which exhibit random walks at long time scales, and even robotic platforms such as the macroscopic self-propelled bristle-bots studied in [13]. The internal diffusion dynamics have been the focus of these studies, though these systems, when the confining boundary is free to translate, also have interesting global dynamics on the scale of the entire ensemble.

To investigate an active granular material with the ability to actuate and sense, a system of robotic smart particles, hereby called *smarticles*, were developed, seen in Figure 1.1. Each smarticle is composed of a microcontroller, several sensors, and two servos which actuate about parallel axes. The original goal for the smarticle platform was to target agglomerations of smart active particles which can modulate their aspect ratio by modifying the angles of servo joint angles, thereby changing the length:width aspect ratios and the collective material properties. The smarticle platform has been used to demonstrate a number of interesting ensemble phenomenon, each of which hinge on a common theme: More is not more. More is different. The system is not the individual, and the sum of the individuals is not the linear compounding of each agent's actions. [3].



(a)



(b)

Figure 1.2: Particular smarticle configurations can be implemented to geometrically emulate the joint configurations of the "u"-shaped particles (a) from [11], which inspired the development of the programmable active material (b)

# **Part I**

## **Robotic Ants**

## **CHAPTER 2**

### **ROBOTIC ANT SYSTEM OVERVIEW**

Robophysical studies of scavenging and material transport tasks in the context of confined environments address the previously unstudied dynamics of systems which are environmentally constrained. Studies which parallel the material transport tasks conducted by ant colonies will be useful to elicit the dynamics of systems which have the potential to be fully saturated by agents. The robotic ant system was designed to geometrically represent the spatial interference problem from an active matter perspective with the intended goal of efficiently transporting material from one end of the tunnel to the opposite end while managing with task-disrupting factors, such as spatial constraints and difficulties associated with manipulating the excavated material. To enforce these interactions, the geometries of the robots and the operating environment were informed by the ratios observed in nature, in which the average tunnel diameter is approximately 1 body length, with ant body lengths being approximately 2 body widths [14].

The robotic model of the ant organism was designed to capture the group dynamics present in social insect swarms which are believed to accomplish tasks on the global scale without omniscient, centralized controllers governing and coordinating all agents. These systems operate without the benefit of complex path planning algorithms or any sense of globally coordination directions; we aim to capture the consequential group dynamics which emerge from ensembles of individuals operating without comprehensive information about the work space. To study these systems, a collection of homogeneous robots was programmed with behavior algorithms which govern the actions of the individual robots based on simple rules given locally observed states such as vision and contact inputs.

The development of the robotic ant system is built upon lessons learned in the design of a previous generation of robotic ants which were used to perform preliminary studies

[15]. Meticulous improvements in the mechanical, electrical, and software components of the robots were made to the platforms to fulfill the design parameters outlined below.

## **2.1 Design Parameters**

A number of requirements were established in the process of designing the next iteration of the robotic ant platform. Previous design parameters, such as safety, autonomy, robustness, durability, and scalability remained at the core of the design process, while additional considerations were made in terms of maintainability, availability, and testability.

### 2.1.1 Safety

The robotic platform was designed to operate without human intervention, though maintenance and experiment preparation would often require a significant amount of human interaction. Therefore, it was important to consider the various aspects of the electromechanical systems and the driving software to ensure that humans would be safe while operating on the robots.

Mechanically, the robot was designed without sharp edges, and all actuators such as servos and motors were geared such that the implementations were incapable of applying excessive forces which may clamp or pinch prior to stalling.

The electrical circuitry was designed such that all components were well within their operating ranges and all connections were isolated with electrical tape and heat shrink wrap to prevent electrical shorts from occurring. Additionally, a single-pole, single-throw (SPST) mechanical emergency shutoff switch was included prominently on the robot case far from electromechanical elements which could be accessed in the event of an emergency to directly cut power to all robot circuitry. The emergency shutoff switch effectively isolates the power supply and the associated charging circuitry from the electrical connections which drive the microcontrollers and mechanical actuators.

### 2.1.2 Autonomy

To capture the issues of collective task completion in the context of agents which are incapable of global coordination, the robots were designed to run software uploaded to a microcontroller with tunable parameters. The implemented software would follow behaviors according to a finite state machine which would be traversed based solely on locally observed states from onboard sensors. Given these restrictions in data availability, the robot platform was required to have a sufficient amount of sensors so that it can be programmed to perform social excavation activities autonomously. All actions and decisions made by the robot are based on the individual robot's own perception of the environment. The finite state machine was designed to capture the various states that a biological ant may operate under while excavating, such as moving towards the excavation site, grasping tunnel material, coordinating a reversal from the excavation site, moving towards the deposit site, and depositing, as well as other non-digging behaviors such as moderating energy expenditure and opting to rest and recharge. The composition of sensory capabilities and software states enable the robotic platform to exhibit a variety of artificial and biologically-inspired social digging behaviors without any external input commands from a human operator or any sort of overarching system controller.

### 2.1.3 Robustness

The primary mechanism the robot has for detecting obstacles are a set of contact sensors located along the perimeter of the robot shell. Robots regularly bumped into other robots as well as the walls of the tunnel. Additionally, robots regularly attempted to dig at the excavation site and instead grasp components of other nearby robots. It was important to consider the ability of the robotic platform to withstand such interactions without disrupting normal operations. Evidence of these considerations regarding robustness can be seen in the design of the robotic shell and the enclosure which protects the wires within the body of the robot, with any external wires being fastened securely to the frame of the robot.

#### 2.1.4 Durability

Robot durability was also considered an important factor in order to ensure that the lifetime of a single robot was sufficient in relation to the cost of assembly and operation. In order to reduce the required maintenance, hardy mechanical components were developed, electrical components were chosen well within the predicted operating ranges, and tuning methods were developed which ensured that robots could operate without the need for constant readjustments to code parameters.

The robots were designed using parts well within the boundaries of the component operating ranges. Electrical considerations were made on the individual component level, as well as on the overall system level to ensure that voltage and current consumption spikes could be handled adequately and that no components would fail under conditions near the intended states of operation.

#### 2.1.5 Scalability

The study of robotic collectives requires numerous platforms operating concurrently, which further emphasizes the need for the robots to be robust, durable, as well as scalable. Collections of four to five robots were the target of the process, such that developing the platforms with the aspect of scalability in mind was important in ensuring that a number of robots could be produced and maintained easily.

As a result, the robots are designed with the intent of being easy to assemble, with mechanical components all derived from 3D printer-based materials and all circuits based around a readily available electrical prototyping material called perfboard.

A suite of tests were developed, further described in Section 2.1.7, which enhanced the ability of the human operator to diagnose issues and identify sources of error in malfunctioning robots. Electrical and software identification and repair times were drawn to a minimum with this system, and collections of up to five robots could be easily maintained by a single person.

### 2.1.6 Maintainability and Availability

The issues of scalability, maintainability, and availability are all inherently intertwined. All aspects of the robots were designed from components which were not only well within their specifications, but also readily available from local hardware stores or reliable online sources. The bulk of the robot frame is composed of 3D printed parts, assembled with standard nuts, bolts, and washers, which can be easily disassembled and repaired in a short period of time.

Electrical components were also chosen with availability in mind; cheap components were readily obtained from nearby hardware stores, with more specialized hardware such as motors and cameras kept in stock with additional supplies available within a short timescale.

### 2.1.7 Testability

The robots are composed of many interacting mechatronic systems which present numerous behaviors in the event of a component malfunction. A suite of test methods were developed in order to minimize the time to diagnose issues and thereby reduce the overall turnaround time in repairing robots, increasing robot availability. The test package is comprised of methods which can be used to diagnose the performance of every sensor currently implemented on the robotic platform, ranging from the low level analog readings of the force resistive sensors to the high level camera object recognition methods and the behavior of the PID motor controller which depends on such camera inputs. Test methods have been implemented at numerous levels within the electromechanical system hierarchy of the robot such that a collection of up to five assembled robots can have all components thoroughly tested in under an hour.

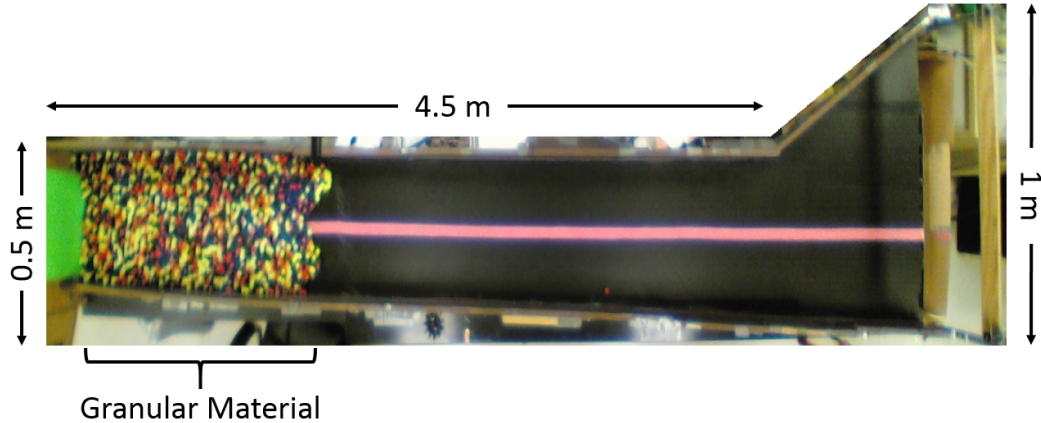


Figure 2.1: Top-down view of tunnel setup

## 2.2 Test Bed Design

The environment in which the robot system operates was designed in order to facilitate a safe, autonomous operation even in the absence of a human operator. The geometries of the tunnel were designed with the relative dimensions of biological ants in mind, such that comparable traffic dynamics may emerge.

### 2.2.1 Tunnel Geometry

To elucidate the effect of spatial constraints on active matter systems, the environment of the system was structured in order to force the robots to interact with one another, with the test bed built to be approximately 3 robots widths across.

As the tunnel length becomes shorter, the traffic dynamics of the system would be dominated by the congestive ant interactions at the excavation site and depositing site, while a relatively long tunnel would result in the traffic dynamics being dominated by the open tunnel agent interactions. A tunnel length of approximately 6 m was chosen in order to provide ample tunnel length to capture the interaction behaviors of both robots at the digging and depositing sites as well as in open-tunnel situations. An overview of the tunnel is given in Figure 2.1.

Previous tunnel designs featured two separate staging areas for material deposition and robot charging. The site allocated for resting was located along the tunnel, which may have contributed to greater traffic conflicts than the behavior of the resting robots would truly produce. Resting robots would only be able to rest after traversing a tunnel which could have already been congested, thereby expending even more energy in the resting state than would otherwise be necessary.

The new tunnel design consolidated the charging stations and depositing stations into a single location, which were made to be sufficiently large to accommodate up to five robots. This allowed robots to immediately enter the resting state upon completion of a deposit.

As in previous iterations, the charging station design, seen in Figure 2.2 is composed of two 22 gauge wires held under tension by springs anchored on both sides of the charging and depositing site by a frame constructed out of 80/20 1"×1" T-slotted aluminum. The charging wires were isolated from the metal frame using a 3D printed mounting bracket. The wires spanning the Charging and Depositing sites were connected to a power supply such that the upper wire carried a voltage of +4.2V with the bottom wire acting as ground.

### 2.2.2 Excavated Material

Previous experiments were performed using cotton as the simulated granular media the robots transported within the tunnel. The material was cheap and could be effectively used within the control loop of the robot machine vision algorithm to move towards the digging site. However, the fibrous cotton would regularly get caught in the robot motors, thereby hindering the ability of the robots to move about the tunnel.

A magnetic granular material was used in order to more effectively emulate the granular material manipulation task biological ants perform. Hollow, threaded hemispheres were 3D printed which could contain a loose rare earth magnet and be assembled manually. The internal magnet is not fixed within the shell, such that neighboring pellet magnets may reorient and align in order to form a cohesive, granular material.

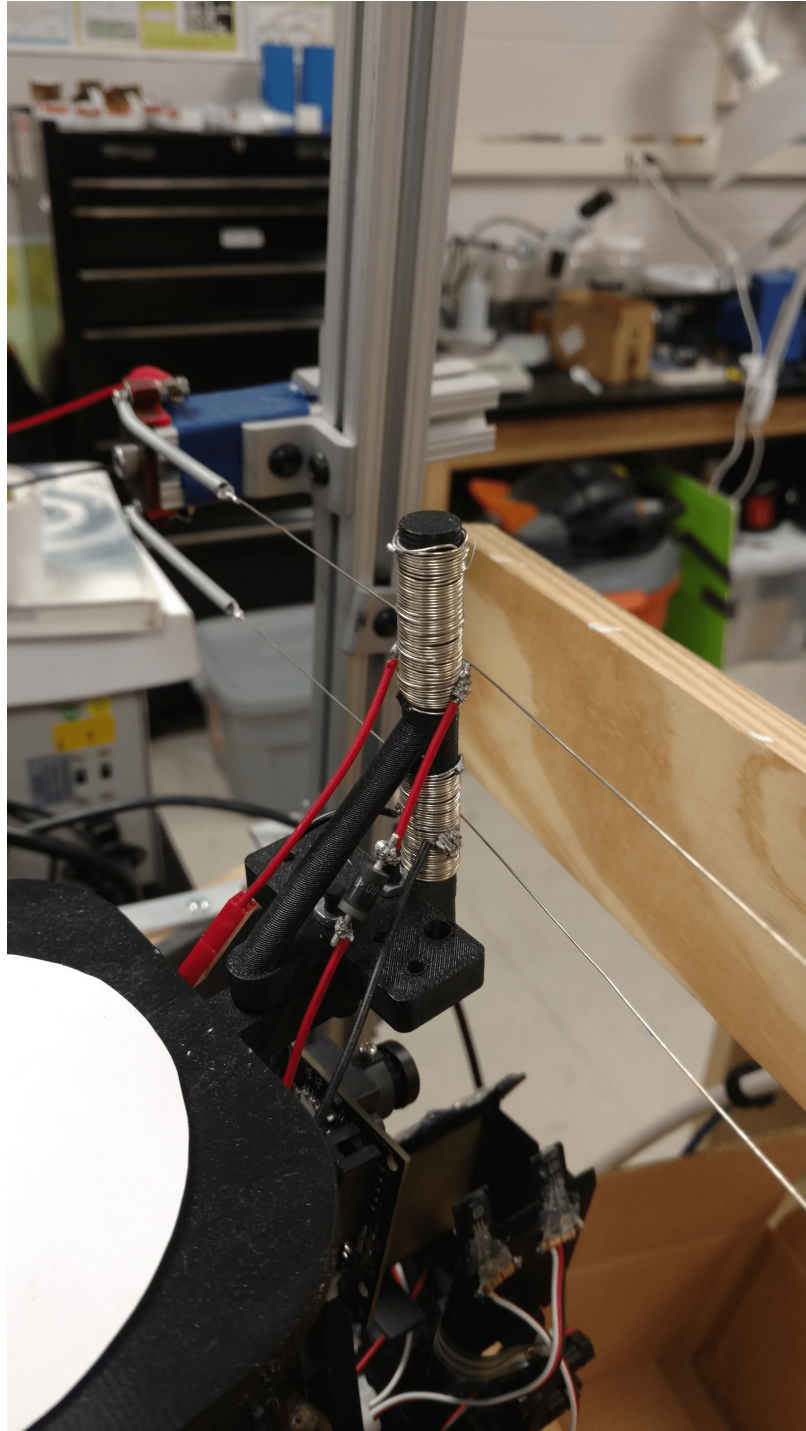


Figure 2.2: Charging station setup



Figure 2.3: Magnetic granular material

## **CHAPTER 3**

### **ROBOTIC ANT ELECTRICAL DESIGN**

The new design of the robotic ant platform involved complete redesigns of the power distribution circuitry in order to develop a more robust system. In this chapter, all electronic components on the ant robot are reviewed, with attention given to their implementation and methods which improve system reliability.

#### **3.1 Microcontroller**

Previous iterations featured two microcontrollers per robot, one Arduino Due which handled sensory inputs and actuator control, and a second Arduino Fio which handled a number of auxiliary systems. Arduino microcontrollers were preferred for their ease of implementation in comparison to other more computationally capable hardware such as a Raspberry Pi. The Arduino microcontroller family, particularly the Arduino Due, has a sufficient number of I/O ports which can support ADC and PWM, as well as a number of communication protocols such as UART, SPI, and I<sup>2</sup>C which can be used to interface with other hardware [16].

Previous iterations of the robot utilized an Arduino Fio to report data wirelessly via XBee radios, log data to an onboard microSD card reader, and communicate to an LCD screen in order to visually display various robot data in order for operators to easily evaluate the state of the robot and perform debugging procedures. The Arduino Fio was found to be susceptible to untimely resets, which could cause the entire robot to reset, in the event of a power consumption spike by the robot actuators. These spikes are a common occurrence in congested robotic systems, as robot-robot interactions can cause numerous motors and servos to stall. In the event of a motor stall, the Arduino Fio could temporarily lose power and restart, wiping the data stored on the microSD card, and often disrupting

communications on the Arduino Due to the extent that irrecoverable issues would regularly arise.

The main reason for including the Arduino Fio related to difficulties in using the hardware of the Arduino Due to interface with the hardware previously connected to the Arduino Fio, such as the XBee radios and microSD card reader. These issues arise from the unique architecture of the Arduino Due. The Arduino Due is the first Arduino platform built around a 32-bit ARM core microcontroller, diverging from the standard AVR microcontrollers used in the prototypical Arduinos. After several iterations of various power management systems, which did not resolve the compromising issues related to the Arduino Fio, a decision was made to pursue removing the Arduino Fio altogether. Support of the Arduino Due ARM architecture is still developing; transitioning the functionality of the Arduino Fio to the Arduino Due was only possible after porting several AVR libraries to work on the architecture of the Arduino Due. A set of libraries were implemented which ported all of the functionality of the libraries implemented on the Arduino Fio's AVR architecture to the Arduino Due's ARM architecture. Upon deployment of the newly developed ARM-directed software, all hanging issues associated with the power consumption spikes were resolved.

It is important to note that the Arduino Due, unlike most other Arduino boards, runs at 3.3V. Voltages applied to the I/O pins greater than 3.3V can damage the board. The electronics of the robot ant are engineered with this in mind, which required careful component selection as well as the inclusion of protective circuitry in the form of voltage dividers.

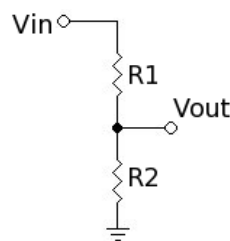


Figure 3.1: Standard voltage divider schematic

Voltage dividers are a relatively simple circuit which are utilized throughout the ant robot to correlate sensed voltages in the range of 0V-3.3V to greater voltages which the Arduino Due cannot safely sense via the I/O pins. The general schematic for a voltage divider is given in Figure 3.1. Application of Ohm's law gives  $V_{out}$  as a function of the resistor values chosen and  $V_{in}$ , which is determined prior to the circuit design. Voltage dividers are utilized throughout the robot, such as in the circuits relating to battery voltage sensing and Hall effect sensors. Careful selection of the  $R_1$  and  $R_2$  resistances allows the Arduino Due to safely sense all necessary voltages on the robot without damaging the I/O pins.

$$V_{out} = \frac{R_2}{R_1 + R_2} \times V_{in} \quad (3.1)$$

## 3.2 Sensors

The robots were designed to behave in a fully autonomous manner. A suite of sensors were implemented on the platform such that each individual robot can sufficiently perceive the local environment as well as internal parameters to modulate behavior accordingly.

### 3.2.1 Pheromone Trail Detector

Laboratory experiments have been shown to demonstrate that fire ant foraging uses a social insect communication mechanism involving pheromone trails [17]. A simulated pheromone trail was implemented to allow the robot to navigate efficiently through the tunnel by using an onboard camera to observe the location of a line on the tunnel floor and control the motor inputs to center the line within the frame of the image.

The robot ant is able to visually perceive the local environment through the use of a Pixy (CMUcam5), developed by Charmed Labs [18]. The Pixy camera can be programmed to recognize many distinct objects in a single image using up to seven different color signatures. The Pixy camera operates at a rate of 50 images per second with an image resolution

of  $640 \times 400$ , giving the robot ant the ability to rapidly adjust to changes in the environment.

The Pixy camera is supported by a program called PixyMon, which is used to upload updated camera firmware, debug camera related issues, and tune the color filtering parameters used in the blob analysis-based algorithm described below.

The Pixy camera captures the scene in response to a software call to the hardware using the UART communication protocol. An example of an input to the Pixy camera onboard filtering algorithm can be seen in Figure 3.2. The image is then thresholded according to the various color parameter characteristics tuned in PixyMon in order to capture regions of the image which express a certain color profile. The pixel areas of these blobs, as well as the centroids, are then computed on the Pixy camera. Further filtering can be performed on the arrays of blobs that are generated from this procedure, such as the removal of blobs which are above or below certain desired areas. The blobs which remain after the filtering process are then written back to the Arduino Due via UART.

As the robot nears the digging site, the granular media would occlude the pink trail, with no inputs available for the camera to observe.

The robot uses the Pixy camera to survey the region of the tunnel ahead of the robot and identify the pink trail which runs the length of the tunnel. The robot uses the output from the Pixy camera to control the motor commands to effectively follow the pink trail. However, as the robot nears the digging site the granular media occludes the pink trail; the Pixy camera is unable to identify the pink trail that is now beneath the granular media.

The issue of the disappearing pheromone trail was previously addressed by giving the robots the ability to also use a PID controller based on the centroid of the uniformly colored cotton being excavated, though the current magnetic granular media lacks any semblance of color homogeneity. A green panel was added to the back surface of the tunnel, which was used for the robotic motor control when the area of green blob was sufficiently large. Including a second color allowed the robots to accurately track towards the digging site over a range of distances within the tunnel.



Figure 3.2: Raw Pixy camera perspective of digging site prior to filtering

The ant robots are currently programmed to seek out areas of pink when present, and green when no significant areas of pink are in the image frame. The image seen in Figure 3.2 after the filtering process can be seen in Figure 3.3.

The horizontal component of the centroid of the dominant color in the image was used as an input to a PID controller which computed the error between the center of the colored centroid and the true center of the image, and produced differential signals for both motors of the robot, thereby rotating the camera frame which would move the centroid of the block closer to the center of the image. Biases in the differential signals were then added to the PID controller output which could allow the robot to move both forward and backward along the pheromone trail.

### 3.2.2 Navigation

The robot ant is able to navigate the tunnel using the Pixy camera, though there is no sense of orientation obtained from the camera. Color coding various components of the tunnel has been utilized in the past, though a simpler implementation was accomplished using an

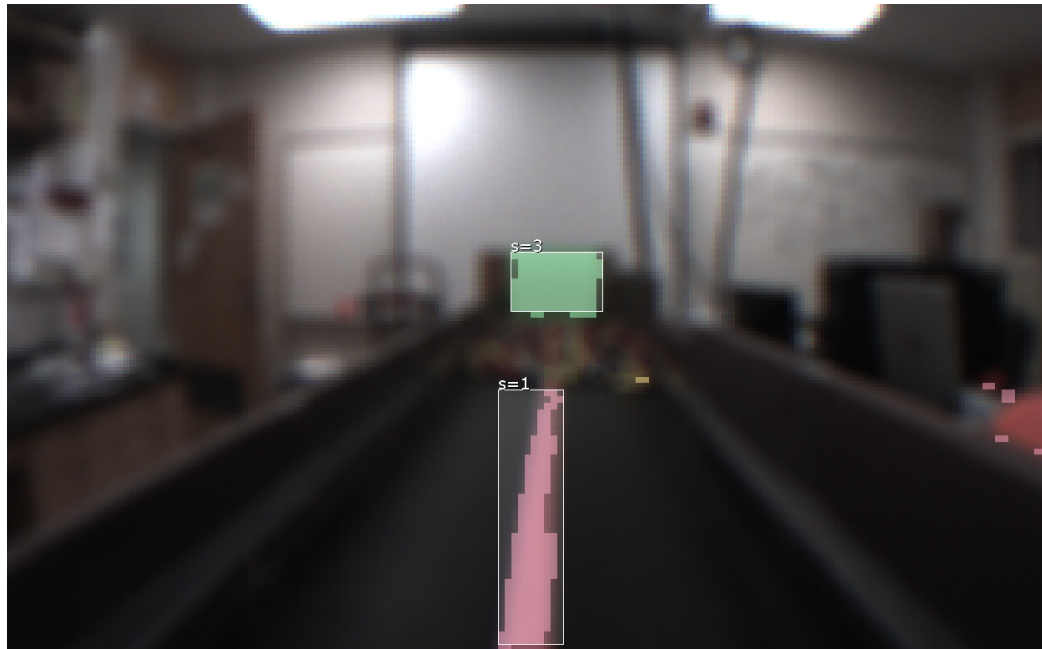


Figure 3.3: Pixy camera perspective of digging site after filtering

inertial measurement unit (IMU).

This method may be representative of the navigation methods used by excavating ants, as numerous studies have been conducted which investigated the effects of magnetic fields on social insects such as honeybees [19, 20], red wood ants [21], and more recently fire ants [22]. The fire ant, *S. invicta*, was first demonstrated by Anderson and Vander Meer to be sensitive to disturbances in magnetic fields in low-light environments, like one would encounter in a tunnel, though their research did not demonstrate a consistent directional orientation [23]. Recent findings have revived the interest in ant sensitivity to magnetic fields, such as the research presented by Sandoval et al. which built upon the work of [23] to ultimately demonstrate that *S. invicta* in weak illumination conditions exhibit consistent magnetic orientation with the geomagnetic field.

Another option for orientation tracking which was considered involved the use of motor encoders, though in these multi-robot systems the robots would regularly bump into other robots and walls, such that dead reckoning methods for monitoring orientation data would be error prone and unlikely to work effectively. The robots were outfitted with a LSM9DS0

IMU, which communicates magnetometer, accelerometer, and gyroscope readings to the Arduino Due using the I<sup>2</sup>C communication protocol [24].

The inclusion of the LSM9DS0 on the platform is useful in the self-orientation of the robot, which uses the readings reported from the IMU to determine if the direction faced by the robot is in the desired direction, and can be used in a closed-loop control algorithm in the turning behaviors of the robots to effectively reorient in the event that the robot is not facing the appropriate direction.

#### *Addressing the Issue of IMU Bias*

A common problem for IMUs such as the LSM9DS0 is the issue of bias, in which the readings of the sensor are perturbed from the true values over a period of time due to electrical and magnetic fields near the circuitry of the IMU. The data from the sensors were found to be heavily biased, such that magnetometer and gyroscope data often took on impossible values in terms of real world conditions. There are three principle factors which are important to consider when analyzing the general error terms of an IMU: repeatability, stability, and drift. Repeatability of a bias relates to the change in the bias value from turn-on event to turn-on event. The LSM9DS0 was found to have good gyroscopic repeatability; the bias for a single IMU was consistently near a certain bias value over all boot-up processes. Higher variability in turn-on to turn-on biases would have required more complex estimation methods. However, because the bias had good repeatability, the IMU could be calibrated using the method outlined in Section 3.2.2 prior to a test and the bias compensation parameters could be assumed to be correct for the entire period of the trial.

The stability of the IMU readings corresponds to the ability of the sensor, given a constant physical input to deliver a consistent output. In terms of the data output, the stability of the IMU may be thought of as the standard deviation of the output signals for a given IMU orientation. The LSM9DS0 was found to have reasonable stability, which did not require any compensation or filtering techniques.

The drift of the IMU is defined as the change in the output over a period of time. Relating back to the statistical correlation of the data output, while the stability can be thought of as the standard deviation, the drift corresponds to the movement of the mean output over a period of time. The drift of the LSM9DS0 was found to be small as well, such that the calibration process did not need to be repeated regularly.

### *Developing a Robust IMU Calibration Method*

The magnetometer data obtained from the IMU is given as three orthogonal components,  $H_x$ ,  $H_y$ , and  $H_z$ , of the magnetic field influencing the sensor. The values of  $H_x$ ,  $H_y$ , and  $H_z$  are RAW signed 16-bit readings from the sensors, with units in ADC ticks. The robot was assumed to always be sitting flat on the surface of the tunnel, such that only  $H_x$  and  $H_y$  were considered in the computation of the heading of the robot, accomplished using a simple trigonometric relationship to map the values of  $H_x$  and  $H_y$  to values between  $0^\circ$  and  $360^\circ$ .

The biases in the  $H_x$  and  $H_y$  terms are easily visualized by plotting the output of the LSM9DS0 mounted on a robot as the platform is rotated through a  $360^\circ$  sweep, as seen in Figure 3.4 for five different IMUs, all with evidently distinct bias parameters. An IMU with zero biases would be centered at the origin of the  $H_x - H_y$  plane.

Because the IMU bias terms were found to be consistent over long periods of time, the calibration method was accomplished using a mapping from the uncorrected circle traced in the  $H_x - H_y$  plane to a proper unit circle by computing the difference between the maximum and minimum  $H_x$  and  $H_y$  terms as the IMU is rotated about a  $360^\circ$  sweep. This difference, along with the maximum and minimum values, are used to shift and scale the readings at runtime on the robot using Equations 3.2 and 3.3.

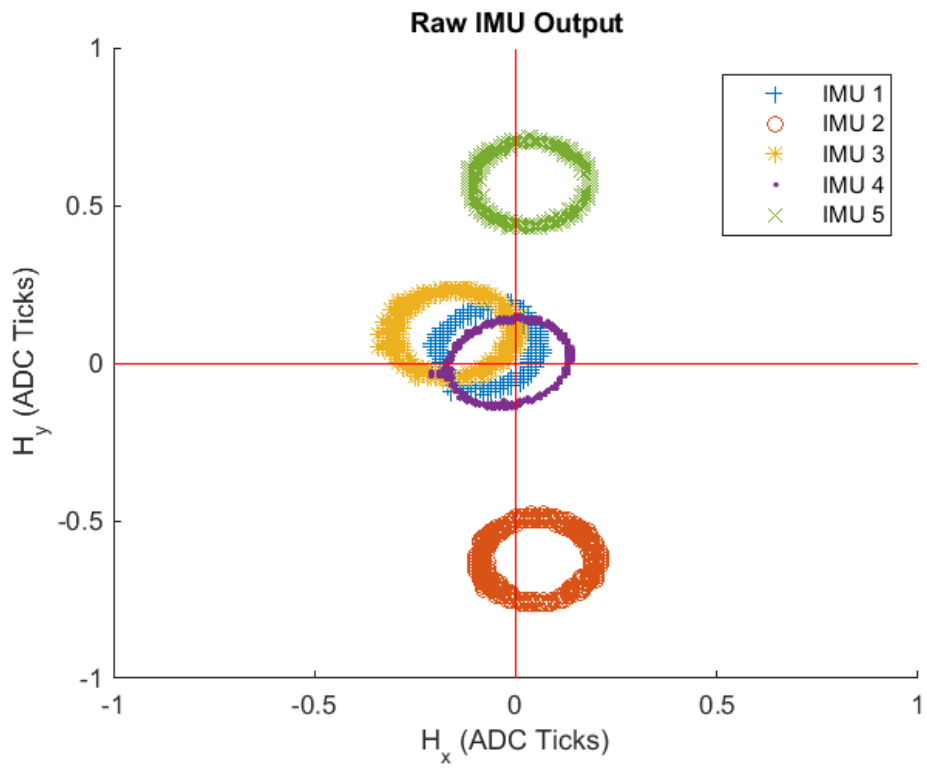


Figure 3.4: Raw heading readings prior to calibration.

$$H_x^{cal} = 2 \times \frac{(H_x^{raw} - H_x^{min})}{H_x^{max} - H_x^{min}} - 1 \quad (3.2)$$

$$H_y^{cal} = 2 \times \frac{(H_y^{raw} - H_y^{min})}{H_y^{max} - H_y^{min}} - 1 \quad (3.3)$$

The results of the calibration method are visualized for five IMUs in Figures 3.5-3.9. A three dimensional space relating the IMU  $H_x - H_y$  readings to the calculated heading is presented as two projections onto the  $H_x$  (top of each figure) and  $H_y$  (bottom of each figure) planes. The leftmost column of each figure displays the raw, uncorrected IMU data and predicted headings prior calibration, with the data post calibration in the rightmost column. The colors of the points are maintained across the rows, such that the blue points in the left column are mapped to the blue points in the right column via the described calibration equations. The black trace in the images represent the true heading readings which would be obtained from an IMU which could trace a perfect unit circle in the  $H_x - H_y$  plane. As seen in the uncalibrated data, many of the IMUs lack the capability to fully express a complete  $360^\circ$  range, which all IMUs are capable of after calibration. Not only are all  $360^\circ$  of the circle expressed, the outputs of the heading computation with the calibrated data closely follow the true headings of a perfect unit circle.

### 3.2.3 Gripper Sensors

Several components were implemented on the gripping mechanism of the robot claw which is used to manipulate and grasp the magnetic granular material. These sensors provide a sort of tactile feedback which the robot uses to pick up materials during the excavation process.

Force resistive sensors (FSRs) are a type of variable resistor with a resistance that is correlated to the force exerted upon the sensor pad [25]. The FSRs were operated with

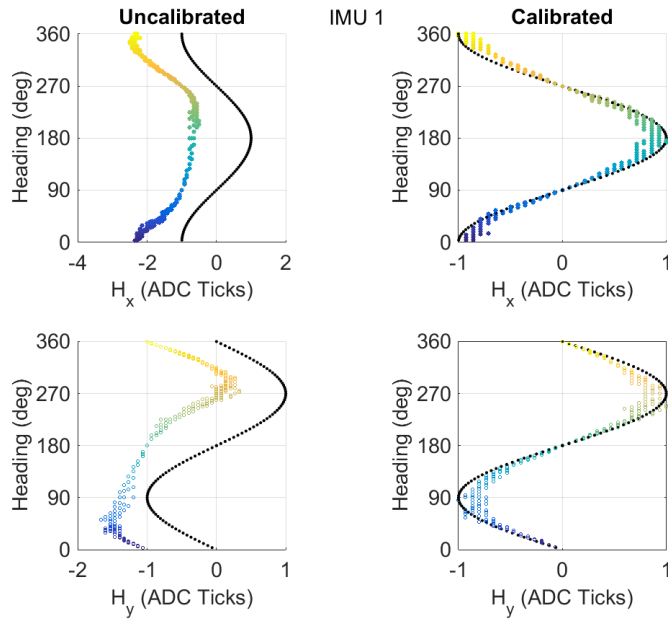


Figure 3.5: Visualization of calibration results for IMU 1

a 5V input, which required the development of a voltage divider in order to protect the 3.3V logic pins of the Arduino Due. The circuit was developed for two FSRs connected in parallel which could be sensed through an analog pin on the Arduino Due, and can be seen in Figure 3.15. Given the design of the circuit, high voltage readings across the 4.7k $\Omega$  resistor in FSR voltage divider indicated a presence of granular material in the gripper mechanism. Calls are made in the various stages of the robot finite state machine which check for the presence of material in the gripper based on a FSR analog sensor reading.

In addition to the FSRs, two Hall effect sensors were incorporated into the gripper in order for the robot to determine if the digging attempts were being successful in reaching the magnetic material. This enabled the robots to escape from digging sequences which were unlikely to succeed. Magnetic granular material can be strewn about the tunnel as the excavation period grows, such that small agglomerations of material can be located far from the digging site. Robots can come across this material and begin the digging protocol, though the likelihood of successfully grasping such small clusters is rather small. The inclusion of the Hall effect sensors allows the robots to effectively determine how

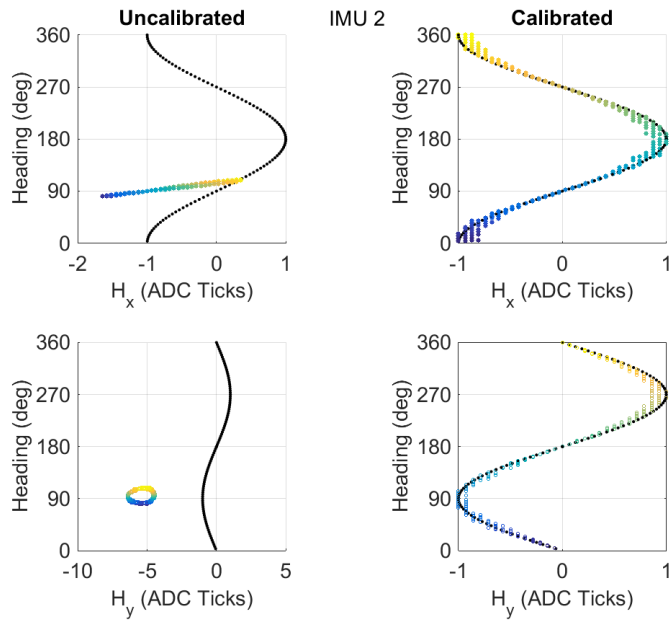


Figure 3.6: Visualization of calibration results for IMU 2

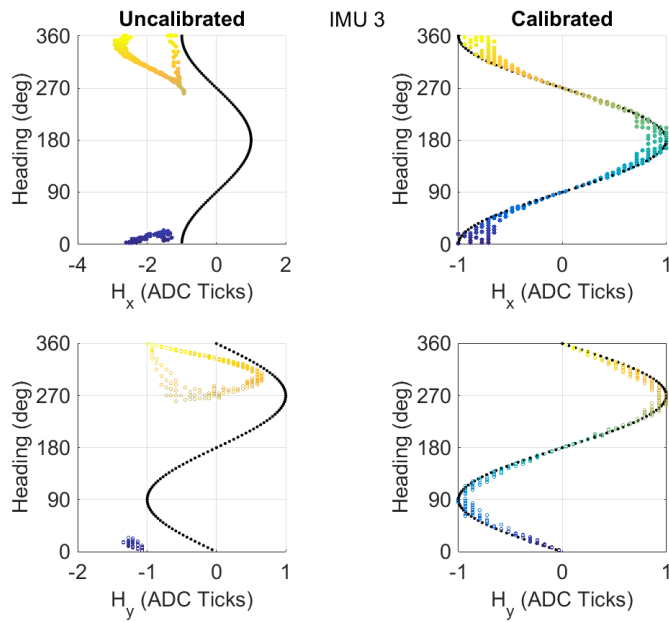


Figure 3.7: Visualization of calibration results for IMU 3

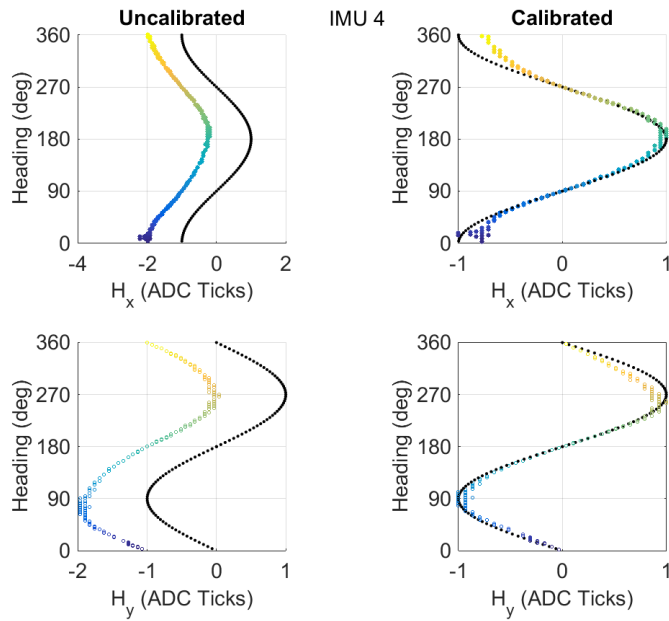


Figure 3.8: Visualization of calibration results for IMU 4

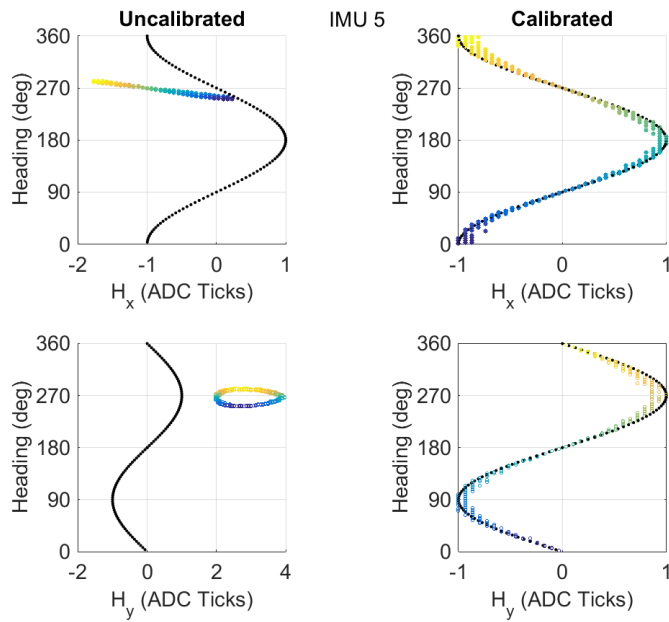


Figure 3.9: Visualization of calibration results for IMU 5

close an attempted dig was at grasping material, thereby allowing the robots to reduce the time spent attempting to collect materials with low success rates and effectively focus on attempts with higher success probabilities.

The model of Hall effect sensor chosen is the OPTEK Technology OH090U, which must operate with a minimum voltage of 5V [26]. The output signal of the sensor in the presence of a sufficient magnetic field switches from LOW to the value of the input voltage, in this case 5V. In order to protect the 3.3V Arduino Due pins, a voltage dividing circuit was developed for each Hall effect sensor. All supporting electronic circuits for the gripper sensors were consolidated onto a single perfboard located at the front of the robot, as seen in Figure 3.15.

#### 3.2.4 Charging and Deposit Site Detector

As mentioned in Section 2.2, the charging and material deposit site featured a pair of wires across which a 4.2V differential is supplied. Another voltage divider was implemented on the Anterior Sensing Board seen in Figure 3.15, along with the Hall Effect and FSR voltage dividers, which would allow the robot to safely sense voltages across the charging wire contacts up to 6.6V. Analog sensor pins of the Arduino Due were used to poll the charging wire contact as the robot navigated the tunnel using the Pixy camera until the charging detector indicated that the robot had reached the end of the tunnel and could proceed to engage in material depositing, charging, or resting behaviors.

#### 3.2.5 Digging Site Detect

The magnetic material which the robot was developed to transport was sensed using a MAG3110 breakout board, which features a small low-power magnetometer [27]. The MAG3110 was placed on the front of the robot, which acted as a bumper which would make contact with the magnetic material as the robot reached the digging site. The MAG3110 was polled regularly using I<sup>2</sup>C communication lines, and could be used in the finite state

machine to move the robot from the state which moves towards the excavation site to the state which attempts to grasp the granular material.

### 3.2.6 Power Consumption

In order to monitor the power consumption of the robot, a voltage sensor was implemented in the form of a voltage divider composed of two  $3.3\text{k}\Omega$  resistors between the positive battery terminal and ground, seen in Figure 3.11. The composition of this voltage divider, given Equation 3.1, will be able to safely measure battery voltages up to 6.6V. In addition, a  $\pm 5\text{A}$  ACS714 current sensor was implemented between the battery pack and all electrical components of the robot to capture the net current drawn by the robot [28]. A shunt resistor was considered in order to monitor the current drawn by the robot, though the reversal of current in the event of charging would have been damaging to the pins of the Arduino Due. The use of the ACS714 is advantageous in that it features a voltage centered logic which allows the monitoring of current in both directions.

The current data measured by the ACS714 in conjunction with the voltage data obtained from the aforementioned voltage divider were used to compute the instantaneous power consumption of the robot over the period of a trial, which was written to an onboard SD card.

### 3.2.7 Physical Contact Sensors

Previous iterations of the ant robot employed the use of SPST switches to detect contacts of various panels of the robot with neighboring robots or the tunnel walls. While the SPST implementation is sufficient for identifying tactile interactions, no information is obtained regarding the type of obstacle that has been contacted. The optimal response of a robot to a contact with the stationary wall of the tunnel is not necessarily the same as the optimal response of one robot to another moving robot. An alternative solution was implemented which utilized the MPR121 sensor to poll the capacitive values of copper panels on the

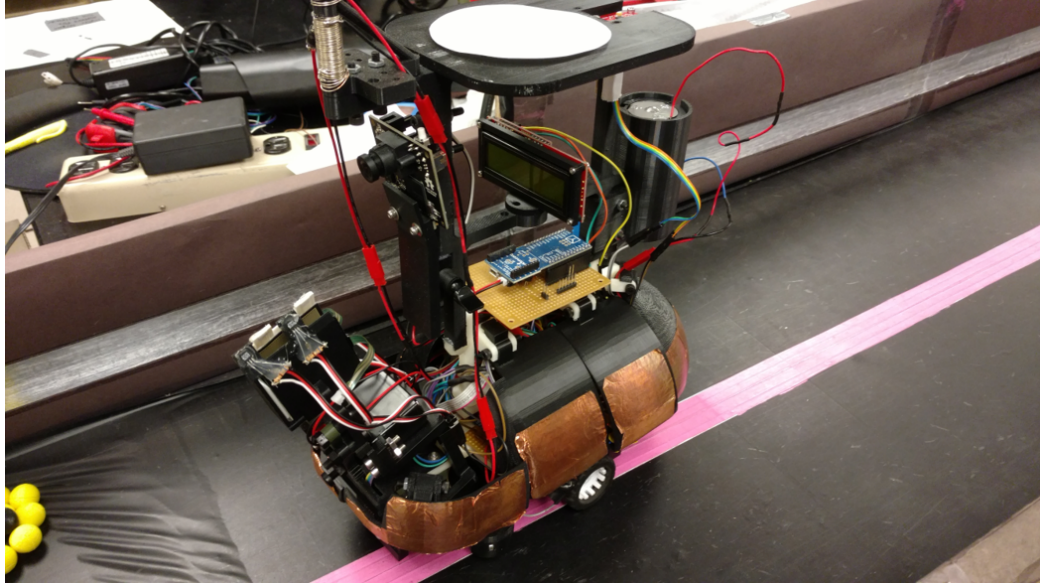


Figure 3.10: The copper on the robots and aluminum on the tunnel walls have different capacitive sensor values

sides of the robots [29].

The walls of the confining tunnel were lined with a layer of aluminum adhesive and laminated with a layer of clear packing tape, while the capacitive panels on the robot shell were composed of copper adhesive tape. The Arduino Due communicates to the capacitive sensor board via I<sup>2</sup>C and polls each of the eight panels located on the robot. The returned values from the sensor are then thresholded and identified as contacts with copper or aluminum according to experimentally pre-determined sensor ranges.

### 3.2.8 Sensor Summary

A review of the various components employed on the ant robot platform is given in Table 3.1. These sensors provide the robot a set of exteroceptive and interoceptive inputs which can be used in the traversal of the behavioral finite state machine.

Table 3.1: Summary of Robotic Ant Sensors

<b>Sensor</b>	<b>Function</b>
Pixy (CMU5 Camera)	Tunnel Navigation
IMU	Orientation, Obstacle Maneuvering, Tunnel Navigation
Capacitive Sensor Panels	Obstacle Detection
Force Sensitive Resistors	Gripper Tactile Feedback
Hall Effect Sensors	Gripper Magnetic Field Feedback
Charging Rod	Charging and Depositing Site Detection
Anterior Magnetometer	Excavation Site Detection
Current Sensor	Power Consumption Monitoring
Battery Voltage Sensor	Power Consumption Monitoring

### 3.3 Actuators

The various sensor inputs reviewed in the previous section are used in order to modulate the behavior state of the robot, which in turn send commands to the actuators which allow the robot to maneuver the tunnels and manipulate the magnetic granular material.

#### 3.3.1 Servo Motors

The gripper is actuated using two HS-5485HB servos obtained from ServoCity, one which controls the pitch of the gripper mechanism with respect to the ground and another which controls the grasping mechanism of the gripper. Each servo has an operating range of 4.8V-6.0V, with a stall torque of 72oz/in at 4.8V and a stall current of 1.2A.

The servos are supplied with a regulated 5V from the Central Electronics Board, seen in Figure 3.13, with control signals provided using the standard Arduino `Servo` library.

#### 3.3.2 Drive Motors

The same motors used on the previous iteration of the robot platform were used, though the mounting brackets were modified to create a more balanced system. These motors are composed of a high-power brushed DC motor with a plastic 120:1 reduction gearbox, with an operating range between 4.8V-6.0V, and a stall torque of 25oz/in with a stall current of

1.25A at 4.5V [30]. The current implementation of power supplied to the motors provides a voltage equivalent to the battery voltage, which ranges between 3.7V and 4.2V in experiment, such that these stall conditions will not be realized, and lower values should be expected. Furthermore, the plastic gearbox includes a safety clutch which slips in the event of a stall, preventing the gear teeth from being damaged by shear forces.

The motors were controlled using a breakout board for Texas Instruments' DRV8835, which is a H-bridge IC used for the bidirectional control of two brushed DC motors [31]. The DRV8835 is capable of safely driving motors with voltages between 0V-11V, with continuous output currents per channel at 1.2A and peak output currents per channel at 1.5A when operating at 5V. The logic voltages required for the DRV8835 are between 2V-7V, such that no intermediary circuits are necessary to communicate with the 3.3V logic pins of the Arduino Due. The DRV8835 has two possible control modes, one which utilizes the classic PHASE/ENABLE logic, in which each motor output pair is controlled using a phase pin which determines the direction of the motor rotation and an enable pin which controls the motor speed via PWM. The second control method, which was implemented on the robotic ant platform, is called IN/IN mode, and allows for more advanced control options such as coasting and braking that are utilized in the PID controller. The motor connections were wired in parallel with a  $0.1\mu\text{F}$  ceramic capacitor in order to smooth out the signal noise from the DC motors and protect the other electronics on the Central Electronics Board.

### **3.4 Circuitry**

There are two primary electrical boards which facilitate supplying power at the appropriate voltages to the various components found on the robot. The sensors and actuators located on the robots operate within two principle voltage ranges: 3.3V and 5V. The motors are supplied the voltage equivalent to the battery voltage, which falls in the range of 3.7V-4.2V, and will be referred to as BATT.

The battery connects directly to the Power Board, where power consumption is moder-

ated, voltages are regulated, and a relay controls the supply of power to components with relatively high idle power consumption such as the motors and servos. The BATT and 5V regulated line of the Power Board are connected to the Central Electronics Board, where communication lines and all 3.3V, BATT, and 5V power supply lines converge in order to power the appropriate components.

### 3.4.1 Power Board

The Power Board has several purposes, all of which focus around connecting to the 3.7V battery pack and driving various lines to the appropriate voltages prior to connecting to the Central Electronics Board, where the voltages controlled by the Power Board are ultimately connected to the sensors and actuators. The schematic for the Power Board can be seen in Figure 3.11, with the assembled circuit board seen in Figure 3.12.

The power from the battery pack is connected to the ACS714 current sensor, which is connected to the rest of the robot circuitry through the SPST emergency mechanical shutoff switch. The SPST switch connects to the battery through the line monitored by the current sensor, which connects to a voltage regulator, a battery charger, a voltage divider, and a solid state relay.

The 5V voltage regulator connects to the  $V_{CC}$  pin of the current sensor which supports the logic circuitry of the ACS714. The 5V regulator is also connected to the  $V_{in}$  pin of the Arduino Due, which has been found to supply sufficient power to support the microcontroller. A common ground is also used to ensure that all relative voltage levels reference the same ground.

The battery charger is a breakout board which utilizes the MCP73831T IC, which is able to simultaneously charge the connected battery pack while also continuing to power the attached load, with constant voltage regulation for input voltage ranges between +3.75V and +6V [32]. The input voltage is applied to the MCP73831T through a power supply connected to the Charging and Depositing Station wires mentioned previously in Section

2.2. When contact is established between the charging wires and the charging rods located at the front of the robot, as seen in Figure 2.2, the battery charger breakout board POS and GND pins are connected to the 4.2V differential which is used to charge the battery pack of the robot.

Between the SPST switch and the solid state relay is the voltage divider used to detect the voltage of the battery. The solid state relay is controlled by a digital pin of the Arduino Due, and can be opened or closed in order to connect the  $V_{in}$  and  $V_{out}$  leads of the solid state relay. When the robot is resting, the solid state relay can be opened, effectively disconnecting the actuating electronics of the robot such as the servos and motors, which have non-negligible idle power consumption. When the solid state relay is closed,  $V_{out}$  is connected to a pair of leads which go to the Central Electronics Board, carrying a voltage equivalent to the battery voltage and second 5V regulator which in turn connects to another trace on the Central Electronics Board. Both pairs of leads from the solid state relay utilize a signal filtering  $220\mu\text{F}$  capacitor.

### 3.4.2 Central Electronics Board

The Central Electronics Board sits at the core of the robot, and acts as the junction site to which all electrical components converge. The two leads from the Power Board, carrying BATT and 5V, connect to the DRV8835 motor driver and the servo bus, respectively. In previous iterations all sensors were driven off of these two lines, though power consumption spikes caused by actuator stalls would regularly disrupt sensor communications. As a result, these two power sources are solely used to drive the actuators of the robot, with all power to the sensors of the robot being supplied via the 3.3V and 5V pins of the Arduino Due. The Arduino Due 3.3V and 5V pins are connected to the 3.3V and 5V buses on the Central Electronics Board where all of the sensor power connections will attach; each pin is capable of supplying 800mA, which is well above the expected sensor load.

In addition to supplying power to all components on the robot, the Central Electronics

Board also has a communication bus which acts as the interface between the Arduino Due SCL/SDA lines and all of the SCL/SDA connections of the sensors for I<sup>2</sup>C-based communication.

### *Removing the Arduino Fio*

The Arduino Fio was previously used to handle auxiliary functions on the robots such as resetting the robot in the event of a system error, communicating and recording data, and writing debugging information to an LCD screen. However, the Arduino Fio was found to be one of the more error-susceptible components of the system, due to power supply issues. As a result, the system error handling processes of the Arduino Fio were primarily triggered by errors pertaining only to the Arduino Fio, thereby exacerbating the power supply problems. Ultimately these issues were resolved by the removal of the auxiliary microcontroller. The removal of the Arduino Fio required the development of a circuit for the Arduino Due which would enable the microcontroller to write data to both the microSD card and the LCD screen. Both of these components were powered through the 3.3V bus of the Central Electronics Board, with communication protocols being adopted which were supported by the Arduino Due. The Arduino Fio used an SPI protocol to write data to the microSD card, which is also possible on the Arduino Due; a ribbon cable was used to connect the central SPI pins of the Arduino Due to the corresponding pins of the microSD card reader. All other modifications to support the data-writing capabilities of the Arduino Due were made in software.

The LCD screen controlled by the Arduino Fio was useful for debugging purposes to output the various states of the robot behaviors and easily poll sensor values over the course of a test trial. The LCD screen is not vital to the operation of the robot, though the component has proven to be incredibly valuable in terms of maintenance and diagnostics. The supporting library for the LCD screen utilized a `SoftwareSerial` library which has yet to be implemented on the Arduino Due ARM microcontroller architecture. In

order to incorporate the LCD screen into the new system hardware, the LCD supporting software library was rewritten to operate on an Arduino Due hardware serial port. The newly developed library enables all of the previous functionality with several new writing features.

### 3.4.3 Anterior Sensor Board

The Anterior Sensor Board consolidates several boards from the previous robot iteration, while also adding in protective voltage dividers across several components. The Anterior Sensor Board receives a 5V power supply from the 5V bus of the Central Electronics Board, which is connected to a parallel pair of Hall effect sensors as well as a pair of force sensitive resistors. The outputs of the Hall effect sensors are 5V, which might have damaged the I/O pins of the Arduino Due if connected directly. A voltage divider was implemented using a 1.8k $\Omega$  and 3.3k $\Omega$  resistor pair, such that the voltage read by the Arduino Due when the Hall effect sensor outputs 5V will be reduced to a safe 3.24V.

The Anterior Sensor Board also features a voltage divider to detect an applied external voltage across the charging detector of the robot, using a voltage divider of two 3.3k $\Omega$  resistors. The contacts can be seen in Figure 2.2, which is made of 22 gauge wire wrapped around a 3D printed post. The output from the sensor is used as an input within the finite state machine to localize the robot, as the Charging and Deposit Site is the only location at which such an external voltage can be detected. The schematic for the board is given in Figure 3.15, with the assembled board in Figure 3.16

### 3.4.4 Battery Selection

The motors of the robot were found to operate well at values between 3V and 5V, while the HS-5485HB servos were only able to operate at voltages near 5V. The upgrade in the servos associated with the development of the custom gripper claw was associated with a large increase in power consumption relative to the previous iteration. In the event that

all of the actuating components of the robot stalled, the current draw was calculated to be 4.9A, which would be supplied directly from the battery pack. All other sensory components could be sufficiently supplied power by the Arduino Due 3.3V and 5V pins, which are rated to supply a net 1.6A. The previous robotic ant iteration utilized a single cell 3.7V Li-ion battery with a 3400mAh rating, which had the ability to discharge at a rate up to 7A. The Li-ion chemistry was found to offer a good weight-energy density ratio in comparison to rechargeable alkaline and NiMH batteries, while also avoiding some of the safety issues associated with LiPo chemistry batteries. Additionally the selected Li-ion batteries include protection against overheating, and built-in over-charge and over-discharge circuitry to improve the lifetime of the battery. A battery pack which holds three of the 3.7V Li-ion batteries was used to supply power to the robot, such that the robots could operate for long periods of time without recharging and stalls could be easily handled by the power supply.

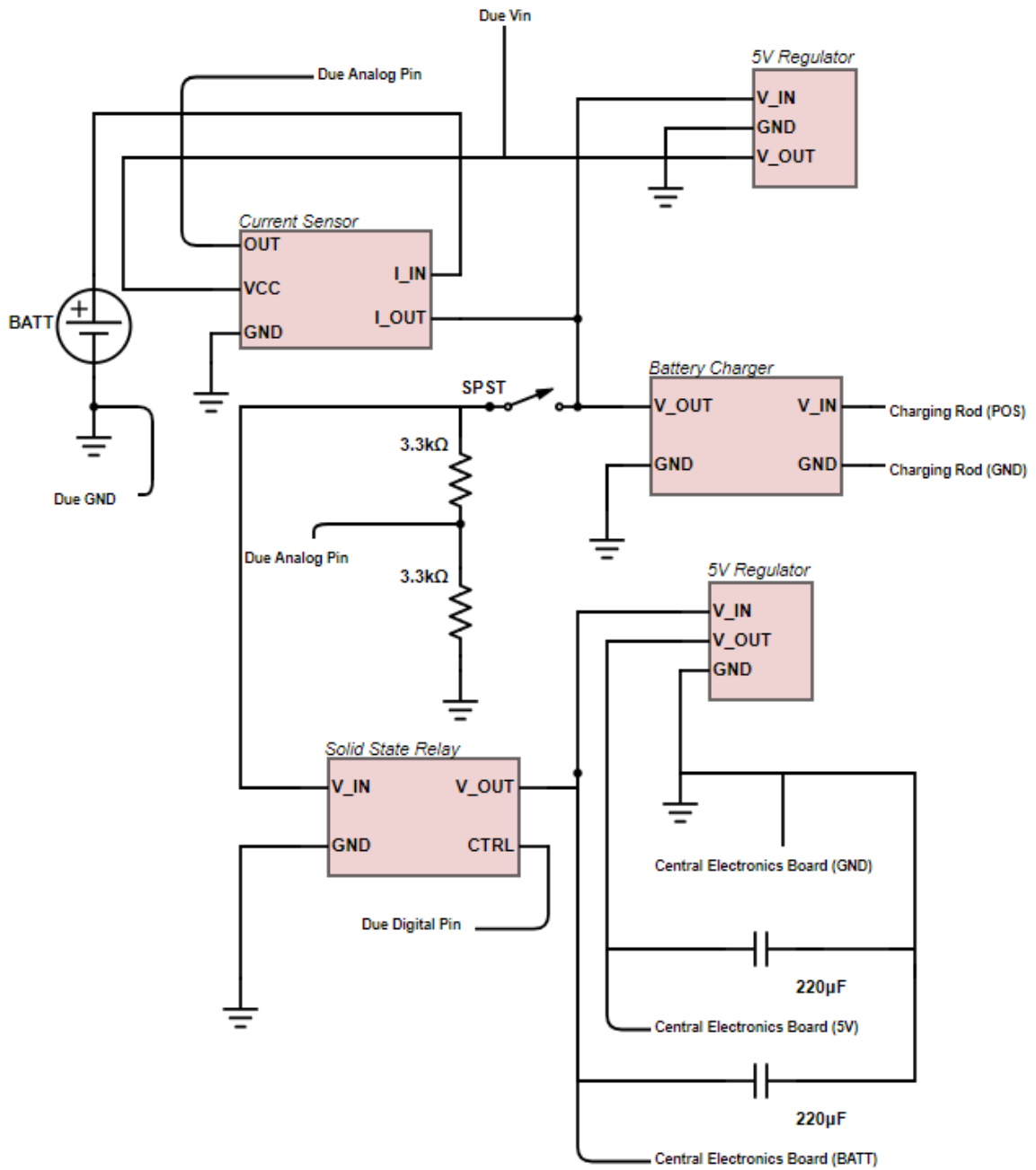


Figure 3.11: Power Board schematic



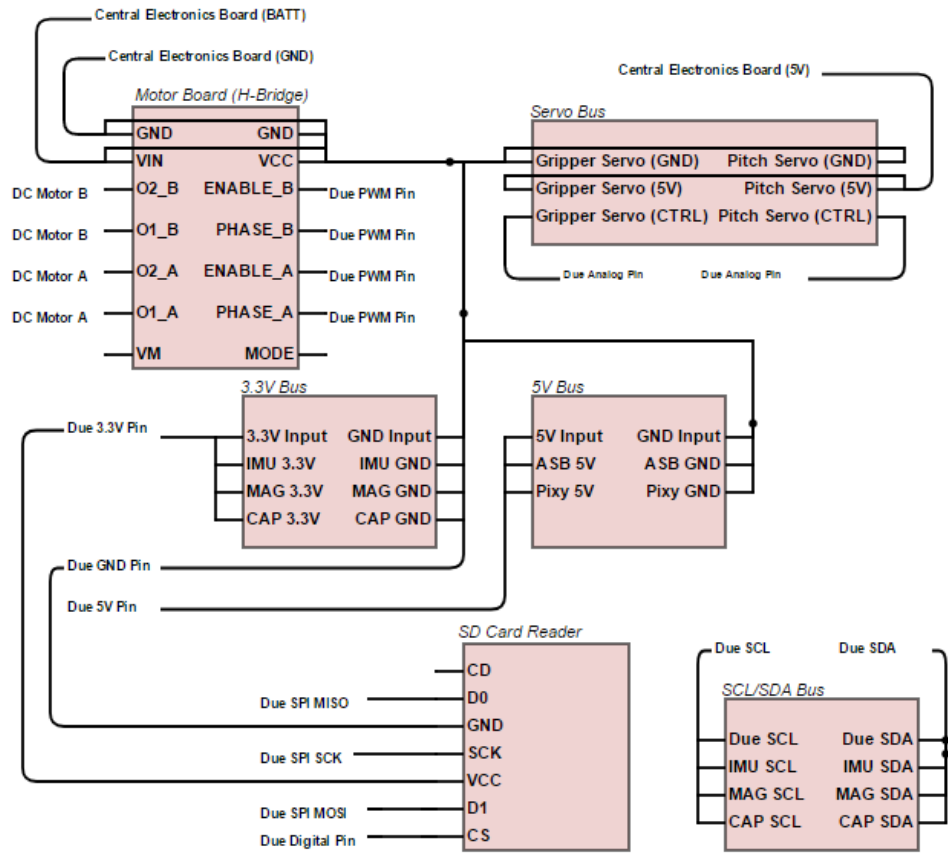


Figure 3.13: Central Electronics Board schematic

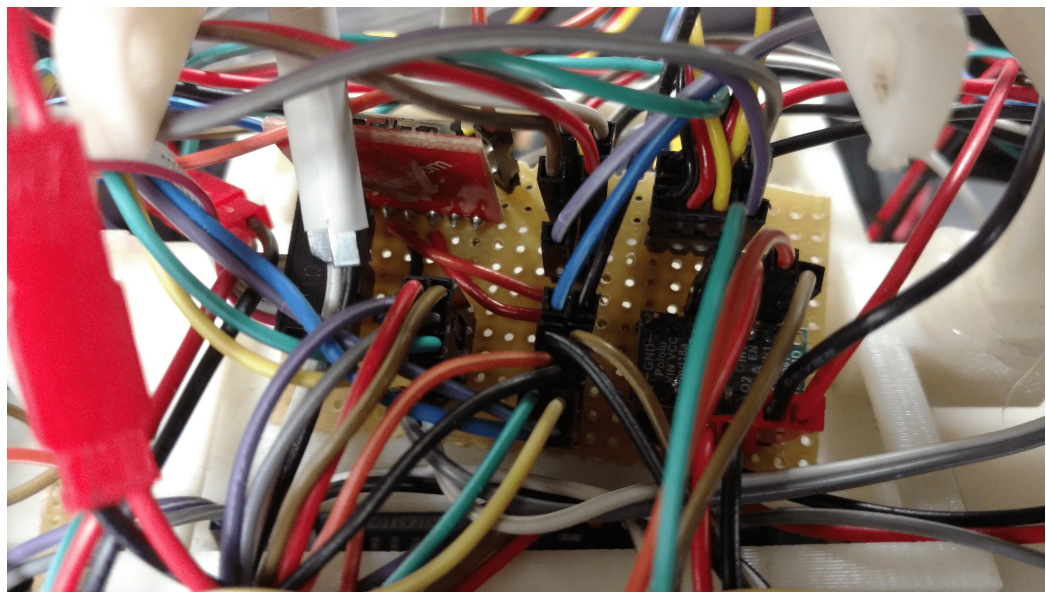


Figure 3.14: Assembled Central Electronics Board

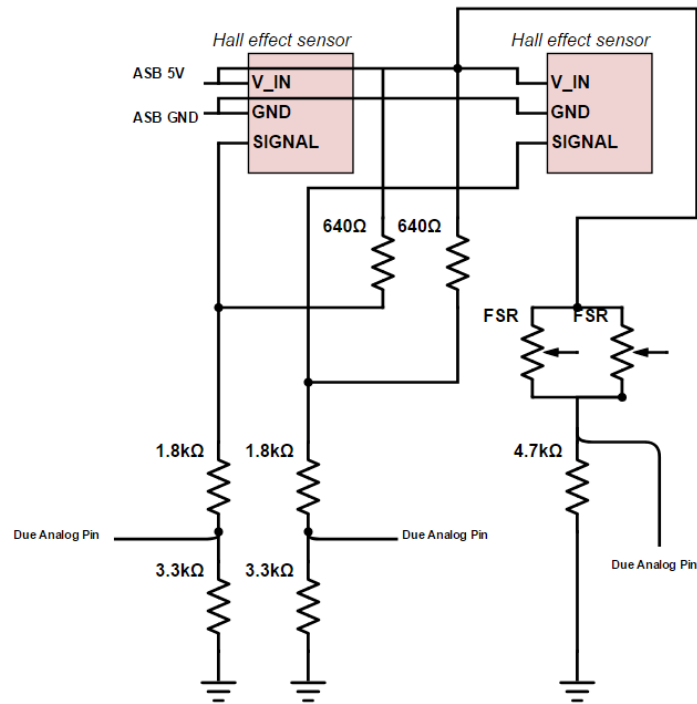


Figure 3.15: Anterior Sensor Board schematic

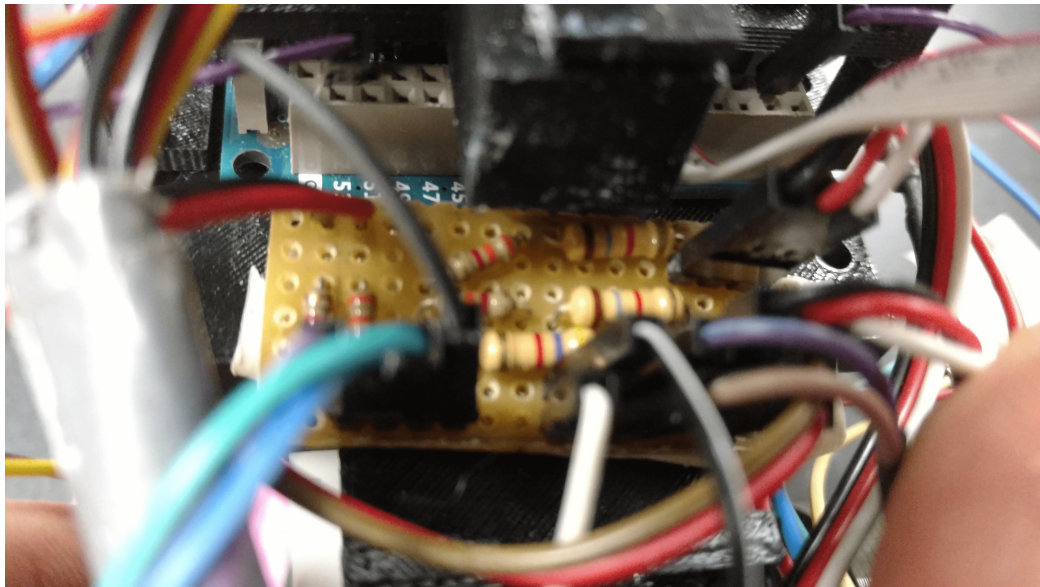


Figure 3.16: Assembled Anterior Sensor Board

## **CHAPTER 4**

### **ROBOTIC ANT MECHANICAL DESIGN**

Previous iterations of the ant robots were designed with the same core design principles in mind to develop a mobile platform capable of sensing the local environment and manipulating a granular media. The predecessor of this iteration was used as a source of inspiration for the new assembly design.

#### **4.1 Design Approach**

With the aforementioned design parameters of Section 2.1 in mind, the hardware of the robots were constructed such that all primary components of the robots could be produced on a 3D printer. This consideration in the design process facilitates maintaining the robots in the event of mechanical failures, while also making the platforms easily produced for increasing the scale of the ensemble.

All of the components of the robot were developed using a computer-aided design (CAD) software. Components produced in this software were designed within the context of all of the other constituent parts, with appropriate tolerances and fits considered prior to production. In spite of the relative geometric complexity of some of the components, all parts were easily manufactured by leveraging 3D printer technologies.

The 3D printers in the lab use an additive manufacturing process called Fused Deposition Molding (FDM), in which a heated filament of material, classically ABS plastic, is extruded through a fine nozzle onto a bed which then traces a silhouette cross section of the component being printed onto a single layer. Upon completing the layer, the bed is lowered a distance on the order of several tens of micros, and the extrusion process is repeated.

The use of this FDM process is important to the project for several reasons. First, the ABS plastic used by the 3D printer provides consistent parts which are relatively strong and

light, which is useful in designing a robust and durable robot. Furthermore, the parts are able to be produced quickly which not only reduces downtime in the event of a mechanical failure, but also expedites the iterative process in which new components are tested to assess their performance and efficacy.

In summary, the new platform of robots were inspired by the antecedent platform, with many common design parameters in mind. The use of 3D printers were leveraged to satisfy several design parameters, which permitted the development of a compact and robust platform to support the new iteration of the robots. Structures to support the updated package of sensors were developed, a custom gripper was implemented, and vestigial structures associated with the previous iteration's removed hardware were discarded.

## **4.2 Computer-Aided Design Overview**

Another design consideration in the context of these robotic platforms were geometric dimensions, such that the platform could capture some of the geometric constraints of the biological systems being emulated. Fire ants have an average length:width ratio of approximately 2:1; the robots were designed with length of 28 cm, a width of 14.5 cm, giving a length:width ratio of 1.93, with a height of 38 cm measured from the bottom of the wheels to the top of the charging rod. The robot ant system is a 2D emulation of the true biological ant system, so the height of each robot need not conform to any specific geometry.

The assembly of the robot is built upon the Modular Base which was designed with a flexible geometry and numerous holes sized to accommodate #4 screws which allows the base to attach to a number of components easily in many different configurations. All sub-assemblies of the platform are connected through the Modular Base. These sub-assemblies include electronics scaffolding, the differential driving motors and caster, as well as the newly designed gripper claw.

The upper half of the robot is built around the Electronics Scaffolding seen in Figure 4.4. The electronics of the motor converge at the Arduino Due, which is mounted directly

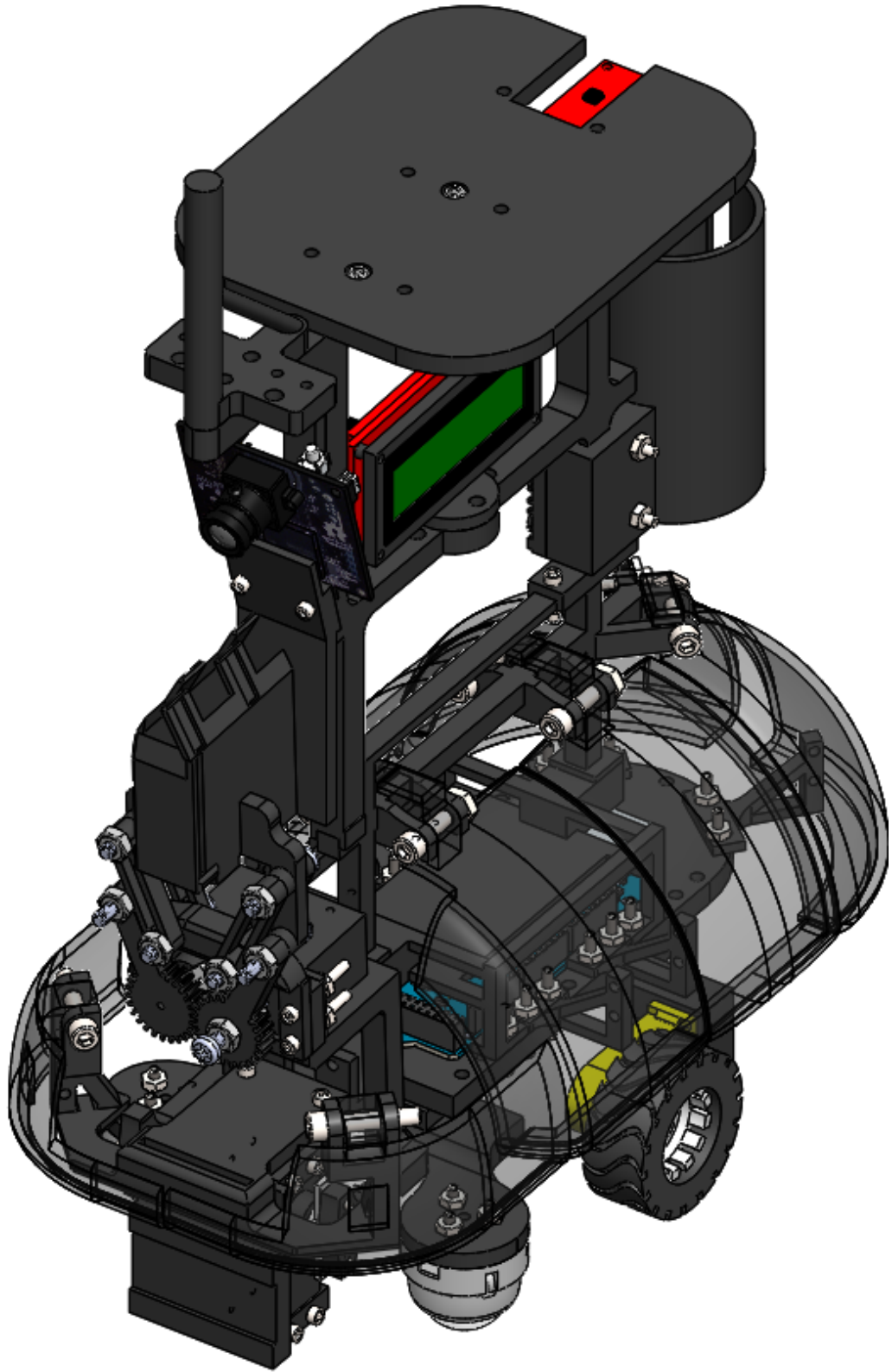


Figure 4.1: Ant robot isometric view

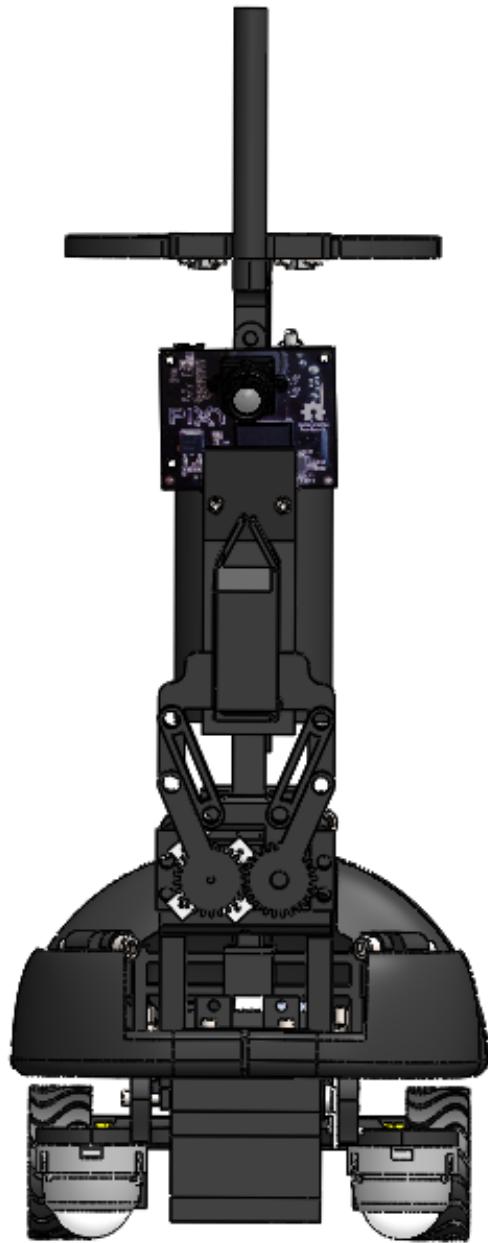


Figure 4.2: Ant robot front view

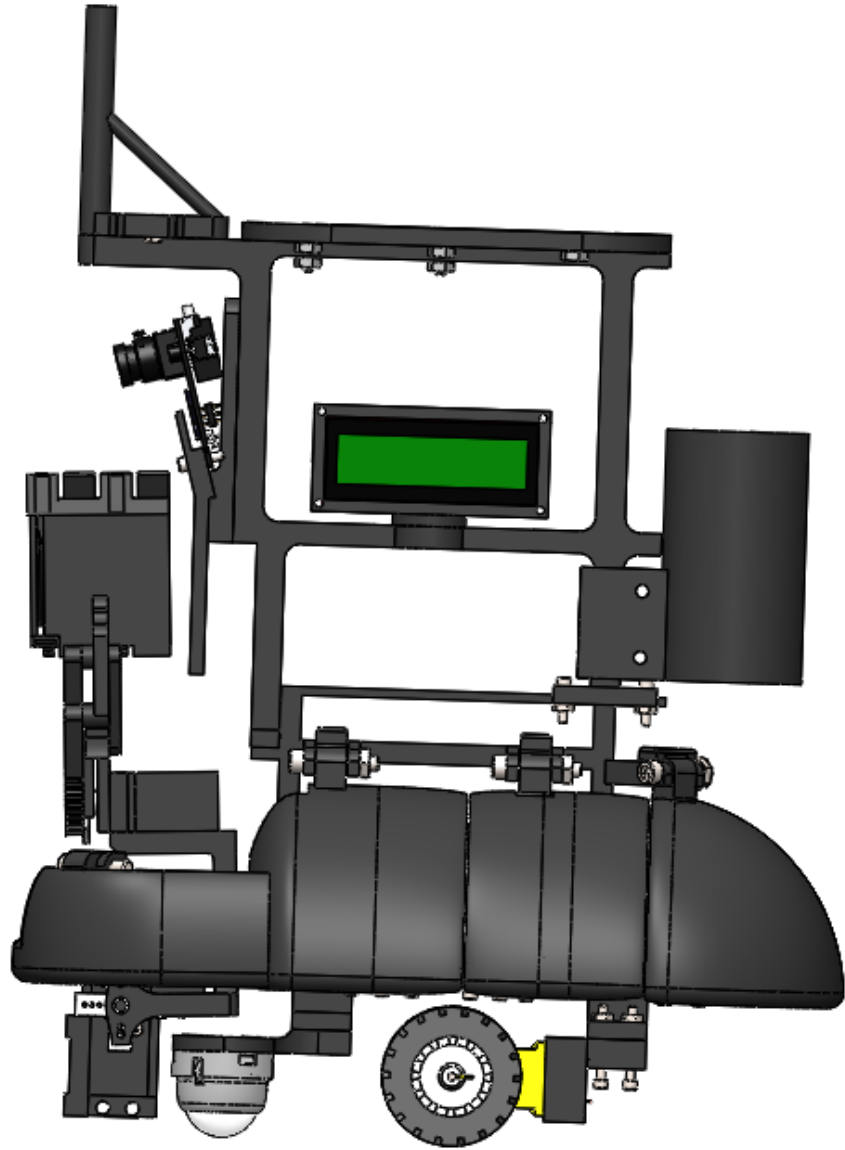


Figure 4.3: Ant robot side view

to the Modular Base using #4 screws through the medial holes on the Modular Base which match those of the Arduino Due. The Electronics Scaffolding is anchored to the Modular Base using the Electronics Platform, which straddles the Arduino Due across the width of the Modular Base and is affixed using #4 screws through the lateral holes of Modular Base. The Electronics Platform holds the Central Electronics Board, described in Section 3.4, and also has mounting holes for the Shell Skeleton upon which all of the contact panels of the robot hang. The components of the shell were mounted on the Shell Skeleton using a #10 screw as an axle, such that there was a hinge between the shell of the robot and the Shell Skeleton. This allowed the panels of the robots to flex in the event of a contact, and reduced the wear of the components. Panel Supports were mounted along the perimeter of the robot on the Modular Base which held the panels at a constant height and could be used for routing electronic cabling. The Central Electronics Board was mounted on the Electronics Platform, and the Power Board was placed towards the back of the robot behind the Electronics Platform within the shell, such that all of the primary electronics were contained within the shell of the robot, protecting them from being damaged by other robots. A pair of #4 screws connect the Shell Skeleton to the Electronics Extension above, which has numerous components attached to it such as the Pixy camera, LCD screen, battery pack, IMU, and charging rod.

The design of the Modular Base allows for a variety of drive systems to be implemented. The final product of the current iteration has only two motors which employ a differential driving system of locomotion, though legged platforms with up to four motors were explored over the period of design. Underneath the Modular Base are two mounting points which can be used as an attachment site for motor brackets. This design allows motor brackets of varying geometries to be designed and printed rapidly, as opposed to printing an entirely new Modular Base to test a new locomotion platform. The exploded view of final design of the motor and caster assembly can be found in Figure 4.5.

The two mounting bracket trees located on the bottom of the Modular Base were de-

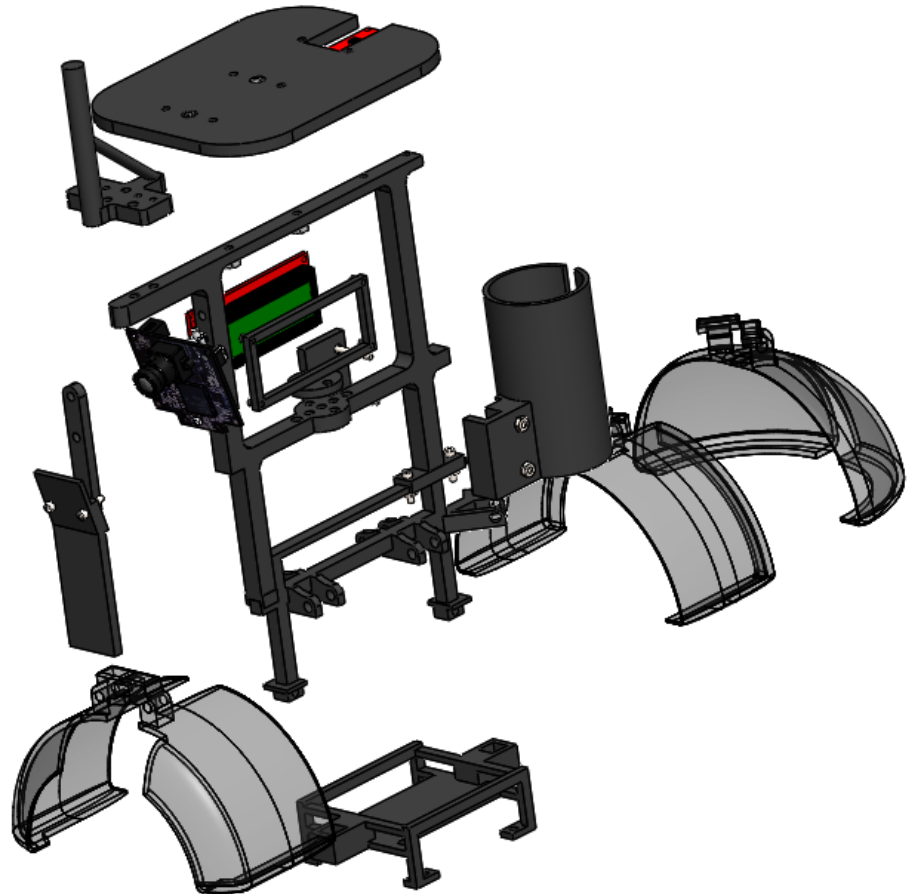


Figure 4.4: Exploded view of electronics scaffolding

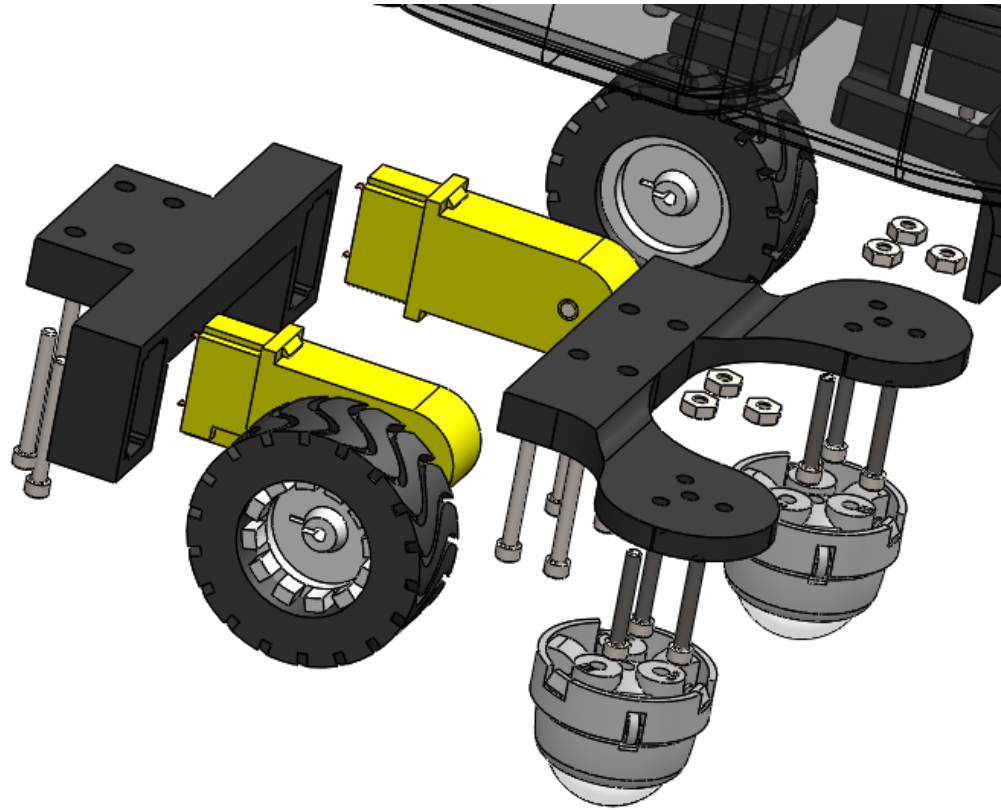


Figure 4.5: Exploded view of motor and caster mount assembly

signed with holes to accommodate #4 screws. A support stance of four points was established by using two driven wheels and two casters. Located at the front of the robot was a Caster Bracket which was attached to two 1" plastic caster balls using #4 screws. On the back mounting bracket tree of the Modular Base, a Motor Mount was used to hold two motors affixed with a bonding agent. These motors have a 3mm diameter, D-shaped output shaft which couples to a plastic wheel with rubber tires. The wheels have a 42mm diameter and have a width of 19mm. These wheels have 12 teeth on the rim which are designed for use with a quadrature optical encoder which can provide up to 48 counters per revolution, though the final design does not utilize these features.

A custom gripper was designed for this iteration of robots to replace the previous off-the-shelf gripper. The gripper was attached to the Modular Base using a pair of #4 screws which went through holes on the Front Panel Holder as well as the Pitch Servo Mount.

The Pitch Servo Mount was then attached to a Hitec HS-5485HB digital servo which was used to raise and lower the gripper. This servo motor connection was supported by the Magnetometer Sensor Mount attached using four #4 screws through both the servo motor and the Pitch Servo Mount. A servo horn provided with the servo motor was attached to the Gripper Servo Mount using two #0 screws. This pitch servo junction also has a #4 screw axle opposite the servo horn connected to the Pitch Servo Mount to further support the Gripper Servo Mount about the axis of actuation. The Gripper Servo, another Hitec HS-5485HB digital servo, is attached to the Gripper Servo Mount and the Gripper Base using four #4 screws. The Gripper Servo actuates two links which transmit torque through a 1:1 gear ratio. These two links act in parallel with two pairs of supporting links which in turn connect to the left and right sides of the gripper end effector. The link junctions between the geared links and the end effector are all aligned using #8 screws as axes to enforce the geometry and proper movement of the actuator.

### **4.3 Assembled Robot**

Figures 4.7 - 4.9 feature images of the completed robots.



Figure 4.6: Exploded view of gripper assembly

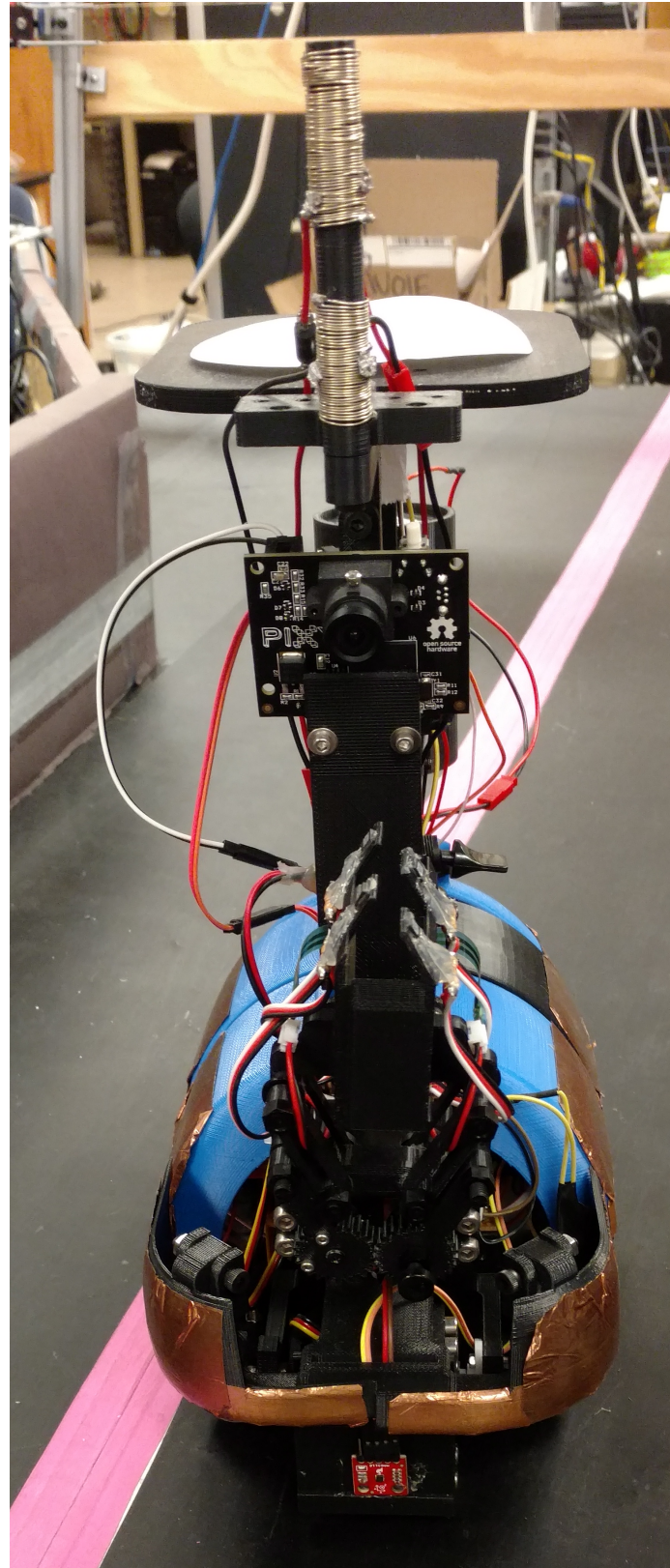


Figure 4.7: Assembled robot from the front

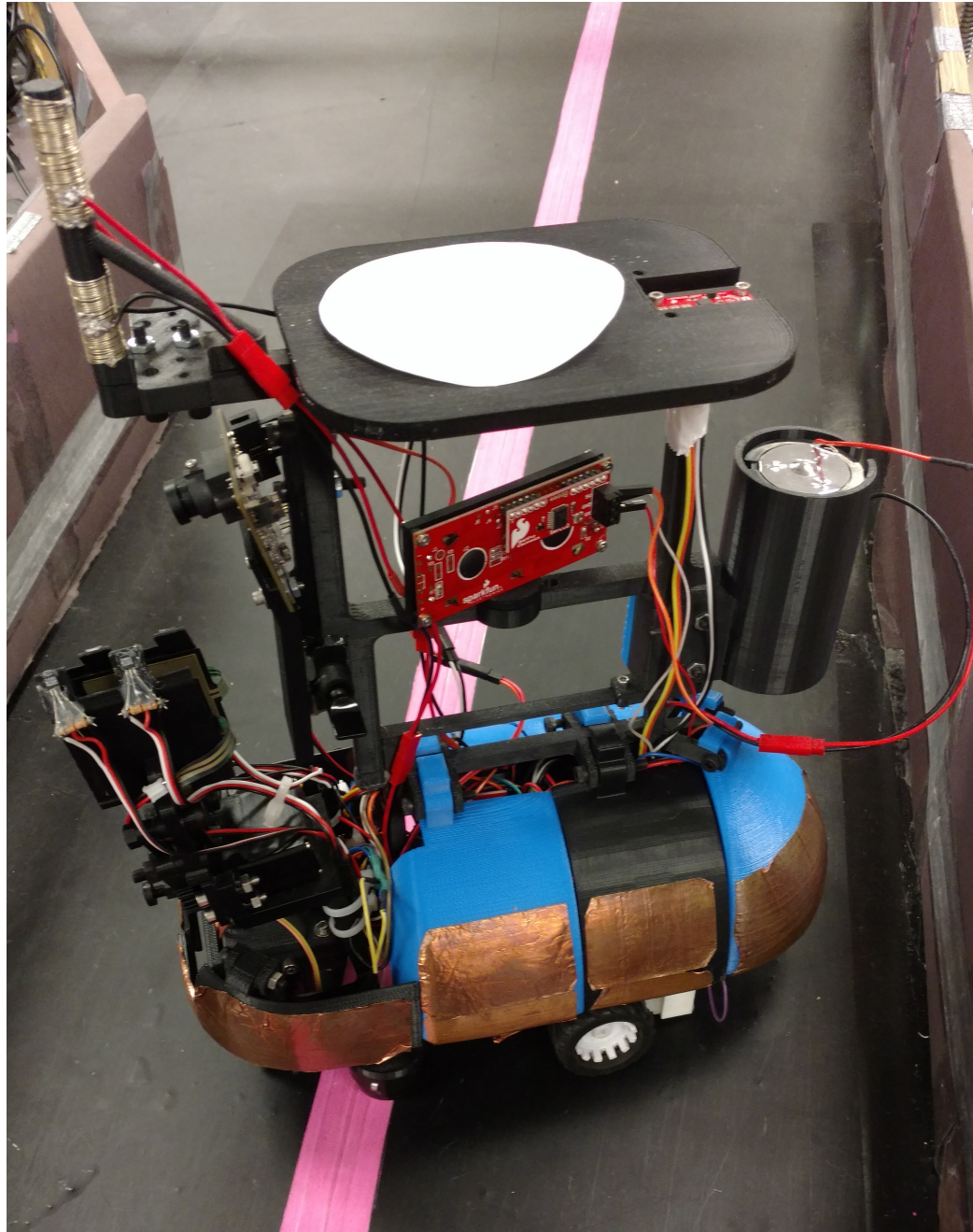


Figure 4.8: Assembled robot from the side

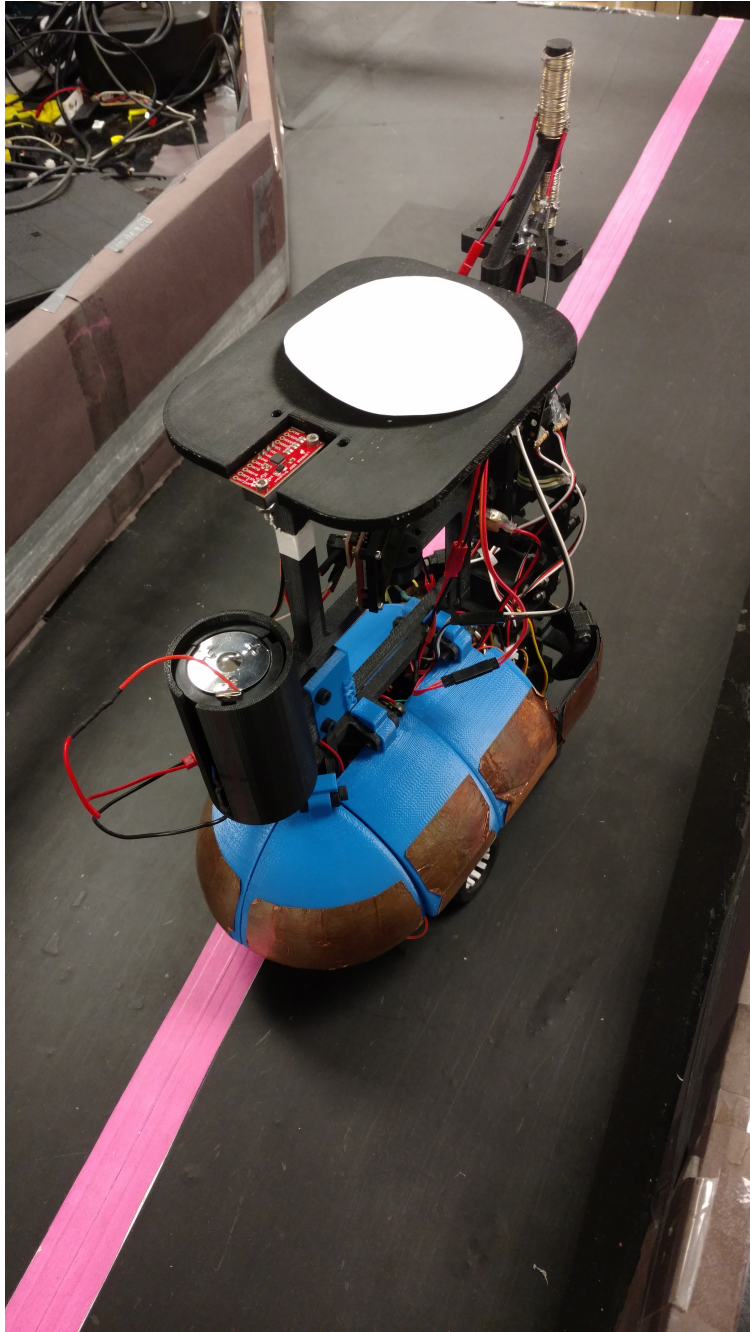


Figure 4.9: Assembled robot from the back

## CHAPTER 5

### ROBOTIC ANT SOFTWARE DESIGN

The redesign of the embedded software architecture and the supporting libraries are discussed below. Software changes were primarily made to improve the robustness of the system, though the behavior implementation was restructured such that combinations of various behaviors could be introduced in a modular fashion and switched on and off easily.

#### 5.1 Arduino Due

All software written for the Arduino Due was developed in a standard text editor and compiled using the Arduino 1.5.7 IDE. The Arduino code features two principle methods, one called `setup()` which executes a single time when the sketch loaded on the Arduino board starts, such as when the Arduino Board is powering up or has been reset. In `setup()`, variable initialization and sensor communications are established. The other principle method is `loop()`, which is simply called repeatedly upon completion of `setup()`. A finite state machine was developed in which a number of boolean states are evaluated within `loop()`; evaluating a particular state to be true calls a method which contains the behavioral code for the state, and traps the control flow of the code until a condition is met which necessitates a transfer to another state. The final step of the behavior is to reset the state vector according to what the next step of the finite state machine should be, upon which the behavior method returns the control to `loop()`, which evaluates the state vectors and passes control to the next behavior. The overarching finite state machine of the robot is given in Figure 5.1, with the finite state machines of each individual behavior given in Figures 5.3-5.10.

As seen in Figure 5.3, the main control loop of the software controls which of the eight principle behaviors are executed. The `goingInMode()` method is used to control

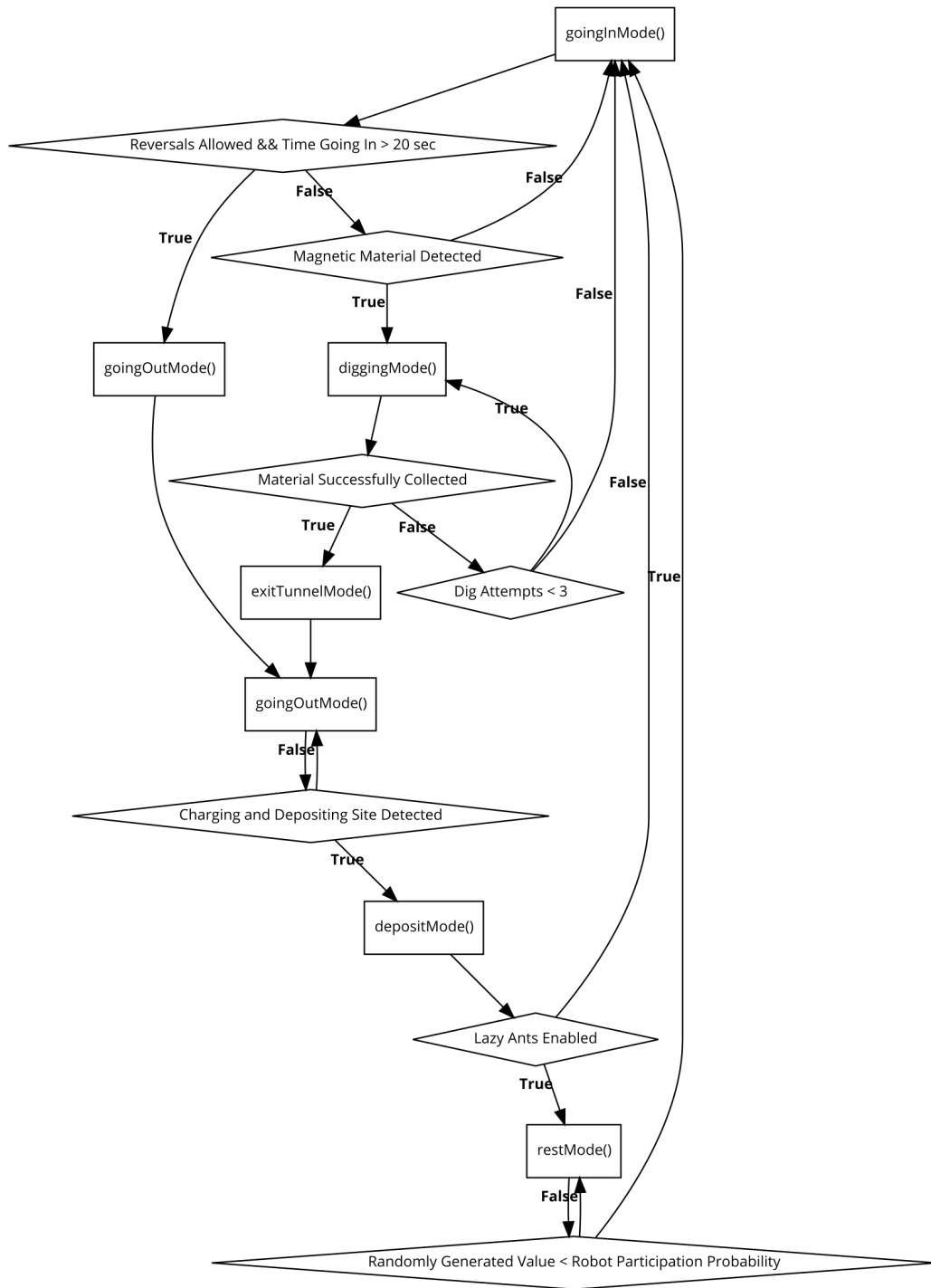


Figure 5.1: Overview of robot ant state machine modes and transitions

Table 5.1: Summary of Robotic Ant States

State Method	Behavior
<code>goingInMode()</code>	Navigates towards excavation site
<code>diggingMode()</code>	Picks up material at excavation site
<code>exitTunnelMode()</code>	Moves away from excavation site
<code>goingOutMode()</code>	Navigates towards charging and depositing site
<code>turnHeading()</code>	Turns the robot to face the desired orientation
<code>depositMode()</code>	Deposits excavated material
<code>restMode()</code>	Allows the robot to be “rest”

the robot as the agent navigates within the tunnel from the charging and depositing site towards the digging site. When the robot detects the presence of magnetic material using the MAG3110, the robot then transitions from `goingInMode()` to `diggingMode()`.

The code of `diggingMode()` makes attempts to grasp the cohesive material, with successful attempts being sensed using the force sensitive resistors within the robot gripping mechanism. In addition to the force sensitive resistors, the robot could also poll the Hall effect sensors on the gripper mechanism to modulate the movement of the gripper over the period of the digging attempt. If the Hall effect sensors did not indicate the presence of any magnetic fields, it is possible that further digging attempts will not be successful, and the behavior control returns to `goingInMode()`.

In the event of a successful digging attempt, the robot will then execute `exitTunnelMode()`, a unique behavior which is specific to movement near the excavation site. Previously, the robot ant would immediately attempt to turn around after a successful dig, congesting the system and hindering the ability of the other robots in the area to move efficiently. `exitTunnelMode()` is a time-based method which utilizes the Pixy camera to control the motor signals such that the robot moves backwards along the pink line. After the robot has backed up a certain period of time, `exitTunnelMode()` returns and `goingOutMode()` is called.

The `goingOutMode()` method was used to transport the robot from a point in the tunnel to the charging and deposit site, which effectively follows the simulated pheromone

trail of the tunnel until the charging sensor makes contact with the charging wires of the terminal site. At this point, the robot engages in a material depositing motion which attempts to shake the magnetic material out of the gripper. When the magnetic material is no longer sensed by the force sensitive resistors of the gripper, the robot has completed a full depositing cycle, and returns to `goingInMode()`.

Observations made while studying the tunneling behaviors of biological ants informed the inclusion of two behaviors: reversals and probability-based laziness [33]. Biological ants have been observed to give up on digging attempts if they are unable to reach the tunnel tip, even when the ant is within several body lengths of the digging site. This behavior was implemented using a time-out methodology, which can allow the robot to abandon `goingInMode()` after a certain time-period has been spent in the method. This event is immediately followed by `goingOutMode()`, after which the robot visits the charging and deposit site but does not exhibit any of the unnecessary material depositing behaviors.

These ant populations have also been observed to exhibit an uneven workload distribution within the worker population. In order to emulate the effects of workers abstaining from excavation, a set of parameters were implemented which could be used to moderate how “industrious” each particular robot behaved. Within `depositMode()`, which is always called after `goingOutMode()`, the robot may make a call to `restMode()`, which has the ability to trap the control flow of the robot and force the robot to rest. The robot evaluates a random number every twenty seconds, and if the random number is less than the robot parameter which determines the work probability, then the robot returns to the typical state machine and makes a call to `goingInMode()`. It is possible to individually tune the work probability of each robot such that an ensemble of robots can be deployed, some of which are perpetually engaged in the digging process and others which do not attempt to dig a single time.

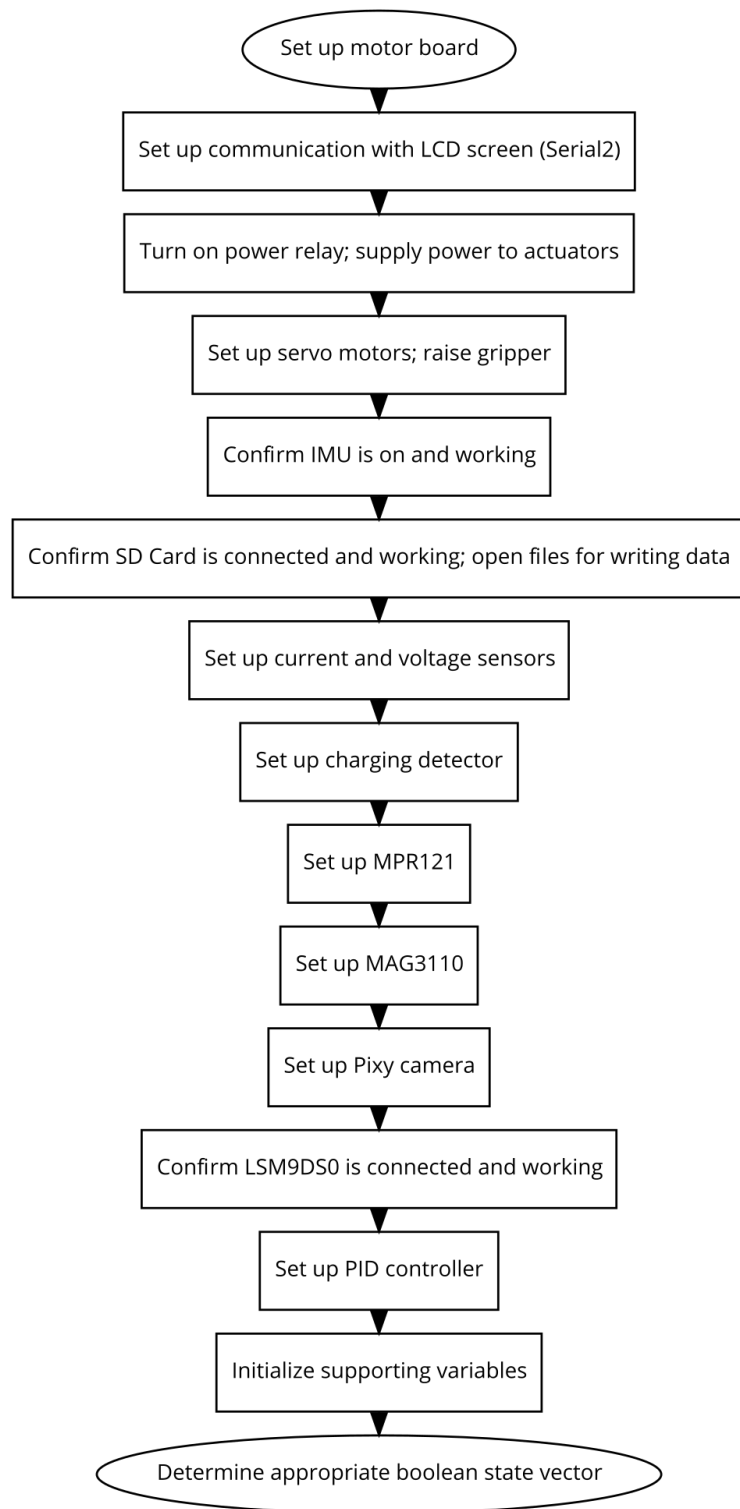


Figure 5.2: Overview of robot ant setup ( )

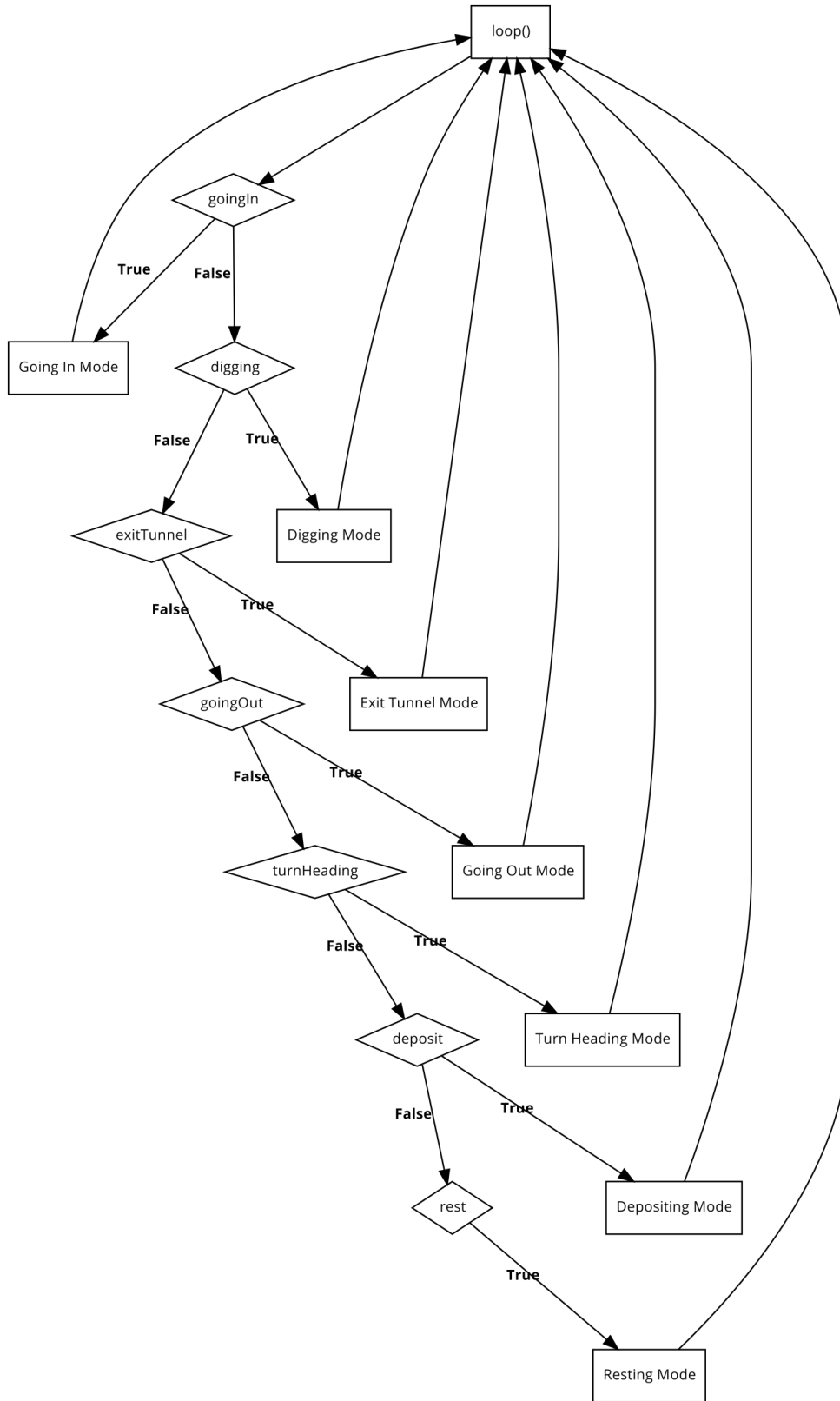


Figure 5.3: Overview of robot ant loop()

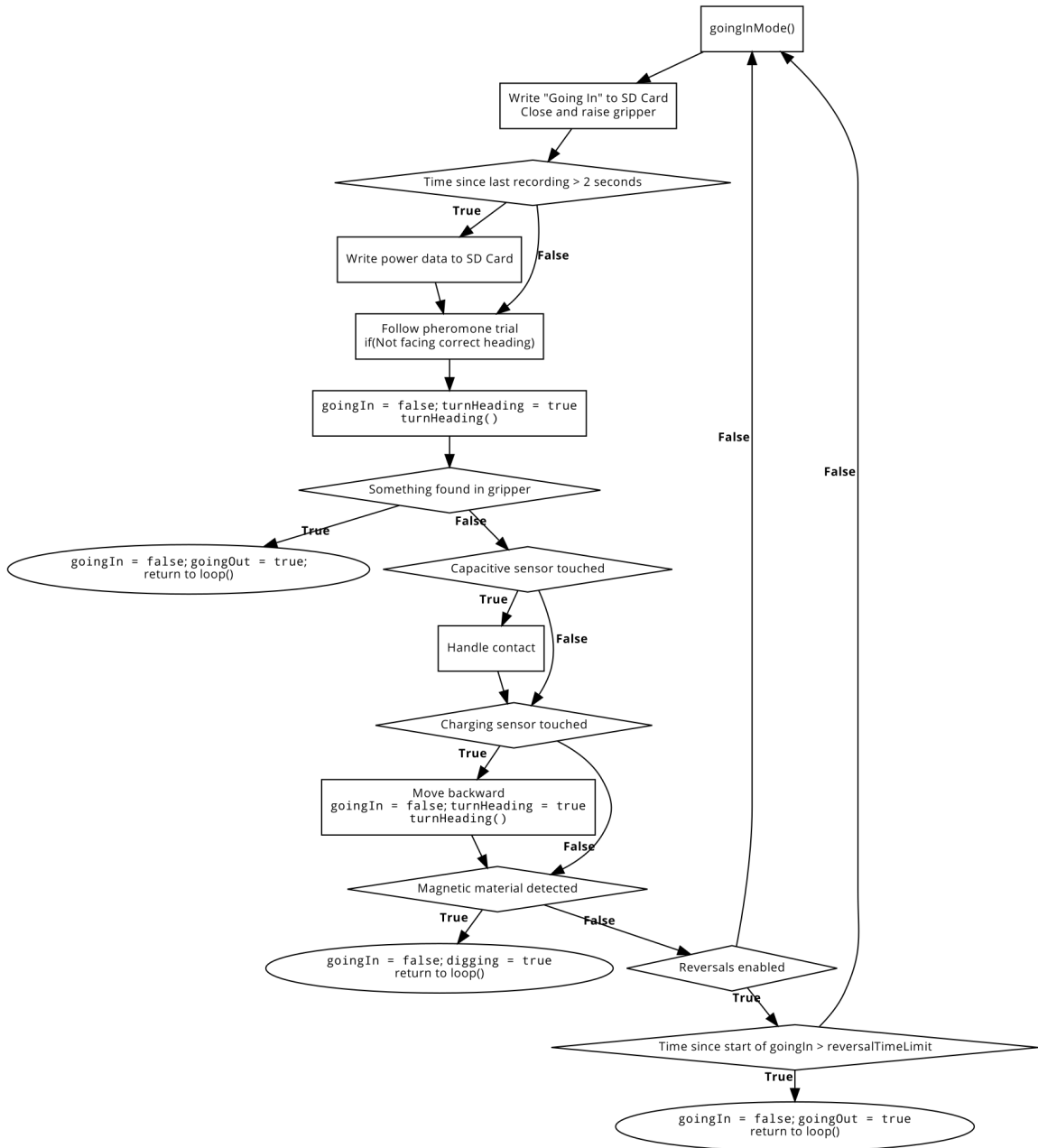


Figure 5.4: Overview of goingInMode ( )

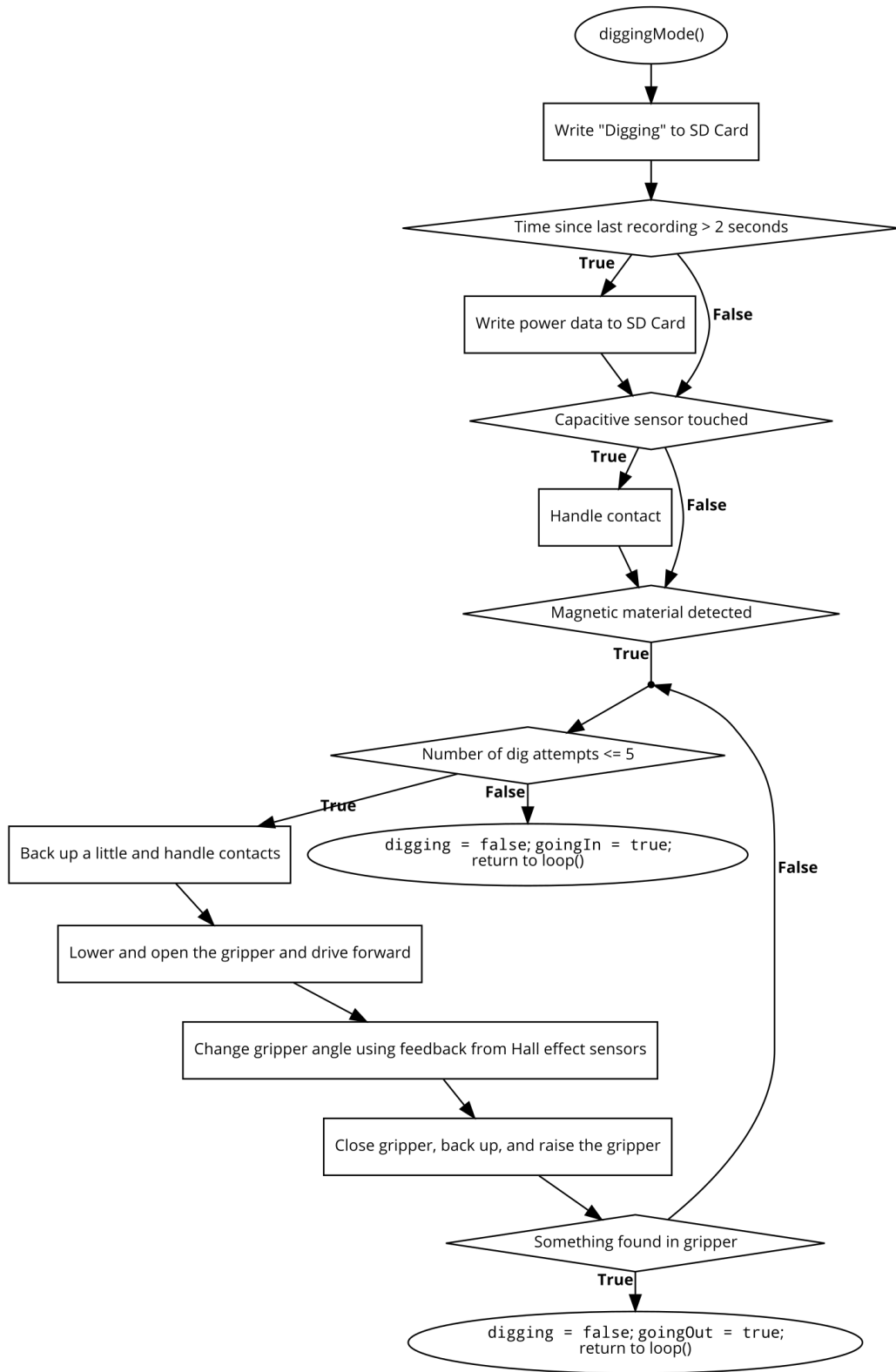


Figure 5.5: Overview of diggingMode ( )

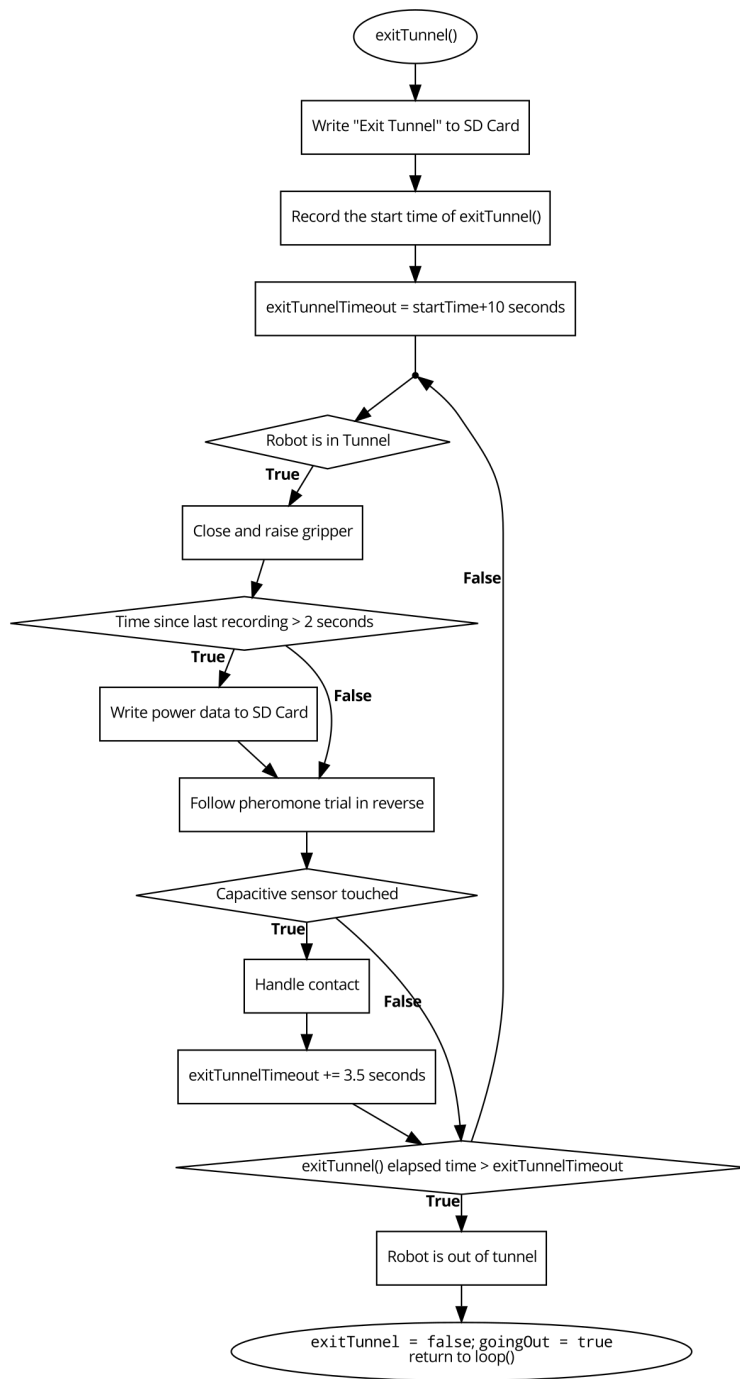


Figure 5.6: Overview of `exitTunnelMode()`

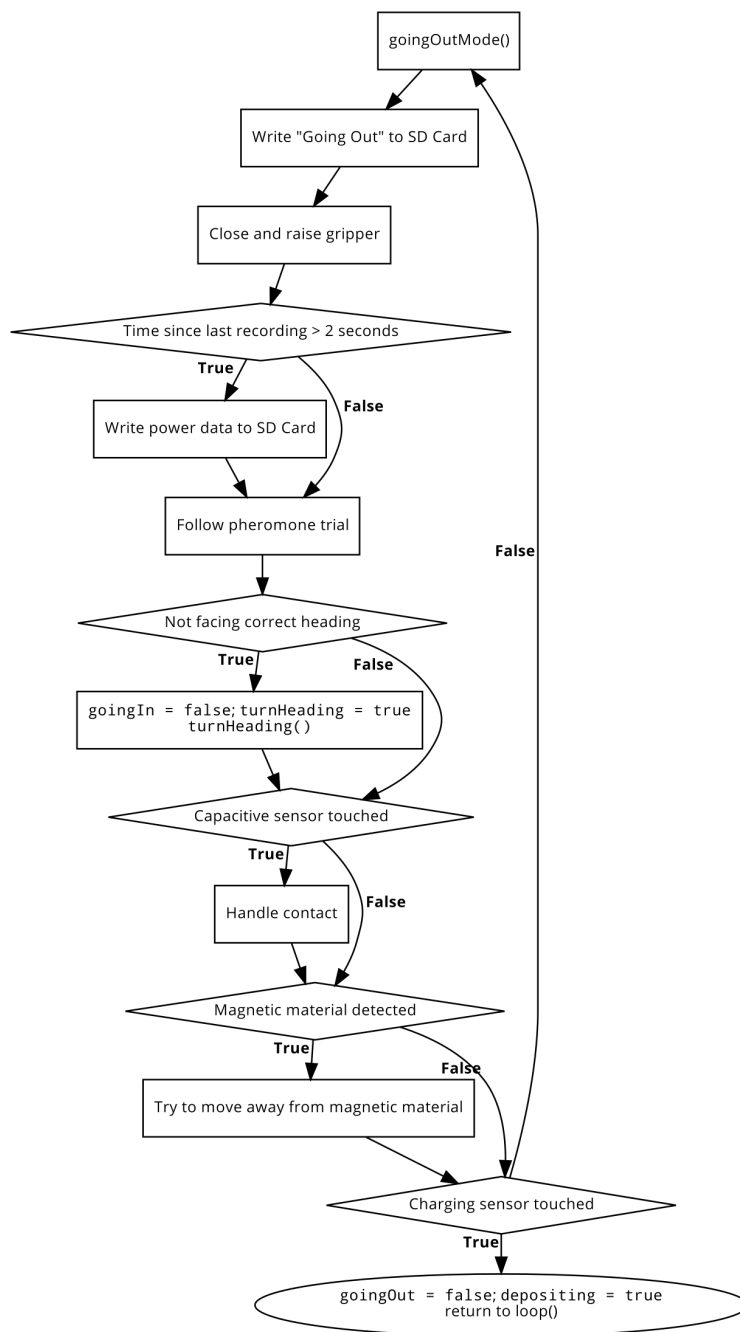


Figure 5.7: Overview of goingOutMode ( )

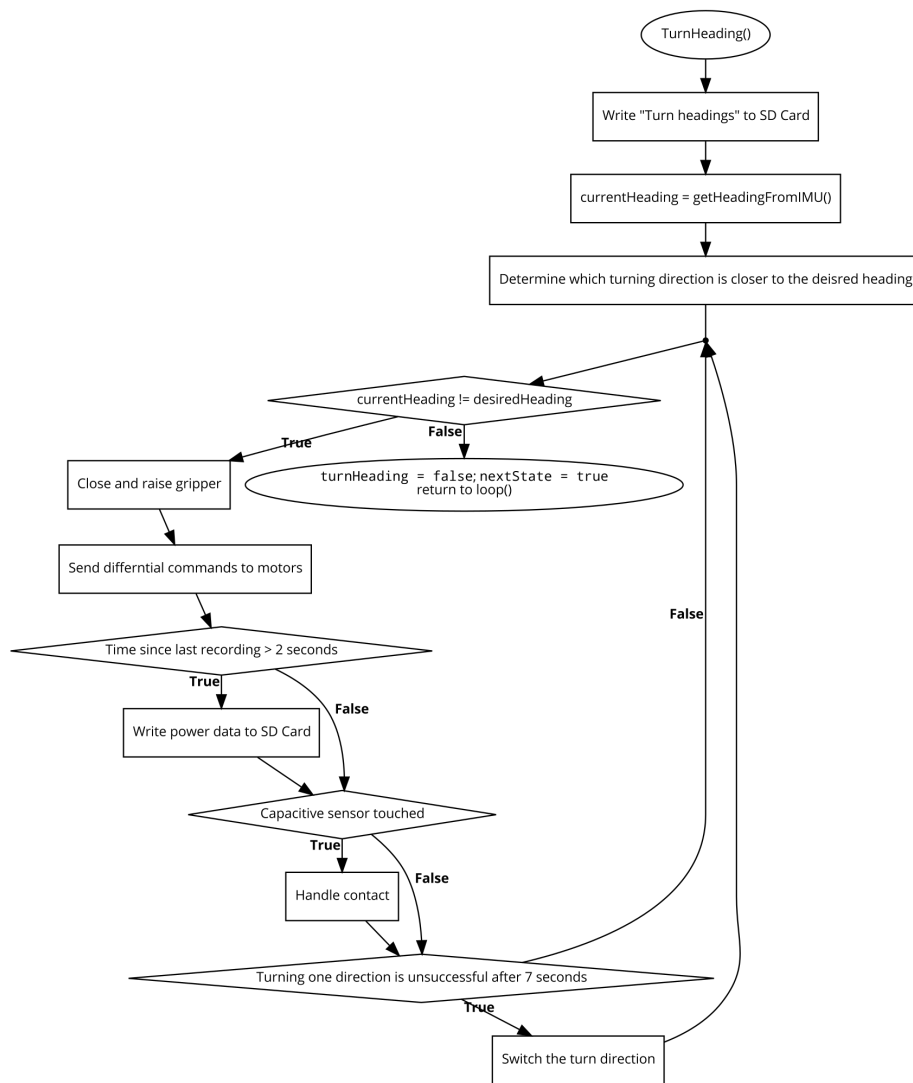


Figure 5.8: Overview of turnHeading ()

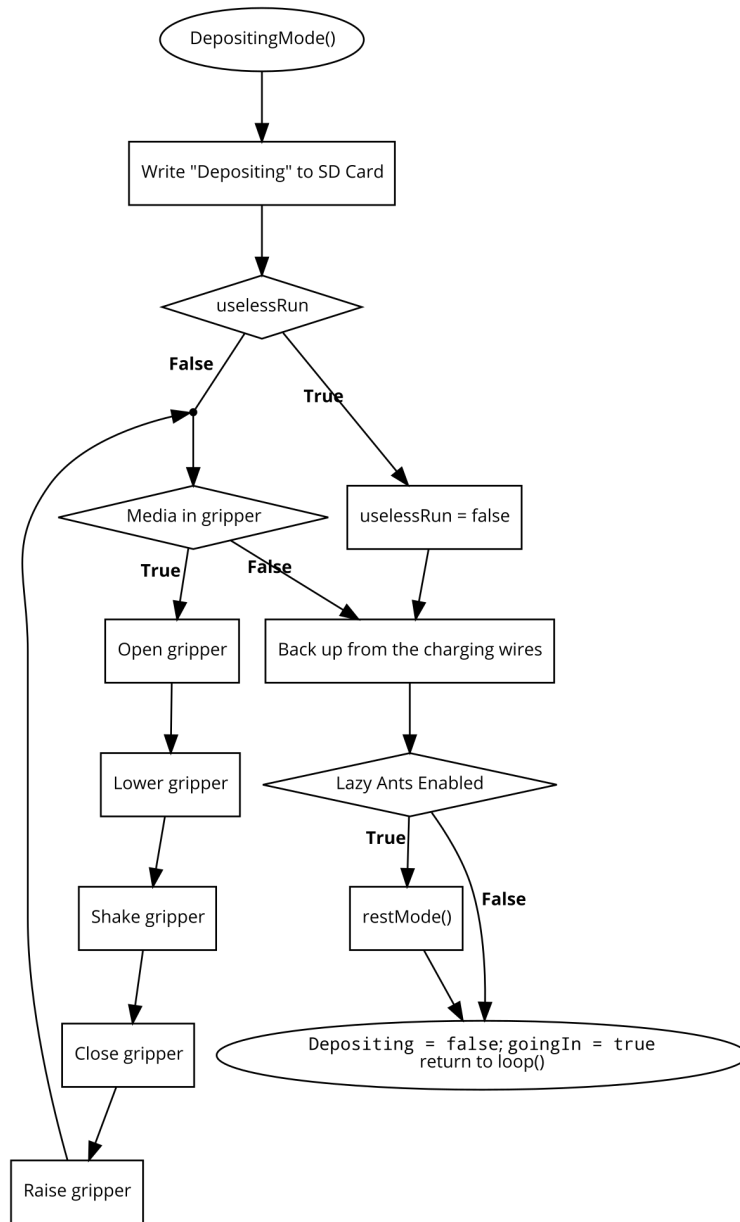


Figure 5.9: Overview of depositMode ( )

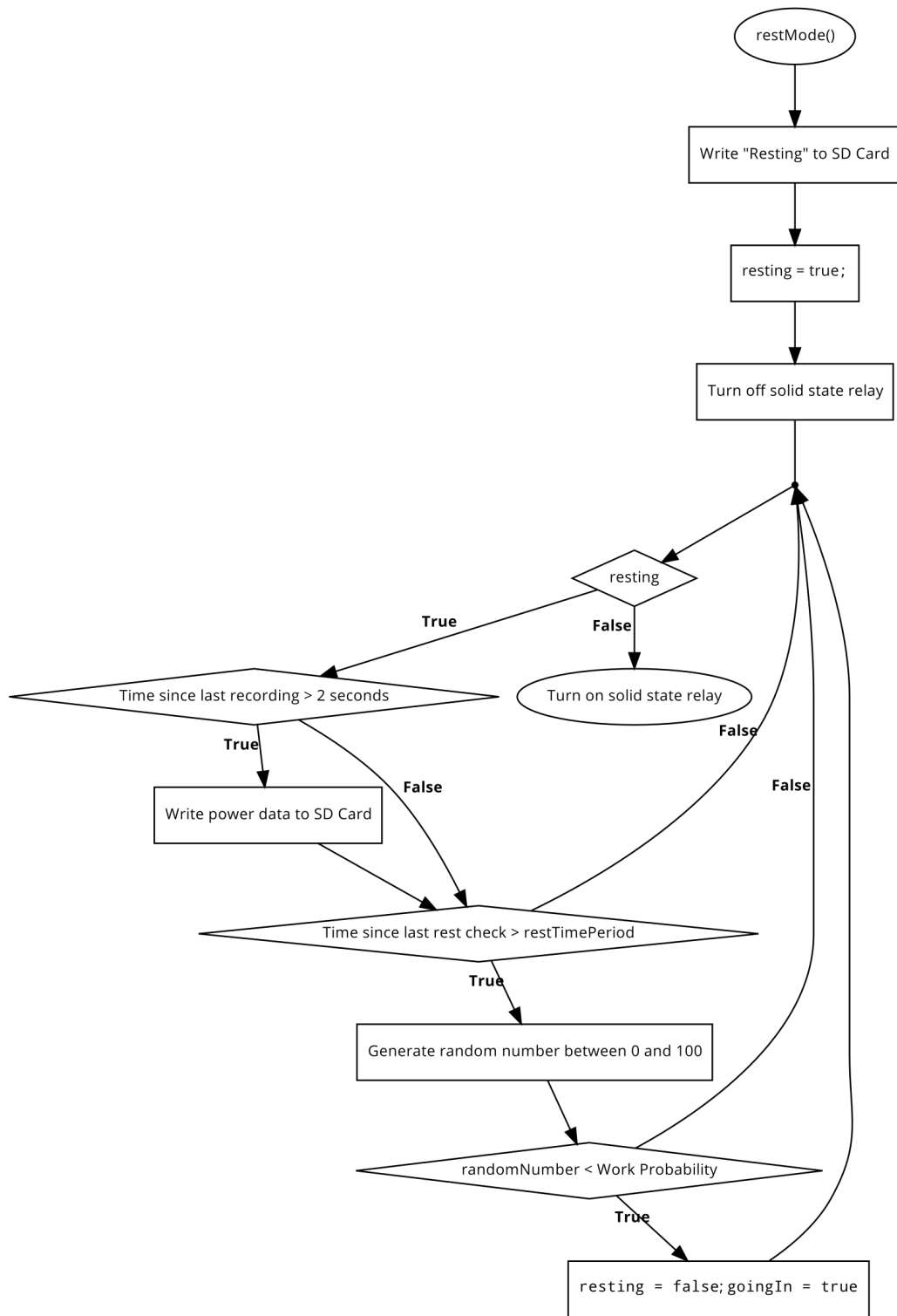


Figure 5.10: Overview of `restMode()`

## 5.2 Pixy Camera Supporting Software

Previous versions of the Pixy camera software libraries were prone to hanging the entire robot in the event of communication errors arising between the Arduino Due and any of the other sensors. This issue was particularly problematic for the Pixy camera due to the power lines previously being connected to the motors and servos, which could disrupt the Pixy camera operation in the event of a power spike typically caused by mechanical stalls of the actuators. Several modifications were made to eliminate such system compromising hangs.

As seen in Chapter 3, the power supplied to the Pixy camera is now driven by the Regulated +5V pin of the Arduino Due along with other low-power sensors such that actuator-driven power consumption spikes are sufficiently isolated from all sensors. Since isolating the actuating circuits from the rest of the sensors, no system communication hangs related to insufficient power have been observed. However, if for some unforeseen reason the power consumption were to temporarily exceed the capacity of a component on the robot without causing permanent damage, the new software and electronic architecture are designed such that the robot can detect the disruption and undergo a system reboot in order to reestablish all communications.

In addition, the software libraries supporting communication and interpretation of signals from the Pixy camera utilized numerous state machine blocking loops which indefinitely captured the state of the robot, effectively locking the system in whichever state was being executed during the hang with no opportunity to exit. Problematic snippets of code were modified such that the state machine could return in the case of a system fault and prompt a system reset to reestablish communications.

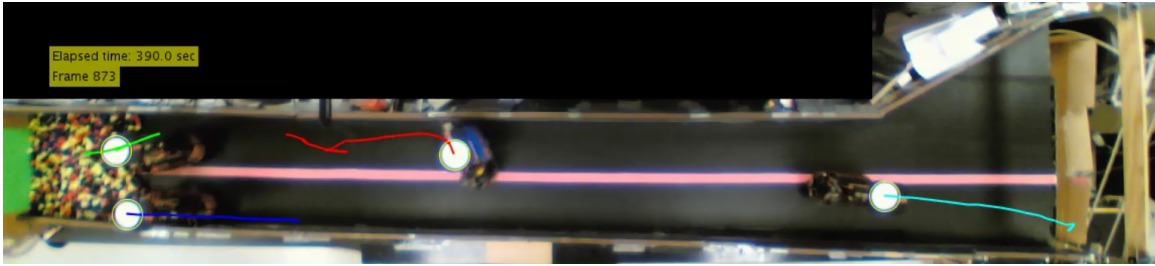


Figure 5.11: Example of the Hough transform image processing. The tunnel length is approximately 20 robot body lengths

### 5.3 MATLAB Vision Tracking System

In order to track the robots as they moved about the tunnel, a tracking system was developed in MATLAB which could accurately follow each robot and appropriately distinguish each robot from one another in the event of a collision.

A webcam was fixed above the test bed, which would capture a frame at a frequency of 3Hz. Higher frame rates were considered, though they produced cumbersome amounts of data, while lower frame rates were unable to accurately and uniquely track each robot correctly in highly congested systems.

Background subtraction methods were considered, though algorithms which relied on these methods were found to fail as the tunnel propagated over the period of a trial and the environment in which the robots operated changed. Ultimately, each robot was marked with a white circle which contrasted the dark robots and dark tunnel well. A Hough transform was implemented which identified circles of the appropriate marker radius within the webcam image. An example of the processed image is given in Figure 5.11, with the colored trails indicating the positions of the robots over the previous twenty frames.

In addition to the machine vision processing, the data recorded by the robots to the onboard microSD cards were also loaded and analyzed in MATLAB.

## CHAPTER 6

### ROBOTIC ANTS RESULTS AND DISCUSSION

The results of the modifications made to the various components of the ant robot platform on the overall system are reviewed below. Data from preliminary trials are reviewed, followed by a discussion regarding the design of the *next* permutation of the ant robot platform.

#### 6.1 Observations

Biological ants are dynamic agents which are able to intelligently navigate complex situations within the tunnel, and are hypothesized to use a number of locally observed parameters to inform the expressed behaviors to efficiently navigate the tunnel network. The robot behaviors were designed to handle events in a general manner, with no code written for any specific state. These behaviors are not guaranteed to be the optimal solution, though this abstraction may be important in the overall preservation of behavioral continuity in the context of active matter systems. A review of observations made regarding the robot capabilities, with a comparison of the previous ant robot platforms, is provided below.

##### 6.1.1 Granular Media Manipulation

The interaction of the robot with the granular media can be broken up into three periods: excavation, transport, and deposition. It should be noted that previous iterations of the robot platform approached the solution of digging in a different context. The first granular media used was cotton, which was grasped using an off-the-shelf gripping mechanism which could sense the presence of cotton using an infrared detector which looked at the cavity of the gripper where the cotton would be held. While the excavation routine in the software has remained relatively similar, the media and the gripping mechanism have been

modified significantly.

The use of a magnetic granular material as the excavated media is a more appropriate emulation which captures the type of material manipulation problems that biological ants must address in the process of digging. The off-the-shelf gripper was replaced with a custom 3D printed gripper mechanism, actuated by an upgraded pair of servos, and outfitted with a new suite of sensors that are able to reliably determine the presence of material using the force sensitive resistors and evaluate the potential of a digging routine to grasp material via the Hall effect sensors.

After excavation, the robots have been shown to transport the material well, with few dropped pellets populating the tunnel; collisions with other robots or the tunnel walls are the factors which contribute most to dropped pellets.

When the robot has reached the end of the tunnel and has detected the depositing site, the media is deposited into a container beyond the boundary of the tunnel, such that the material is effectively removed from the robot operating environment. Future works have been proposed which operate in a fully enclosed environment where all media in the tunnel remains within the system over the period of the experiment. Robotic behaviors could be developed to probe the various aspects of stigmergy which inform the modification and construction of an artificial nest through the rearrangement of the media, instead of the expulsion of the material from the system.

The new gripper mechanism is able to grasp larger quantities of the material and detect the material well, though there have been some issues in terms of consistency and efficacy. The 3D printed components of the gripper have a non-negligible compliance which can cause some particles to be lost as the robot attempts to pick up a packet of pellets from the bulk of the media at the excavation site. The packets of the magnetic material are difficult to remove from the bulk at the excavation site, which can stall the gripper servos. At the deposit site, two pellets of the magnetic material could be attracted to one another through the palm of the gripper which is then held against the force sensitive resistor. This

would prevent the robot from being able to drop either pellet, and the pellet on the side of the force sensitive resistor would cause the robot to, correctly, identify the presence of a pellet in `depositMode()`, effectively trapping the robot as it perpetually tries to deposit a pellet which it can not effectively move. Future iterations of the gripper could explore geometries which mitigate these issues, as well as a control feedback schema which can monitor the current draw of the servo motors to better modulate the commands sent to the actuators.

### 6.1.2 Navigation

As in previous iterations, the robot used the Pixy camera and an improved IMU to navigate in the tunnel. The Pixy camera was used to sense a simulated pheromone trail and the IMU gave the robot a sensitivity to magnetic fields, capturing a number of senses that ants have been shown to use in coordinating navigation. The robot capability to consistently navigate in the tunnel, both towards and away from the excavation site, even in the presence of other robotic obstacles was found to be rather robust.

After the development of the platform, literature pertaining to the use of a sort of dead-reckoning algorithm in another social insect was discovered. While this method has not been demonstrated in ants, a study reported by Bardunias and Su report evidence for the use of idiothetic dead reckoning in the formosan subterranean termite, *Coptotermes formosanus* [34], which may be informed by something akin to a step-counting process. As mentioned in previous sections, encoder-based solutions are prone to error accumulation in the event of agent interactions which cause the robot to displace without the rotation of the motor. Because congested systems of robots undergo numerous collision interactions over the course of the trial, off-the-shelf encoder-based implementations may be inadequate, though a more complex solution may be a fruitful investment in the future.

### 6.1.3 Precision

While the overall excavation site width was approximately equal to the width of three robots, improvements to the Pixy camera PID control method enabled the robots, when unobstructed digging was possible, to consistently dig near the same central point of the tunnel. As a result, the robots were capable of digging tunnels which were approximately equal to the width of the robot, such that the robot could navigate not only the overall tunnel, but also the self-built tunnel in the bulk of the media. However, the precision of the Pixy camera-PID controller was not as high when the robot moved backwards, such that the robot was unable to successfully reverse out of the tunnel. This problem was aggravated by the fact that the robot wheels were unable to maneuver over the granular media, such that robot could become stuck within the narrow tunnel it had excavated. This issue ultimately prompted the design of a new robotic platform with the capability of moving *on* the granular media, which will be described further in Section 6.3.

### 6.1.4 Robot Interactions

The capacitive sensor panels implemented on the new platform were able to consistently identify the difference between contacts with the tunnel walls and other robots. The current implementation of the software which supports these panels has only small variances in the responses to the two different types of contacts, which are handled in a case-dependent system. However, timing-based implementations could be utilized in the future, such that the robot could infer the agent density within the tunnel based on the frequency of contacts in a given period of time. An implementation which tracked this data in a time-sensitive fashion could be particularly useful in developing a new reversal schema which utilizes a contact frequency threshold as opposed to the current implementation which used a simple timeout method to determine when the robot cancels the excavation attempt and returns to the charging and depositing site.

### 6.1.5 Processing Capability

The Arduino Due continues to have sufficient processing capabilities to manage all of the sensory inputs effectively. The future iterations of robots, discussed further in Section 6.3, may require a more capable processing board, which could support higher level machine vision algorithms, dependable wireless communication, and motor control algorithms to support the gaits of the new legged platform.

## **6.2 Preliminary Data**

### *Power Consumption*

Onboard data recorded to the microSD card were loaded and analyzed in MATLAB after each trial. An example of data collected for a trial of two robots can be seen in Figures 6.1-6.3. The data presented represent the battery conditions of two separate robots operating simultaneously in the same tunnel. The power consumption for the two robots are comparable over a period of time, though spikes can be seen in the power consumption of Robot 1, which were reviewed using the webcam footage. These spikes correlate to periods in which the two robots interacted with one another, which happened to leave Robot 1 in a stalled state for brief periods of time.

### *Space-Time Dynamics*

The tunnel density could be monitored by projecting the tunnel coordinates of the robots from the Hough transform algorithm onto a 1D line, which can be tracked over a period of time. An example of the several space-time diagrams for ensembles of varying numbers of robots is seen in Figure 6.4. Given a behavior profile in which each robot is always engaging in some sort of excavation task, as the number of robots in the system increases the congestion within the tunnel can be seen to increase, with significant jams seen at the digging site, as seen in the four robot ensemble of Figure 6.4.

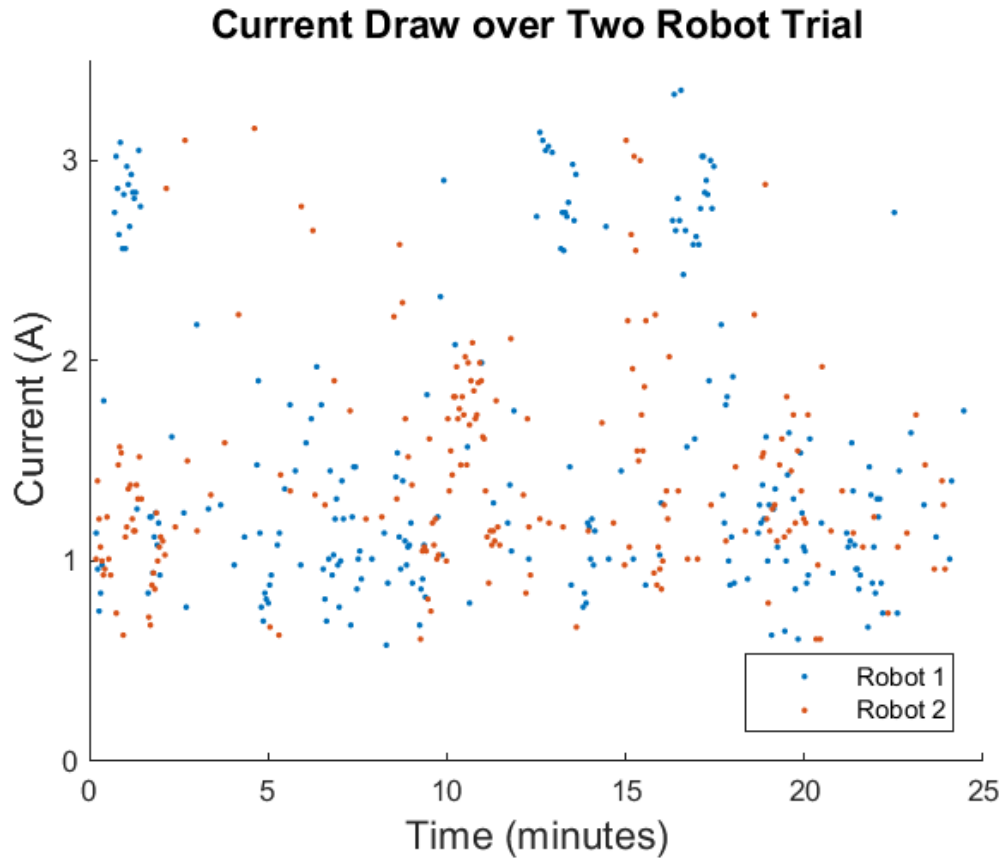


Figure 6.1: Current drawn by two robots over the course of a trial

In the future, data will be collected which utilizes the reversal and lazy behaviors of the robots in order to examine the effect these social protocols have on the overall system dynamics and productivity.

### 6.3 Conclusions and Future Works

This robotic platform, like previous iterations, is incapable of moving on the granular media it excavates. This restricts the types of algorithms which can be explored to material transport-related implementations, with the possibility for a 2D stigmergic implementation that has yet to be explored. In contrast, biological ants are effective locomotors in the tunnels of the media they excavate, and are able to run through the networks of tunnels in all orientations.

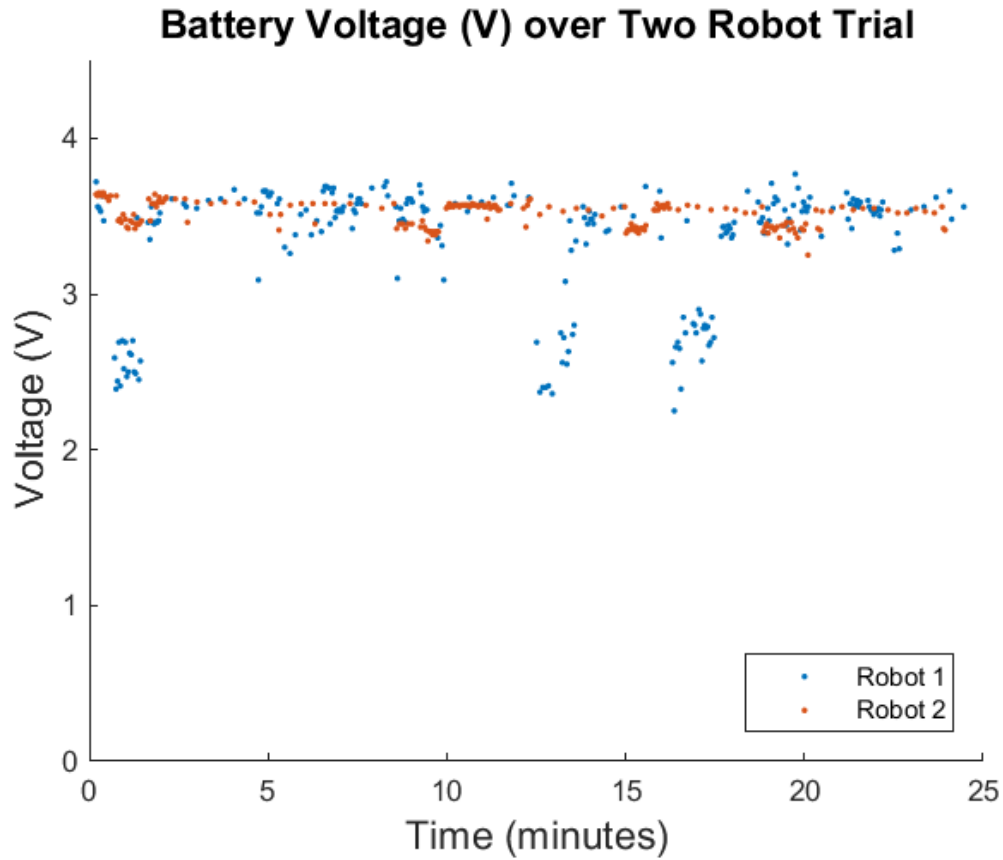


Figure 6.2: Battery voltage of two robots over the course of a trial

The latest work on the ant robots has been implementing a locomotion system such that the robots can maneuver on the granular material they excavate. By enabling them to move over the material they manipulate, we will be able to explore more complex swarm behaviors which more intimately interact the environment. Previously the robots were limited to emulating a sort of material transport problem, though this new platform will enable the system to probe issues related to stigmergy and environment construction.

The new platform, seen in Figures 6.5-6.7, draws inspiration from a number of platforms such as RHex [35], which implement a mechanically simple leg-like mechanism composed of a single compliant leg which rotates about a revolute joint actuated by a brushed DC motor. Quadruped [36] and hexapod [35] platforms have been reported in literature to have notably robust movement capabilities over uneven terrains, and recent work

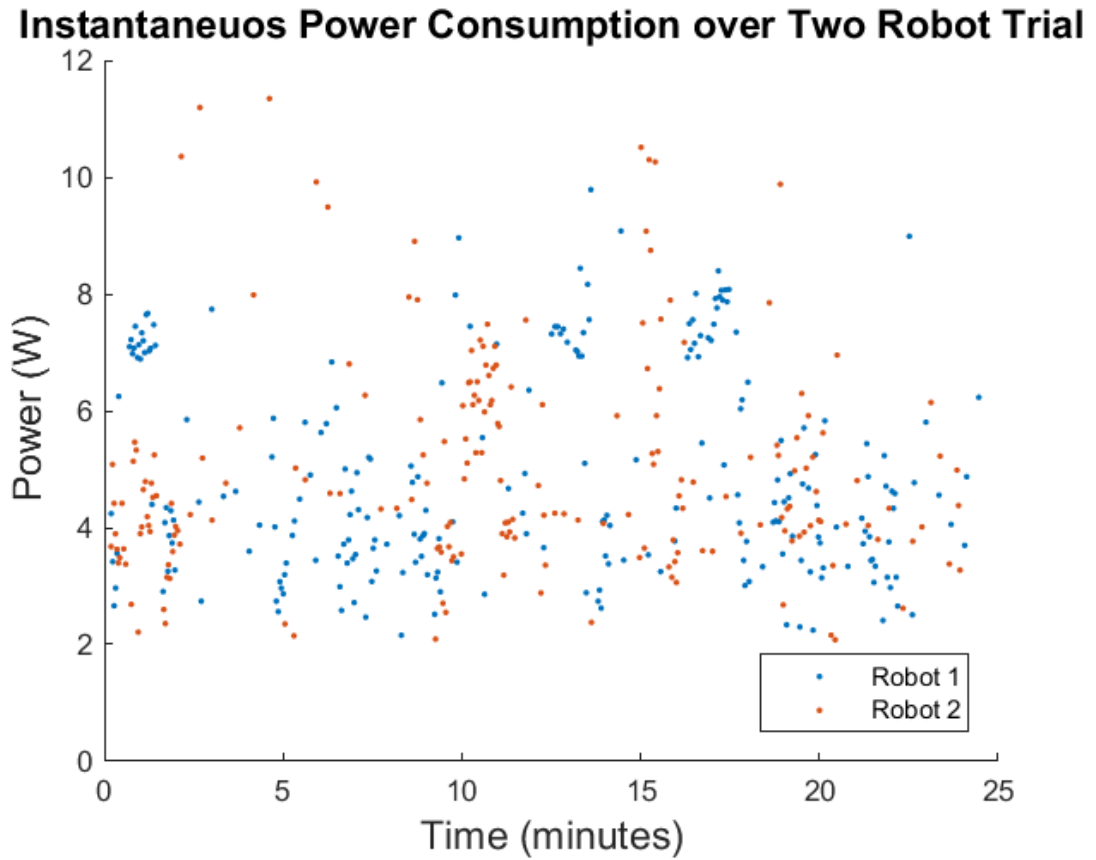


Figure 6.3: Instantaneous power consumption of two robots over the course of a trial. The voltage drops of Robot 1 correlate to periods in which the two robots interacted with one another, which happened to leave Robot 1 in a stalled state for brief periods of time.

conducted in CRABLab on the use of Hildebrand diagrams [37] can be synthesized with previous lab research [4] regarding locomotion on granular media to develop optimal leg geometries and gaits for the new legged platform.

Future iterations of the robot platforms may benefit from an improved power supply, which could in turn support more powerful motors enabled with sensory feedback such that true gaits of organisms can be emulated and tuned to perform on the various surfaces the robots move over.

In the future, a redesign of the test bed may consider separating the charging regions from the depositing regions in order to reduce congestion at the tunnel “entrance”. Congestion at the tunnel entrance region was observed, which had the potential to develop in

cases where sufficient numbers of robots were behaving lazily, thereby reducing the ability of the industrious robots from depositing efficiently. By partitioning these two regions, with the resting site somewhere *beyond* the depositing site, the lazy ants can effectively be prevented from constraining the geometry of the system.

## Space-Time Diagrams

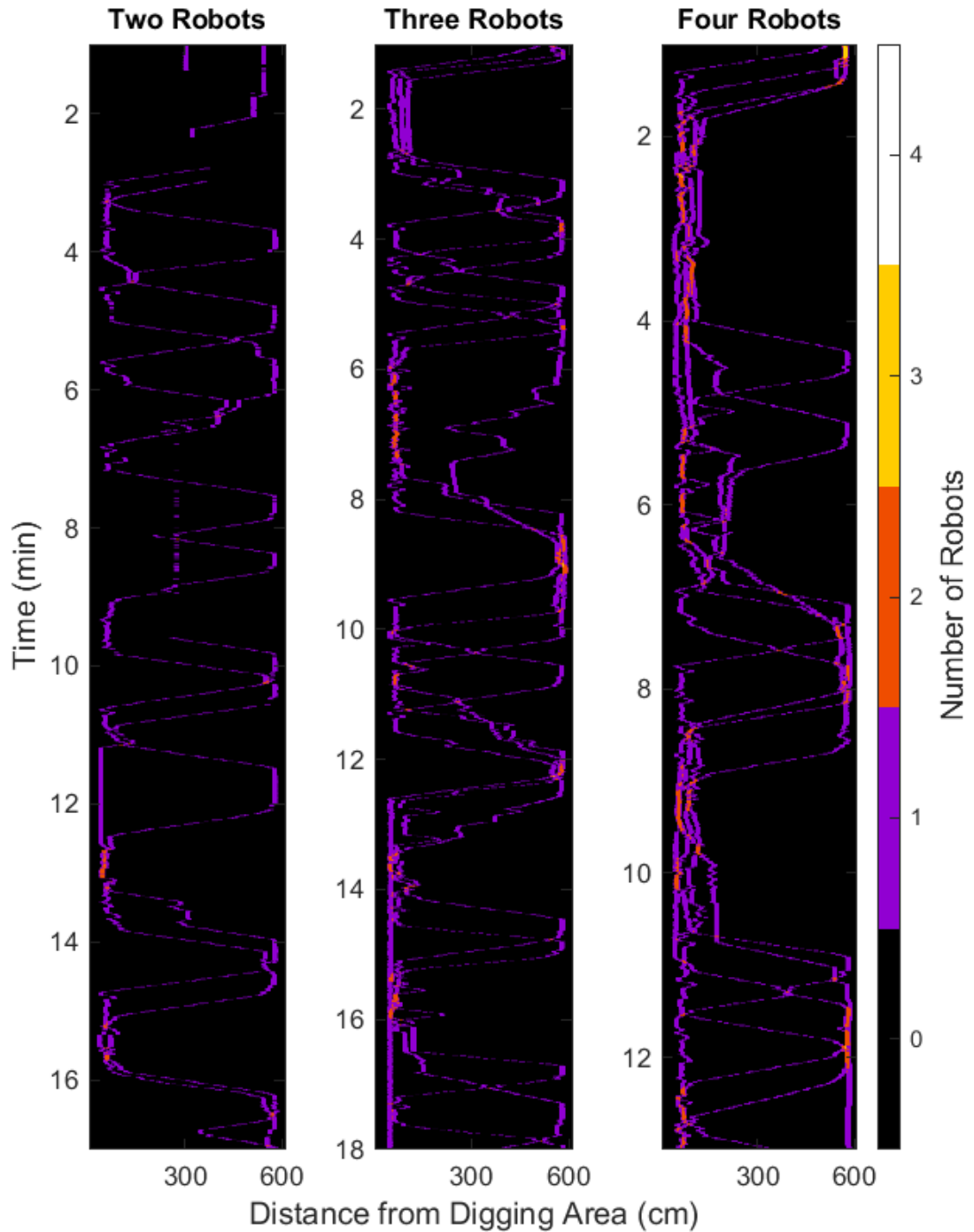


Figure 6.4: Space-time diagrams for ensembles of eager robots which always participate in excavation. Eager robots act to greedily optimize individual excavation rate, at the cost of the global excavation rate.

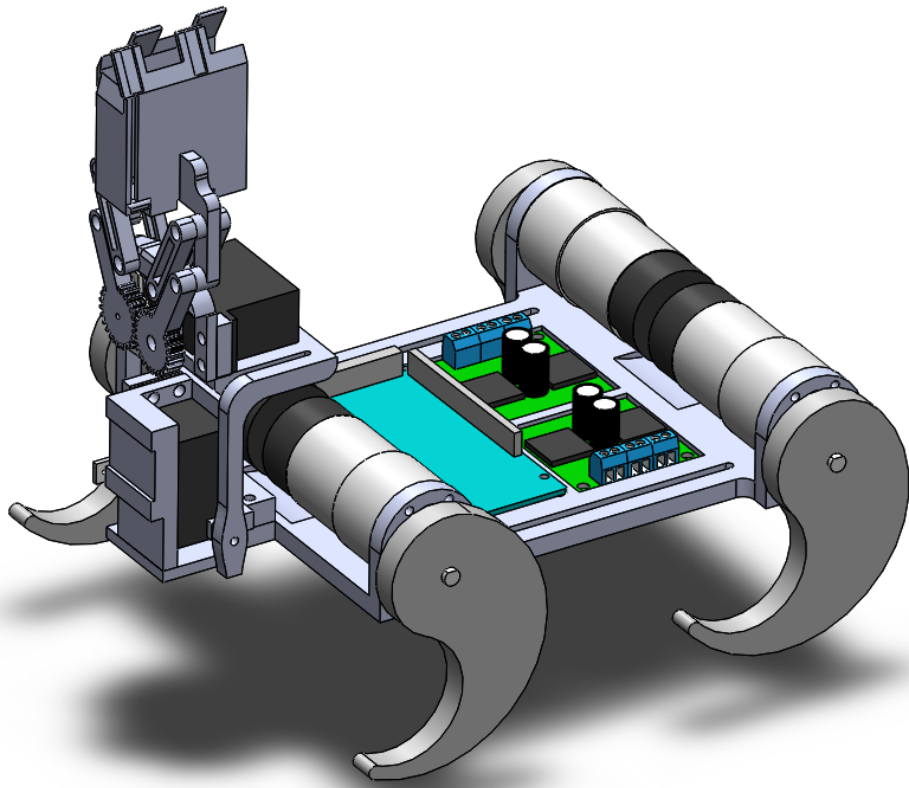


Figure 6.5: Isometric view of new robotic ant platform with C-shaped legs

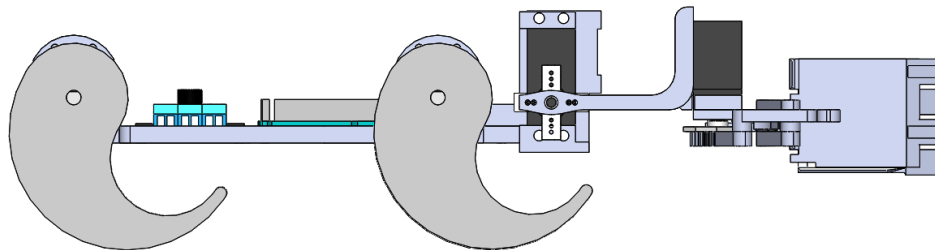


Figure 6.6: Side view of new robotic ant platform with C-shaped legs

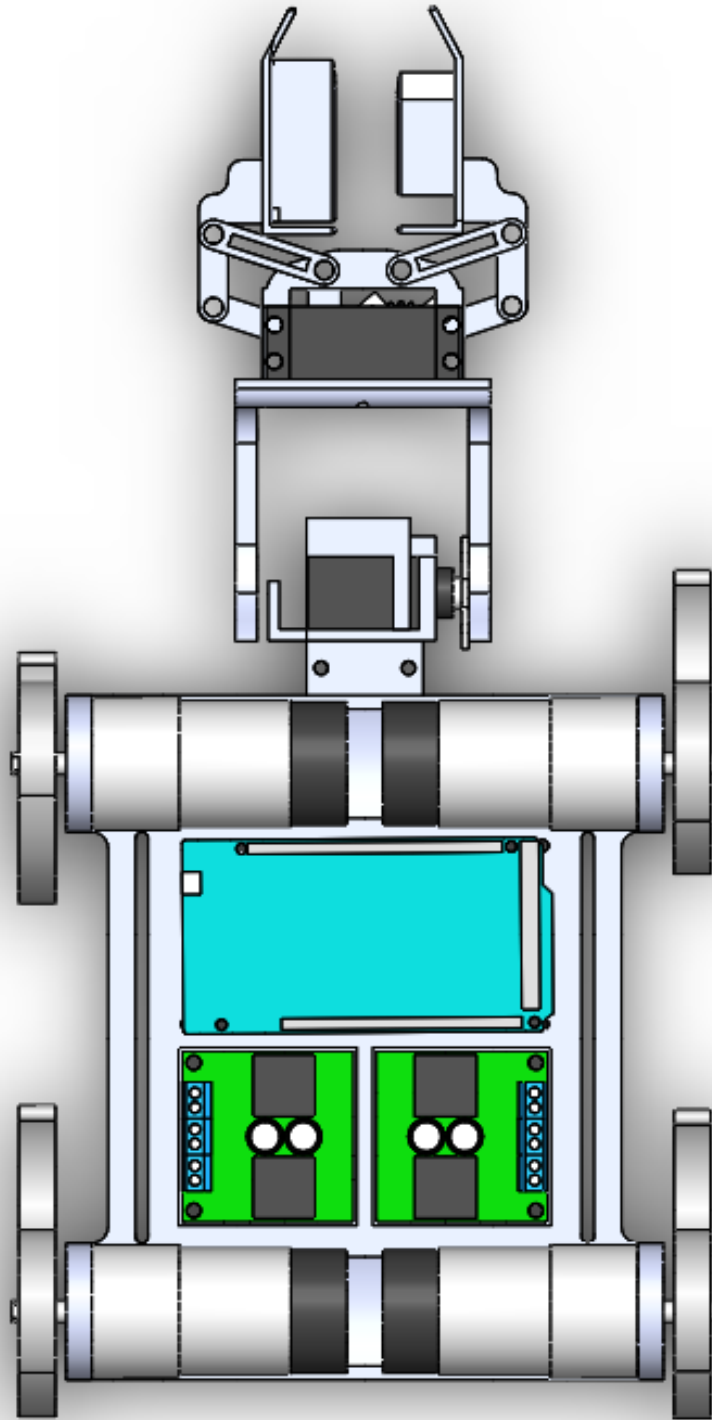


Figure 6.7: Top-down view of new robotic ant platform with C-shaped legs

## **Part II**

### **Smart Particles — *Smarticles***

## CHAPTER 7

### SMARTICLE SYSTEM OVERVIEW

Previous studies using the smarticle platform, conducted by Will Savoie, investigated ensembles in confined environments in the context of entanglement and granular matter physics. Ensembles which were confined within a ring which was free to translate were found produce a net displacement, in spite of the fact that no constituent of the ensemble was capable of displacement. This chapter outlines the system which was developed in order to better understand this particular confined ensemble.

#### **7.1 Design Parameters**

The smarticles deviate significantly from the robotic ants described in Part I in their complexity, though similar parameters were used to inform their overall design. Below are the considerations which informed the implementation of the smarticle platform.

##### 7.1.1 Safety

The smarticle platform was intended for use in numerous experimental setups, which often require frequent handling by human operators during the preparation of the trials. The smarticles are designed to be safe for human interaction at all times, with the two actuating servos characterized by low stall torques and no advantageous gearing, and with circuit elements operating well within their rated performance values.

##### 7.1.2 Form Factor

With the intent to use the smarticle to model a new type of active matter, the platform needed to be small and lightweight such that the inertia of an unbounded smarticle could be overcome by the actuation of a neighboring smarticle. The smarticles were designed to

be small, while also having servos strong enough to effectively actuate in a collision-prone environment. Ultimately, the size of commercially available servos dictated the size of the smarticles. The cases of the smarticles are built around the geometries of the selected servos, discussed further in Chapter 9.

### 7.1.3 Autonomy and Control

The principal interest incited by the smarticle platform relates to the dynamics of active matter ensembles with heterogeneous behaviors. To elicit these dynamics, the smarticles were designed around a small onboard microcontroller with exteroceptive and interoceptive sensors which govern the movement of each individual smarticle agent through its own local finite state machine.

Much like the robotic ants, the smarticles required sensory capabilities which could be used to distinguish environmental characteristics, such as the presence of light or certain frequencies of sounds, and modulate the behavior state of the smarticle accordingly. The smarticles do not have any communication capabilities, such that each robot may only respond to the locally observed environmental conditions. The smarticle and environment were designed within the context of one another, such that the environment could be manipulated in various ways to impose certain asymmetries into the ensemble; descriptions of these setups are outlined in Chapter 11.

### 7.1.4 Robustness

The confined active matter systems the smarticles were used to study ensembles which experience frequent agent collisions. The smarticles were designed to operate on a planar surface parallel to the plane in which the smarticle servos actuated. To isolate the electronics from this collision prone region, all electronics were protected either within the smarticle case or on top of the smarticle in a region which could not be affected by neighboring smarticles.

### 7.1.5 Durability

The smarticle ensemble trials could last between 60 seconds to 10 minutes, with hundreds of trials conducted for some experimental setups. As a result, robot durability was a concern in the design of the mechanical and electrical components. Mechanical clasps were used to keep the shells of the smarticles closed, with joint supports preventing the clasps from being open easily over the period of an experimental trial. In addition, all electrical components were chosen with specifications well within the expected operating conditions of the tested smarticle systems.

### 7.1.6 Scalability

The study of these active matter ensembles requires numerous smarticles be built in order for the system to operate. Collections of four and five robots were examined, which meant that elements related to the issue of scalability – such as process repeatability and component consistency – were important to ensure a uniform ensemble of hardware remained available.

The smarticle platform is composed of an Arduino Pro Mini, a single electronics perf-board populated with all relevant sensors, and two servo motors each attached to a single 3D printed servo arm all contained within two 3D printed panels which encase the entire smarticle package.

The labor associated with manufacturing a smarticle needed to be low in order to account for the large number of robots needed to test the system. The electronics are all contained on a single board which can be assembled rather quickly. When constructing the smarticle electronics using a soldering iron to trace circuits on a perfboard, several smarticles can be produced in a single day from scratch; the recent purchase of a PCB mill by the lab will reduce this production time significantly. This automated manufacturing process compliments the 3D printing capabilities of CRABLab, which will reduce the manual labor incurred to produce the smarticles by a considerable margin.

### 7.1.7 Maintainability and Availability

The stochastic nature of the smarticle ensembles required a large number of trials to be performed, which in turn required an emphasis in the design on maintainability and availability such that the smarticles were regularly available for the numerous trials which needed to be completed.

Components of the robots were modular, with the mechanical components easily swapped in a matter of several minutes and restocked in several hours using a 3D printer, and while the electronics of the smarticles rarely failed, they were cheap and readily obtained from nearby hardware stores. Sensors such as the microphone and photoresistors were kept in stock, and were readily available through Sparkfun or Digikey.

## **7.2 Smarticle Ensemble**

The collections of smarticles were forced to continuously interact by confining the system within a loose ring, as seen in Figure 7.1. These systems of smarticles and the confining ring are referred to as a *supersmarticle*. The ring was designed with slots on the side, which permitted a light source to be directed toward the smarticles and penetrate through the ring unobstructed. While the light exposure was not inhibited by the presence of the ring, and could be sensed by the nearby smarticle photosensors, the bodies of the smarticles could occlude the light and cast shadows onto the smarticles which were located behind the smarticles nearest the light. This occlusion could effectively produce a gradient of light across the smarticle ensemble. While no individual smarticle is capable of explicit communication, there is a kind of state-modifying communication present in the system in which the smarticles which occlude the light receive data in one state and confer another state to the neighboring smarticles.

Two confining rings were designed, one for containing a system of five smarticles and another for containing a system of four smarticles. The large ring for the five smarticle

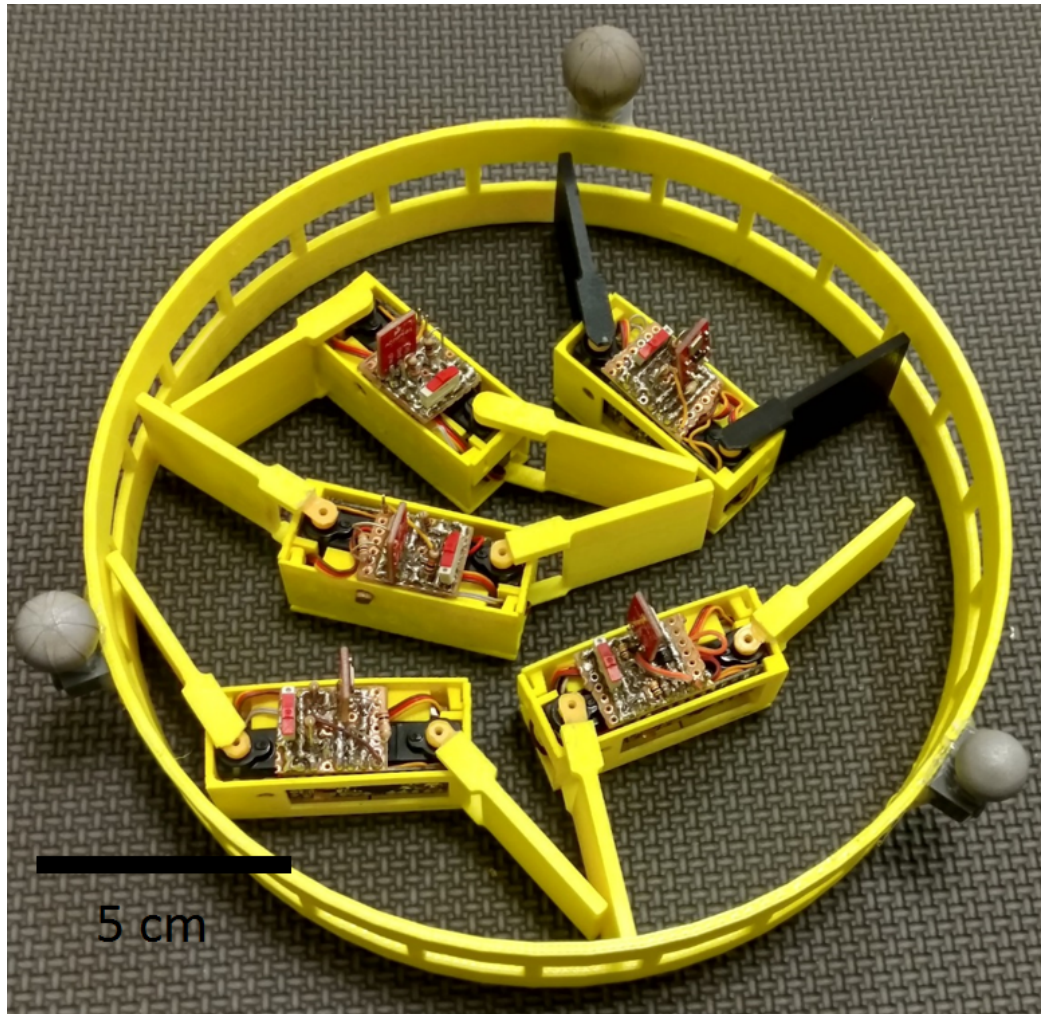


Figure 7.1: Five smarticle ring

systems was the result of several iterations of ring tests to determine which geometry resulted in the most pronounced drift dynamics. Systems in which one of the smarticles was inactivated were of particular interest, though the resulting dynamics could be attributed to the reduction in the number of smarticles moving in the system as opposed to the presence of an inactive smarticle. To study the effects of the inactive smarticle in a five smarticle ensemble on the system dynamics in comparison to a four smarticle system with no inactive smarticles, a smaller ring was designed, seen in Figure 7.2, with the radius of the ring modified such that the density of the robots per area of the ring was equivalent to the original five smarticle system.

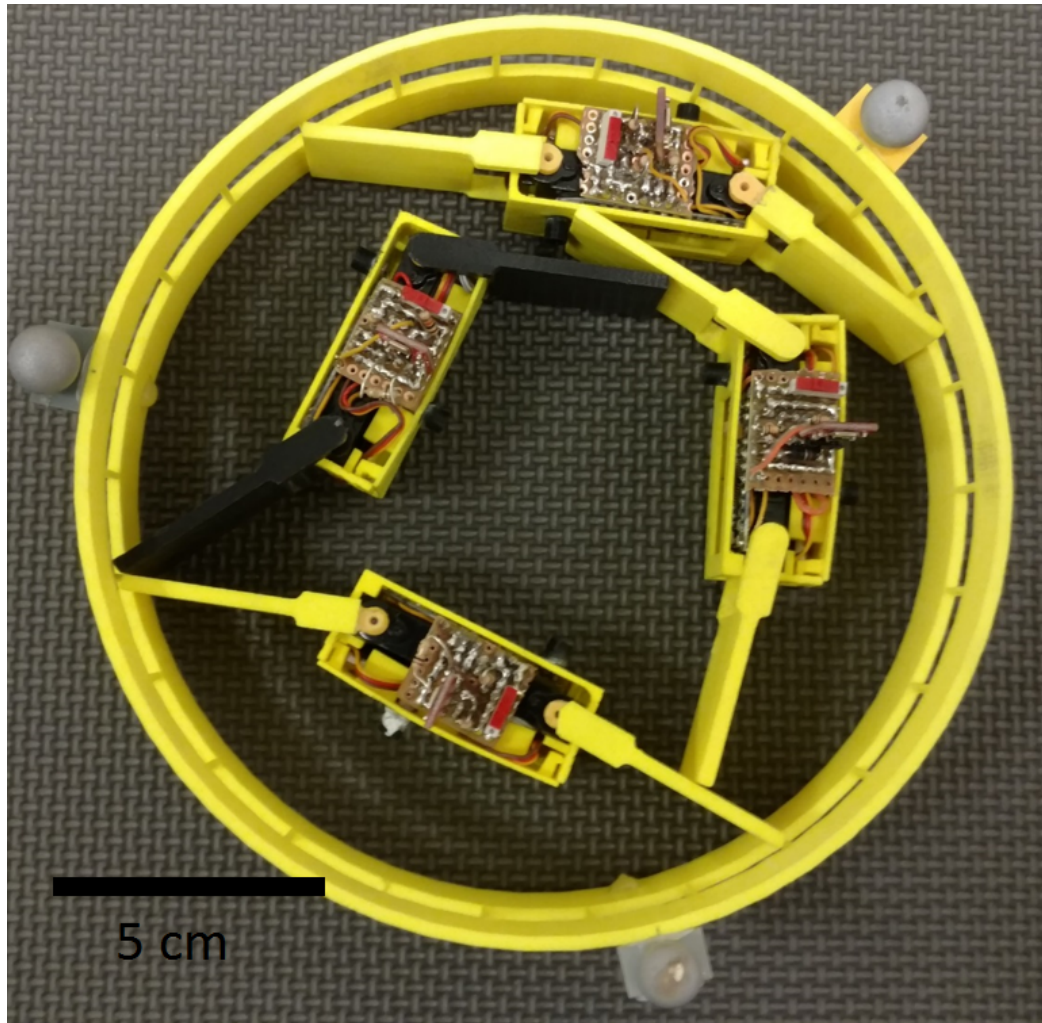


Figure 7.2: Four smarticle ring

### 7.3 Test Bed Design

The smarticle ensembles were studied on a flat, square surface with each edge measuring 0.4 m. After performing preliminary studies, the supersmarticle systems were found to be highly sensitive to small tilts in the platform which could disrupt and bias the dynamics of the system, even at angles as small as  $0.2^\circ$ . In order to produce a level platform, a kinematic mount was implemented which provides a mechanism for easily tuning the platform to be as level as possible.

The kinematic mount is a mechanical system which restricts the number of degrees of freedom by using three unique mounting blocks in which the legs of the platform sit. Each leg is composed of a threaded screw, 7.3(d), which seat in mounting blocks of varying geometries to restrict the degrees of freedom in the system. Each of the blocks constrains certain translational ( $X, Y, Z$ ) or rotational ( $R_x, R_y, R_z$ ) degrees of freedom. The first of these blocks is a cone, which constrains the translational degrees of freedom along all axes ( $X, Y, Z$ ) of the system. An image of the cone mounting block can be seen in Figure 7.3(a).

The next block considered has a groove slot, Figure 7.3(b), which when oriented along one axis will restrict the rotational degrees of freedom of the orthogonal axes. For example, a grooved block aligned along  $X$  will constrain the rotational  $R_y$  and  $R_z$  degrees of freedom.

Given the above examples of the cone and groove blocks, five of the six degrees of freedom have been eliminated. A simple flat block, Figure 7.3(c), can be used to restrict the final degree of freedom,  $R_x$ . Two flat blocks were implemented on the kinematic mount in order to reduce the loads acting on the threads of the screws which supported the leveled platform.

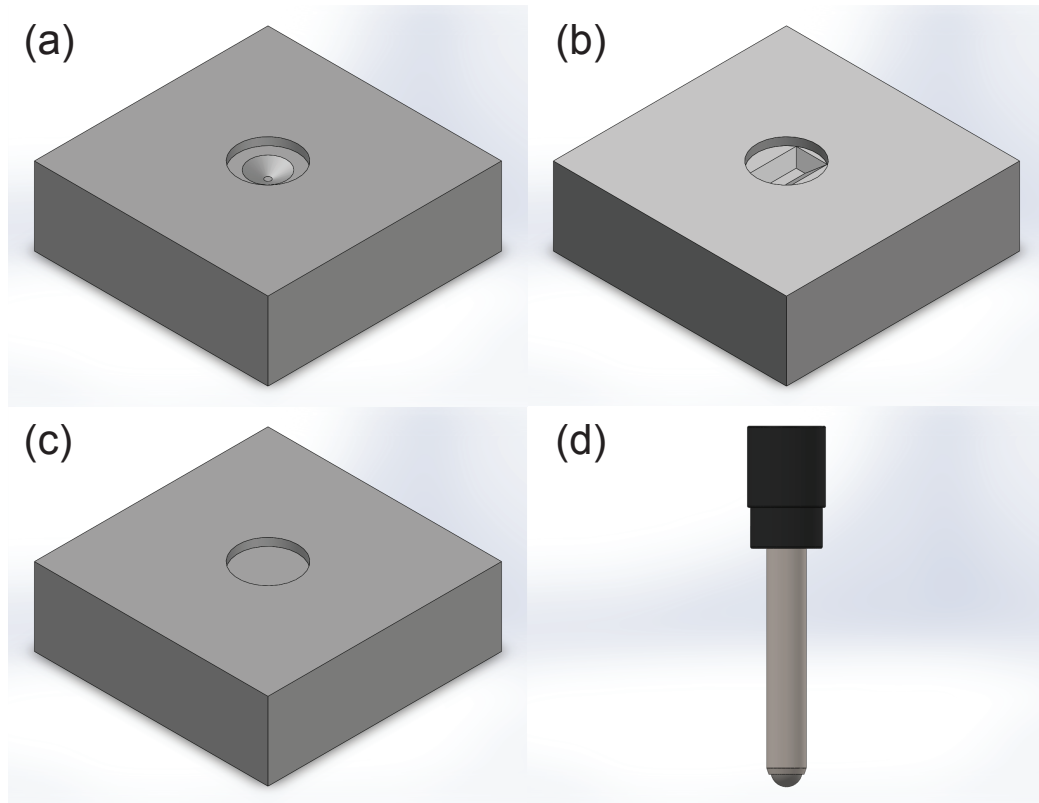


Figure 7.3: Isometric views of the cone (a), groove (b), and flat (c) mounting blocks for the kinematic mount. The adjustment screw (d) is constructed with a ball tip which interfaces with the artifacts of the various mounts. The adjustment screw has 80 threads per inch, such that the plate can be leveled with a high degree of precision.

## **CHAPTER 8**

### **SMARTICLE ELECTRICAL DESIGN**

Modifications were made to the previous smarticle platform, developed by Will Savoie, which included the addition of two photoresistors and the supporting circuitry, which ultimately necessitated a redesign of the electronic organization of the platform. All aspects of the smarticle electronics, ranging from sensor implementation to servo control, are outlined in this chapter.

#### **8.1 Microcontroller**

Previous iterations of smarticles featured surface-mount devices such as microcontroller ICs implemented on etched printed circuit boards. However, the methods available for these implementations were inconsistent and did not support scaling for the number of desired robots which needed to be produced. The current iteration of smarticles utilize an Arduino Pro Mini 328-3.3V/8MHz, which is used to implement the finite state machine, handle the analog-to-digital conversion (ADC), and manage servo control.

The Arduino Pro Mini has 14 digital I/O pins. Six of the pins are capable of PWM used for controlling servo motors; six analog input pins are used for sensing the current draw of the servo motors, the signal from the microphone, and the voltages across the photoresistors (which are correlated to the light exposure on the smarticle).

#### **8.2 Sensors**

The smarticles were implemented with several behavioral states which depended on various environmental cues of the system setup, such as the congestion of the local environment inferred by measuring the stress on the servo arms, tone frequencies being played in the

test room measured by an onboard microphone, and light levels measured by a pair of photoresistors on opposing faces of the smarticle case.

### 8.2.1 Interoceptive Sensors

#### *Stress Sensing*

The servo arms of the smarticles are often unable to actuate in their full joint space due to the confined environments in which they operate. As a result, the servos of the smarticles are often stalled, which can reduce the lifetime of the servo. A shunt resistor, sometimes called an ammeter shunt, allows the smarticle to measure the electrical current drawn by the servos. A current shunt resistor is a low resistance ( $1\Omega$ ) circuit element placed in series with the two servo motors of the smarticle. The voltage across the shunt resistor can be measured using one of the analog pins of the Arduino Pro Mini, and the current draw of the servos can be computed using a simple algebraic rearrangement of Ohm's law:  $I_{servos} = V_{shunt}/R_{shunt}$ . The state of the servos can be inferred based on the current draw, and the code on the smarticle microcontrollers can allow the servos to effectively sense when they are stalled and modify the joint angles while still adhering to the principle active matter behaviors to study the active matter system without damaging the servos.

### 8.2.2 Exteroceptive Sensors

#### *Tone Sensing*

The first method used to control systems of smarticles implemented tone generators to produce heterogeneous behaviors in the ensembles. Certain smarticles were programmed to exhibit a unique behavior in response to a particular tone, with each smarticle having a unique tone-behavior profile. These tones were sensed using an ADMP401 MEMS microphone supplied by Sparkfun, which is connected to an analog pin of the Arduino Pro Mini for ADC. A Fast Fourier Transform (FFT) of the signal produced by the microphone

is performed on the Arduino Pro Mini, with the behavior within the finite state machine being governed by the dominant signal of the FFT.

### *Light Sensing*

A single photoresistor was placed on each of the dominant faces of the smarticle, as seen in Figures 9.12 and 9.13. A voltage divider was implemented for each photoresistor, with the voltage across the resistor monitored using an analog pin of the Arduino Pro Mini, such that the smarticle could sense light exposure on both sides of the center link. The voltage divider associated with the photoresistor was designed to allow the values read across the photoresistor to express the full range of light levels the photoresistors are sensitive to.

### 8.2.3 Sensor Summary

The smarticle platform was constructed with a number of sensors, outlined in Table 8.1, which allow the robot to perceive multiple environmental states, as well as internal states.

Table 8.1: Summary of Smarticle Sensors

<b>Sensor</b>	<b>Function</b>
Current Shunt Resistor	Servo Stress
Microphone	Tone identification
Photoresistors	Light levels

### **8.3 Actuators**

Each smarticle has two servo motors located on the lateral sides of the center link. As mentioned previously, one of the design parameters was to keep the smarticles as small as possible, which was ultimately restricted by the size of commercially available servo motors.

### 8.3.1 Servo Motors

The servo motors for the side link actuation are Power HD-1440A Microservos. These servos feature a standard three pin connection through 32 gauge wires for the positive power terminal, ground, and servo control signal line which carries a PWM signal from a designated digital PWM pin on the Arduino Pro Mini. The servos have a stall torque of 0.6 kg·cm and a stall current of 270 mA at 4.8V, though the smarticles are powered using a 3.7 LiPo battery. At a full charge, the LiPo battery can be expected to have a voltage in the range of 4.1V-4.2V, such that a stall torque as high as 0.6 kg·cm will never be realized.

The servos have the ability to actuate through a 165° range between -82.5° and 82.5°. These ranges of values are controlled by the duty cycle, or pulse width, of the square wave provided by the digital pin of the Arduino Pro Mini. For the smarticle servos, pulse widths of 800  $\mu s$  will cause the servo to actuate to the maximum counterclockwise position, 2200  $\mu s$  to the maximum clockwise position, and 1500  $\mu s$  to the position parallel with the center link of the smarticle.

A joint angle space can be described which represents the angles of the servo arms with respect to a given position of the servo about the axis of revolution. An example of this can be seen Figure 8.1(a), in which the parameter  $\alpha_1$  represents the deviation of the left smarticle link from plane of the center link of the smarticle, and  $\alpha_2$  represents the deviation of the right smarticle link from plane of the center link of the smarticle. Each link parameter,  $\alpha_1$  and  $\alpha_2$ , represent a dimension in which the smarticle can modulate its shape, such that a two-dimensional plane of  $\alpha_1 - \alpha_2$  can express all possible configurations of the smarticle. Given that the servos are restricted to an approximate 180° arc, each  $\alpha_i$  is restricted to be between  $-\pi/2$  and  $\pi/2$ .

This joint description in  $\alpha_1 - \alpha_2$  can capture all configurations of a smarticle. Furthermore, a gait can now be described by considering an orbit within the  $\alpha_1 - \alpha_2$  plane. Given a starting position, a path can be path traced in  $\alpha_1 - \alpha_2$ , such as the red square given in Figure 8.1(b), which in turn describes the positions of the servos as the smarticle actuates

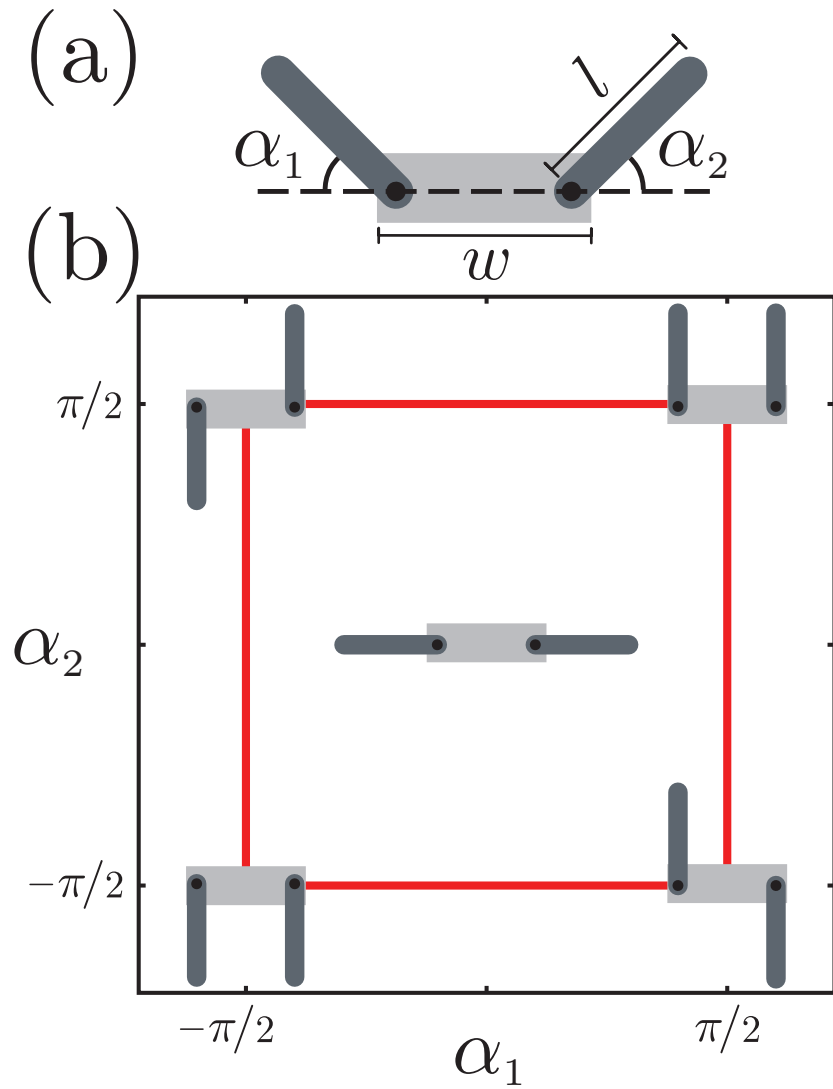


Figure 8.1: Square gait joint space trajectory traced by smarticle

over a period of time. If the end point of the trace is coincident with the start point, then cycles of the gait can be performed continuously. The gait presented in Figure 8.1(b) is the exact gait expressed by smarticles in the *active* state. The *inactive* state is defined by the smarticle located at  $\alpha_1 = 0, \alpha_2 = 0$ , seen in the center of Figure 8.1(b).

## 8.4 Circuitry

The electrical components of the smarticle are all mounted on a single board which sits on top of the smarticle center link between the two servo horns which connect to the lateral links, seen in Figure 8.3. An overview of the board is given below.

### 8.4.1 Main Board

The Main Board of the smarticle is connected to the Arduino Pro Mini using a set of 90° pin headers, which provides a durable connection while also enforcing a geometry that allows that electrical components of the smarticle to fit neatly into the compact cases.

The board receives power from the 3.7V LiPo battery which is connected through a SPST switch that can be easily accessed in case a smarticle needs to be turned off quickly. The battery voltage is connected to both the RAW pin of the Arduino Pro Mini, which powers the microcontroller, and the pair of servos in the smarticle body. The rest of the board is provided power through the 3.3V pin of the Arduino Pro Mini, which connects to the ADMP401, shunt resistor, and photoresistors. These sensors signals are all connected to analog pins of the Arduino Pro Mini.

### 8.4.2 Battery Selection

The Arduino Pro Mini selected for use in the smarticles operates at 3.3V, similar to the Arduino Due, with all I/O pins rated for a maximum voltage of 3.3V. However, the Arduino Pro Mini power supply, connected through the RAW pin of the board, requires an input between 3.35V and 12V. The large range of possible values afforded some flexibility in terms of battery selection. However, restrictions in terms of maintaining a tight form factor for the smarticle package led to the selection of a small 3.7V LiPo battery for use in small remote controlled aircraft. At full charge, the battery will have a voltage of approximately 4.2V, which is well within the operating range for the Arduino Pro Mini while also

providing a more advantageous driving voltage for the servos.

## **8.5 Electrical Design Conclusion**

The electronics of the smarticles were designed to allow the robotic platform to sense various environmental variables while also possessing sufficient processing capabilities to intelligently analyze the sensory signals and actuate in response. The electronics were designed not only with safety and robustness in mind, but also form factor, such that the smarticle is compact and the forces produced by the servos are sufficiently large relative to the masses of the smarticle.

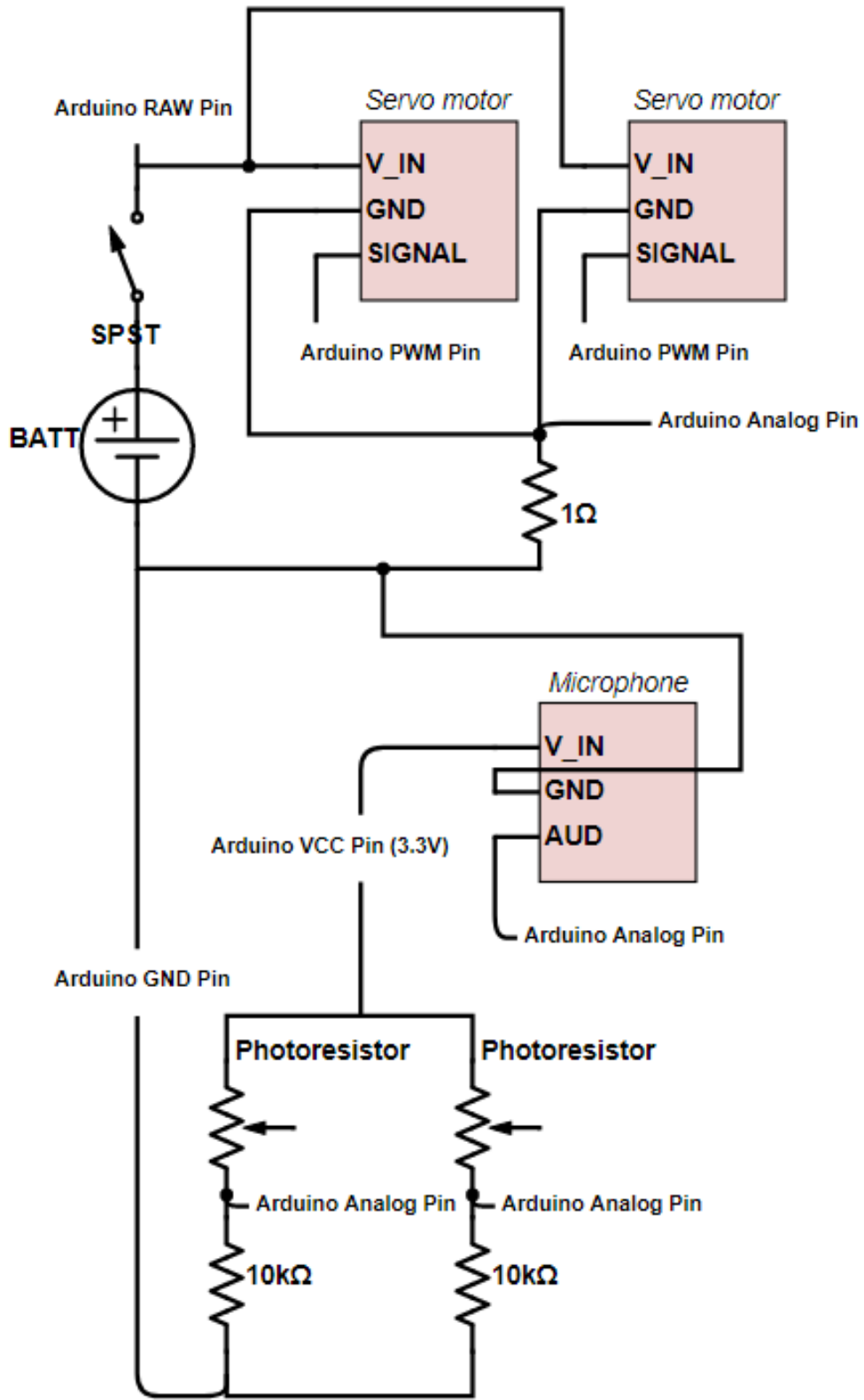


Figure 8.2: Smarticle electronics schematic

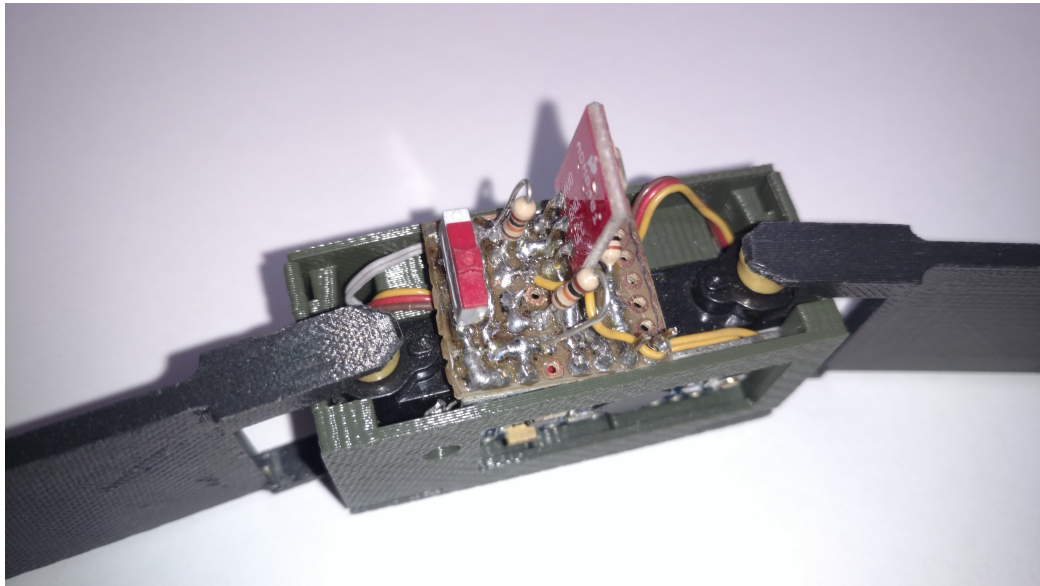


Figure 8.3: Top-down view of the smarticle assembled electronics board

## CHAPTER 9

### SMARTICLE MECHANICAL DESIGN

Two types of smarticle cases were developed: *flat* cases and *light pipe* cases. The flat cases were developed for use in a system which used a directed point-source light to illuminate the environment along a radial direction. Smarticles in the environment could sense the presence of light, or lack thereof, and behave according to the perceived level of illumination. The second case included an extra geometric entity which protruded from the face of the smarticle, and was designed for use in systems with an undirected light bar illuminating the environment along a single axis.

#### 9.1 Design Approach

The smarticle platform was designed in a similar manner to the robotic ant. Manufacturing methods such as 3D printing were leveraged heavily in order to iterate on designs quickly, and replacement parts with complex geometries could be produced with ease in several hours. Unlike the robot ant platform, which uses hardware such as nuts and bolts to affix parts to one another, all mechanical components of the smarticle are connected by geometric constraints of the 3D printed parts.

##### 9.1.1 Smarticle Case Design

The smarticle body is an assembly of two halves of the case. The front case of the smarticle, seen in Figure 9.5a is designed with a cutout section which accommodates and protects the protruding circuit electronics of the Arduino Pro Mini from contact with other smarticles while also allowing the Arduino Pro Mini to be programmed using the exposed FTDI pad connections. The front case also has a small hole to hold the forward-facing photoresistor in place. Slots are cut near the bottom of the front case of the smarticle case to allow for

the inset servo arms to actuate through the full range of joint angles. The lateral arms of the front case are reinforced at the junction with the front face to prevent fracturing during assembly. The lateral arms have tabs which hold the servo motors in place, and include a snap groove on either arm which fits into the hook groove located on the back case. The bottom of the front case has two holes which align with the servo motor actuators to keep the servo arms of the smarticle on a constant axis throughout the entire joint motion. In addition, several small medial platforms were added to enforce the internal geometries of the components and support various components such as the Arduino Pro Mini, the servos, and the battery pack.

The flat smarticle case was used in test environments with a directed light source which could be accurately manipulated to point towards an exposed photoresistor within the smarticle ensemble. Manual control was necessary because unobstructed light acting on the photoresistors would saturate the signal even at relatively low angles of incidence. To investigate the effect of the angle of incidence on the signal values read by the Arduino Pro Mini, a test was conducted in which the cases of the smarticles were rotated through a range of angles between  $0^\circ$  and  $90^\circ$ , with analog readings from the Arduino Pro Mini recorded every  $10^\circ$ . A diagram for the test setup can be seen in Figure 9.1, with the results for the flat smarticle case seen in Figure 9.2.

In order to develop a platform which could be controlled without any external manual inputs, various methods were investigated which would effectively restrict the angle of acceptance of the photoresistors, producing a drop-off in analog signal in the angular incidence range of  $30^\circ$ – $50^\circ$ . Lenses were tested first, which were attractive for their relatively low profile. However, fixing the lenses to the case was unreliable given the frequent collisions the cases experience, and the lenses were found to be inconsistent from smarticle to smarticle. Instead, a light pipe geometry was used which could be tuned by modifying the length of the pipe as well as the inner diameter of the collector. At low angles of incidence, the light enters the collector and reaches the photoresistor unobstructed, though at higher

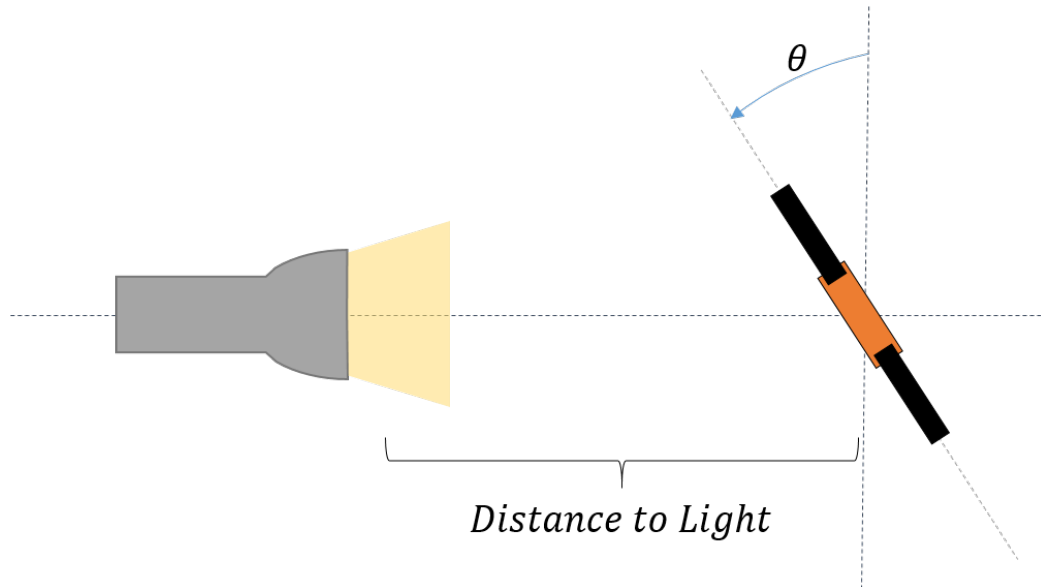


Figure 9.1: Angle of incidence test setup

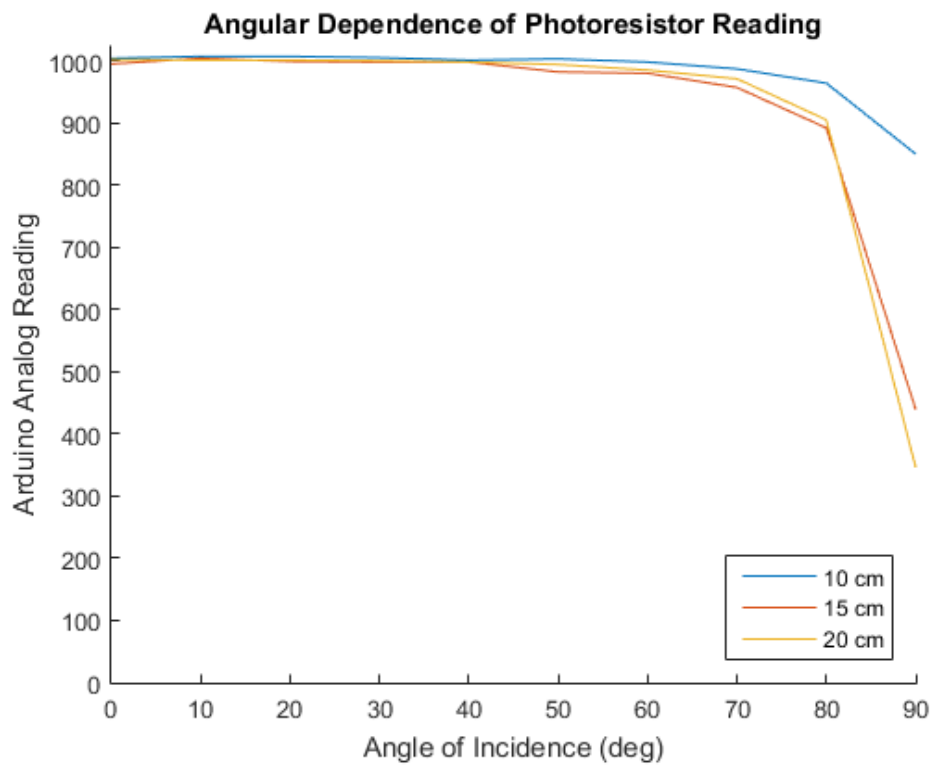


Figure 9.2: Light sensor readings as a function of angle of incidence at varying distances from the light source

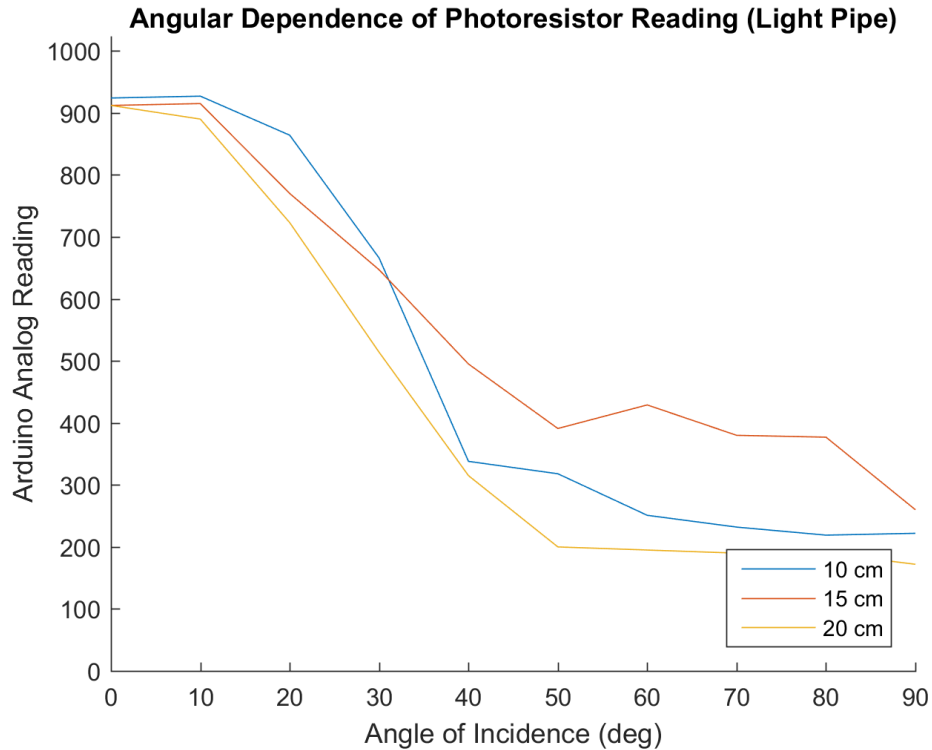


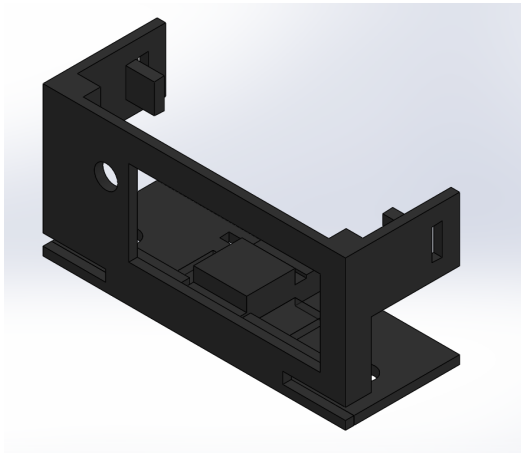
Figure 9.3: Light sensor readings for the new smarticle case as a function of angle of incidence at varying distances from the light source

angles of incidence the geometry of the light pipe occludes the sensor, and a significant and consistent drop-off in the photoresistor signal can be observed, as seen in Figure 9.3.

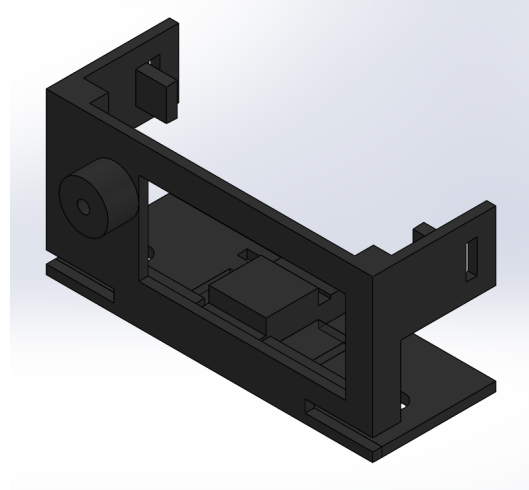
The light pipe case is identical to the flat case, with an additional cylindrical element 20 mm in diameter and 50 mm in height protruding from the face of the cases. Comparisons of the two types of cases can be seen in Figures 9.4-9.6.

The back case of the smarticle was designed with snap hooks which clasp with the snap grooves of the front case to keep the two halves of the smarticle together. The back panel has an identical hole and optional light pipe geometry as the front case, with protruding tabs which are used to confine the position of the servo motors and LiPo battery.

The two halves of the smarticle case enclose a volume which contains the Arduino Pro Mini, the battery, and both servos. The two lateral links of the smarticle are connected to the smarticles using a servo horn provided with the HD-1440A servos which fits into a

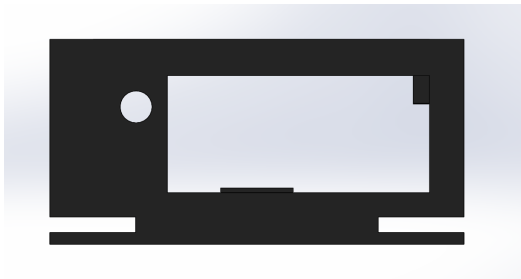


(a) Flat Smarticle



(b) Light Pipe Smarticle

Figure 9.4: Isometric view comparison of two smarticle cases

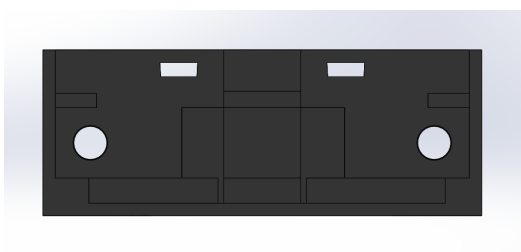


(a) Flat Smarticle

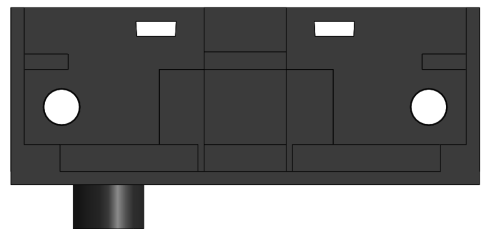


(b) Light Pipe Smarticle

Figure 9.5: Front view comparison of two smarticle cases



(a) Flat Smarticle

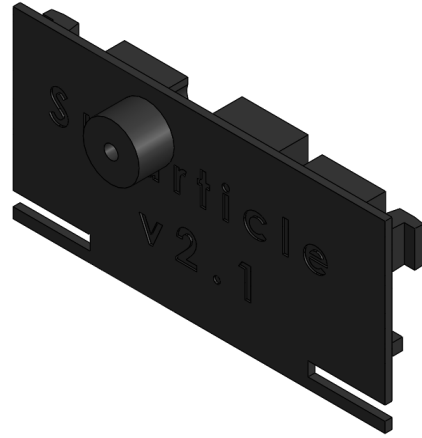


(b) Light Pipe Smarticle

Figure 9.6: Top view comparison of two smarticle cases

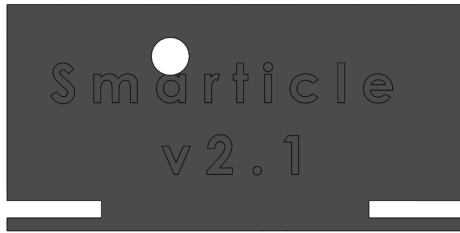


(a) Flat Smarticle



(b) Light Pipe Smarticle

Figure 9.7: Isometric view comparison of two smarticle cases



(a) Flat Smarticle

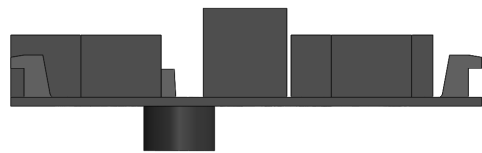


(b) Light Pipe Smarticle

Figure 9.8: Front view comparison of two smarticle cases



(a) Flat Smarticle



(b) Light Pipe Smarticle

Figure 9.9: Top view comparison of two smarticle cases

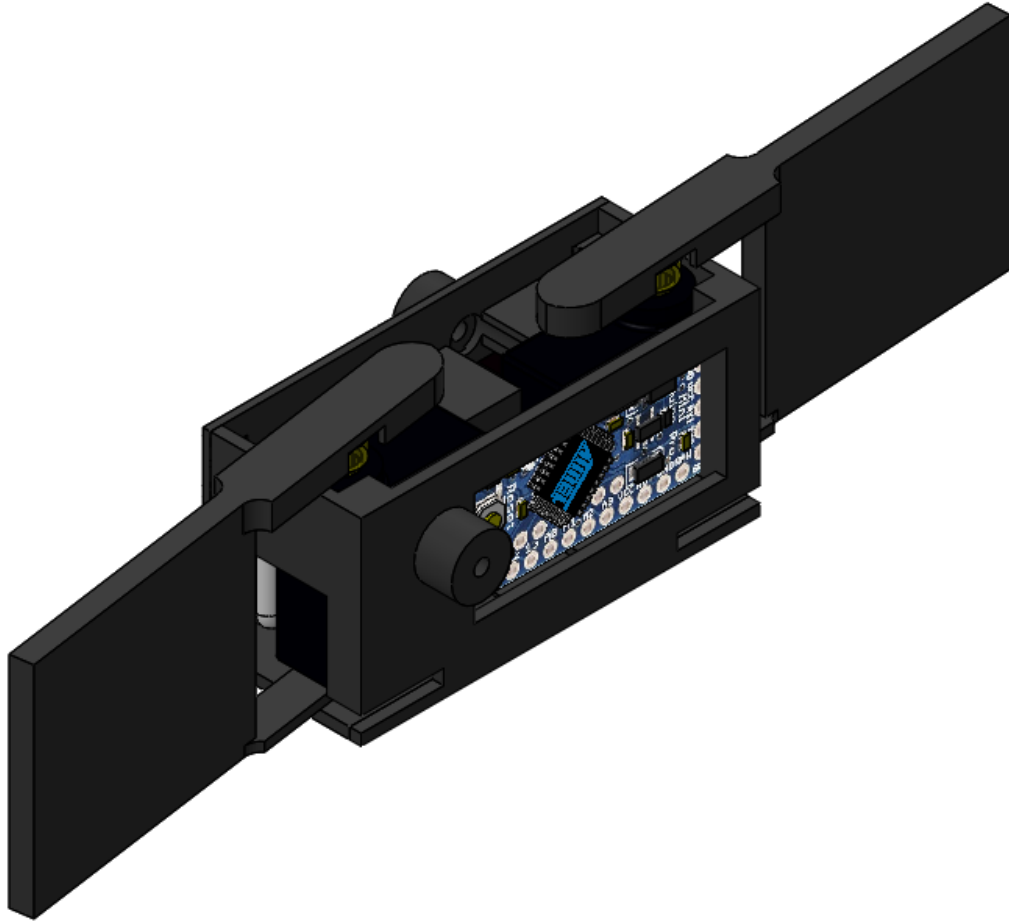


Figure 9.10: CAD model of assembled light pipe smarticle, isometric view

cavity located on the upper tab of the servo arm. The lower tab of the lateral link has a tapered cylinder which fits into the hole located on the bottom of the front case, enforcing an axis of rotation which is parallel to the vertical dimension of the smarticle. An exploded view of the CAD assembly can be seen in Figure 9.11.

## 9.2 Assembled Smarticles

Figures of the assembled flat case case smarticles are provided in Figures 9.12 and 9.13.

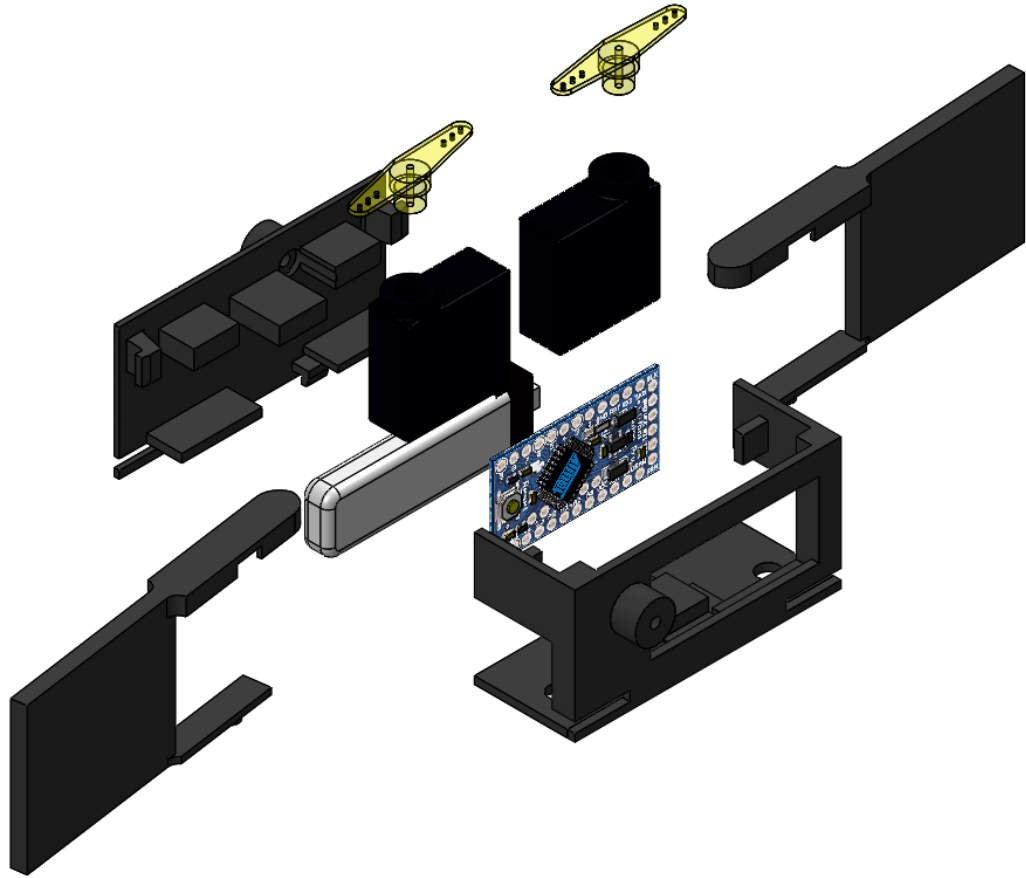


Figure 9.11: Exploded assembly of light pipe smarticle



Figure 9.12: Assembled flat smarticle front view



Figure 9.13: Assembled flat smarticle back view

## CHAPTER 10

### SMARTICLE SOFTWARE DESIGN

The software implementation on the smarticle microcontrollers are detailed below, with attention given to the design of the finite state machines which govern the behavior of the smarticle.

#### 10.1 Design Approach

The embedded software on the Arduino Pro Mini utilizes a finite state machine architecture to control the various smarticle behaviors in response to sound and light. The code was designed to be modular with reuse in mind, such that various sensors can be polled using hardware specific code that in turn enact common smarticle behaviors.

#### 10.2 Arduino Pro Mini Code

The code implemented on the Arduino Pro Mini was developed in Notepad++ and compiled using the Arduino 1.8.3 IDE. The standard Arduino architecture discussed in Section 5.1 applies here, where the code first executes `setup()`, followed by repeated executions of `loop()`.

The smarticle has two behaviors: active and inactive. Upon each execution of `loop()`, the behavior-informing sensors, either the light sensors or the microphone, are polled. The values returned from the sensor are used to determine if the active state or the inactive state will be entered. If the active state is entered, then the smarticle will actuate the servos and move about the periodic square gait trajectory, i.e. trace the red line of Figure 8.1, a single time. The period of this movement was experimentally determined to be 1.7 seconds. If the smarticle sensory inputs indicate that the inactive behavior should be expressed, then

the smarticle moves the joints such that the arms are parallel to the center link of the robot, and holds this configuration for 1.7 seconds, such that both periods are expressed for equal periods of time per execution. Upon completion of the active or inactive behavior, `loop()` would terminate and immediately be called again.

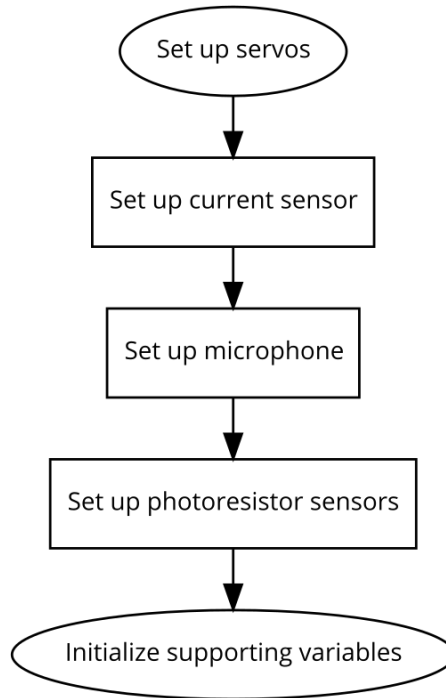


Figure 10.1: Overview of `smarticle setup()`

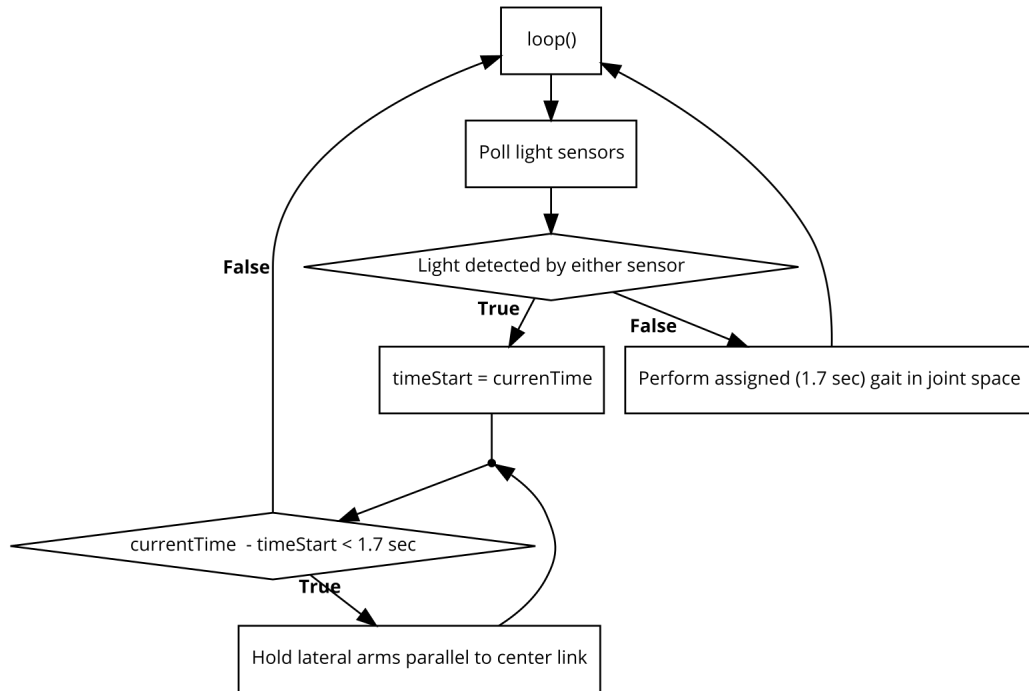


Figure 10.2: Overview of smarticle light-controlled `loop()`

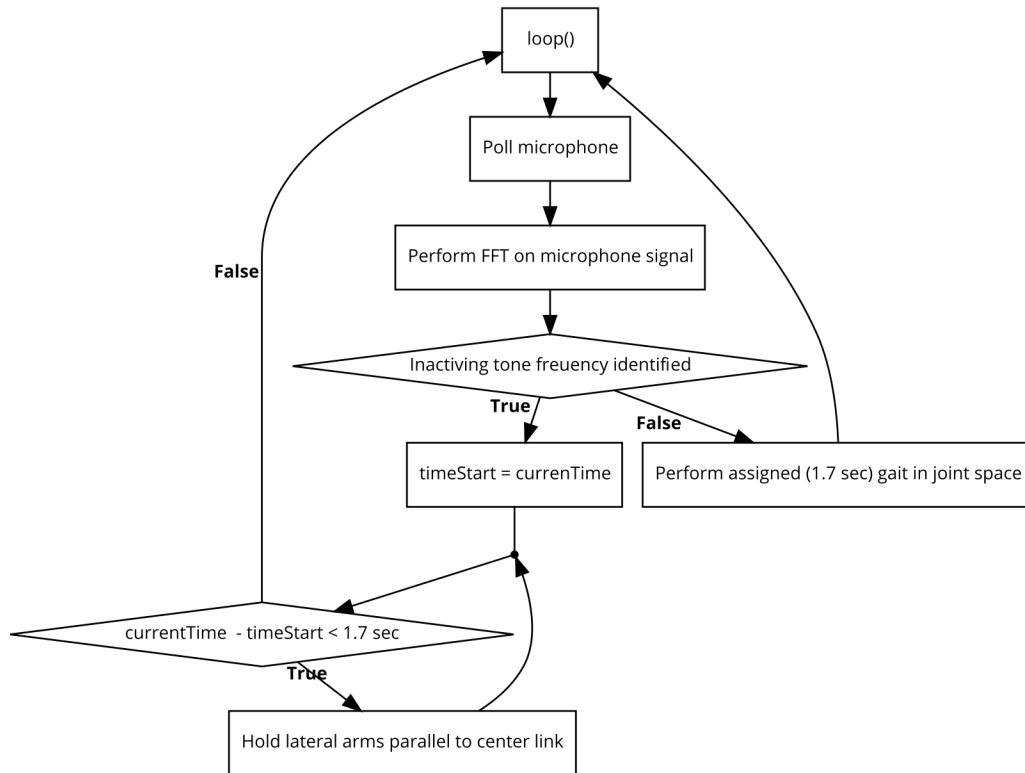


Figure 10.3: Overview of smarticle sound-controlled `loop()`

### 10.3 OptiTrack

An infrared tracking system produced by OptiTrack was used in conjunction with a software called Motive in order to track various markers placed on elements of the supersmarticle system over the period of the trials. The data recorded were then imported into MATLAB for further processing.

### 10.4 msdalyzer

The MATLAB class `msdalyzer`, developed to support mean square displacement (MSD) analysis, was used to analyze the trajectory data [38]. MSD analysis is often used in colloidal studies to determine the modes of displacement dynamics which govern suspensions of particles, which was useful in enumerating the sort of diffusion dynamics exhibited by

the supersmarticle systems.

## CHAPTER 11

### SMARTICLE RESEARCH METHODS

For each experiment a supersmarticle, i.e. the smarticles and the bounding ring, was placed on a level plane, described in Section 7.3. The smarticles were all programmed to exhibit two distinct behaviors: active and inactive. In the active state, the smarticle servos trace a square drawn in the 2-dimensional joint space, as seen in Figure 8.1(b). In the inactive state, the smarticle servos were held at a fixed position such that all of the links of the smarticle were parallel.

Systems of five smarticles confined within a bounding ring were studied, utilizing control methods such as a pivoting point light source, a stationary light bar, and a speaker which emitted sounds which could target specific smarticles and inactivate them. Prior to conducting trials with the input bias, experiments were conducted without any control inputs. These uncontrolled experiments were used to determine the effect of the control inputs on the overall system dynamics. In addition, unbiased experiments were conducted with supersmarticles containing four smarticles to determine if the changes in the diffusive behavior of the system could be attributed to the presence of an inactive smarticle or to the presence of four active smarticles.

#### **11.1 Light-Based Experiments**

For the light-based control experiments, the smarticles were programmed to exhibit the active state until a light source was detected by the a photosensor, at which point the smarticle switched to the inactive state. When the light was no longer detected, the smarticle returned to the active state.

Two smarticle cases were used in the light-based smarticle experiments. Both systems were controlled with a light source located at the center of one of the perimeter edges of

the test platform. The first system studied used the flat smarticle case with the control input provided by a manually directed point light source. In order to remove the human element from the control loop, a new set of smarticle cases with light pipes were implemented, with the control input being provided by a static light bar, as seen in Figure 11.1.

#### 11.1.1 Manually Controlled System

Trials for the manually controlled system began centered in the middle of the test plane, with the point light source located at the midpoint of one of the edges of the test plane. OptiTrack markers were placed symmetrically around the ring of the supersmarticle, and the center of geometry was recorded over the entire period of the trial. Trials were allowed to run until the displacement of the supersmarticle reached the perimeter of the test plane, at which point the data collection was stopped. The displacement rates of the supersmarticle could become negligibly small in some interaction modes within the ensemble; trials which exhibited these behaviors were truncated after ten minutes of data collection. A compilation of the tracks of the supersmarticle for 16 trials is given in Figure 12.1.

#### 11.1.2 Light Pipe Controlled System

The development of the light pipes for the smarticle cases sufficiently reduced the angle of acceptance of the photosensors. The reduction of the angle of acceptance allowed the smarticle activity to be geometrically modulated by the orientation of the supersmarticle configuration, thereby removing the need for the human operator of the control input. Similar to the manually controlled systems, the center of geometry was recorded for all trials, with runs truncated after 10 minutes of displacement recording.

### **11.2 Sound-Based Experiments**

For the sound-based control experiments, certain microphone signals were programmed to cause specific smarticles to enter the inactive state. A pre-programmed inactive tone was

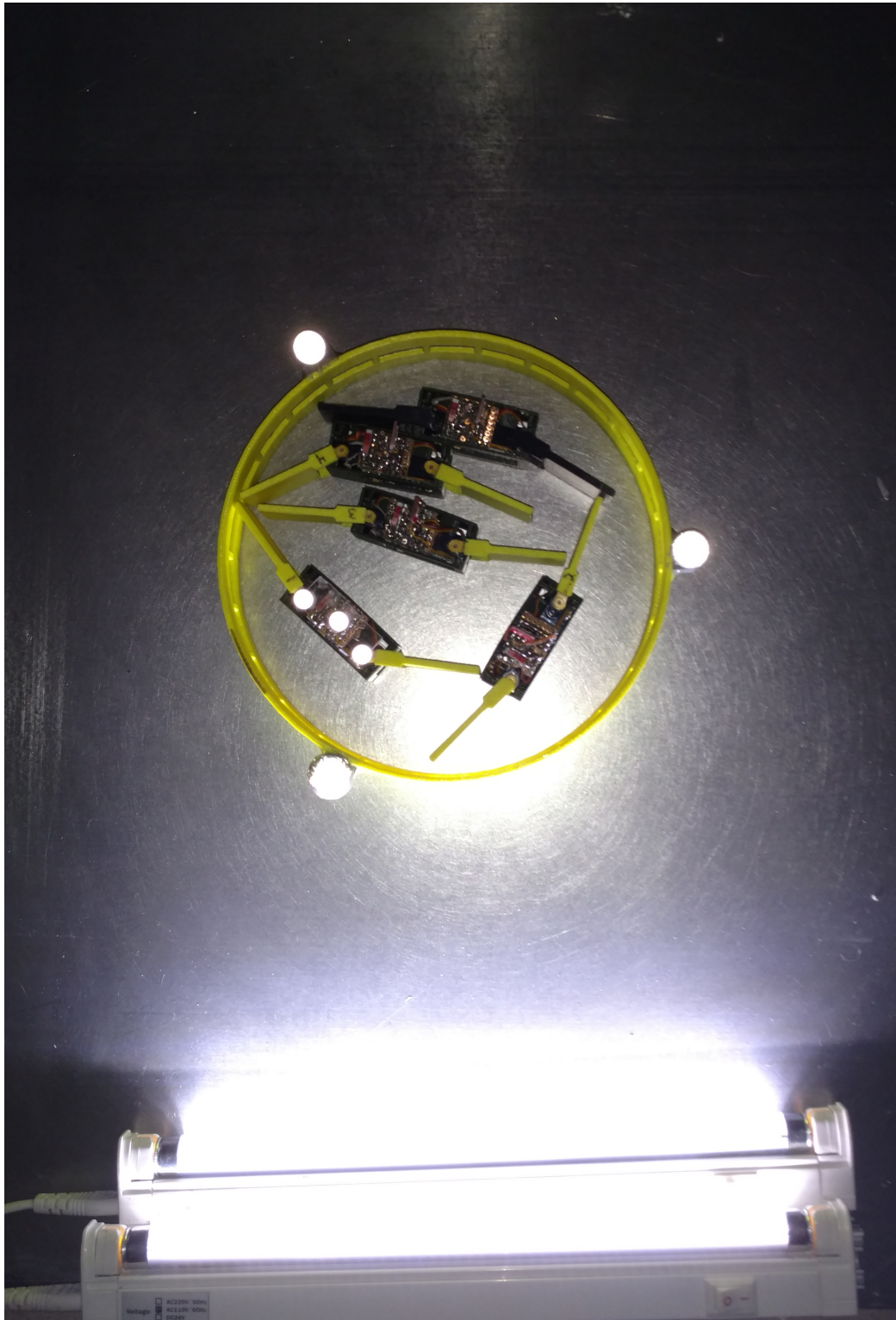


Figure 11.1: Top-down view of the test bed set up for light bar tests

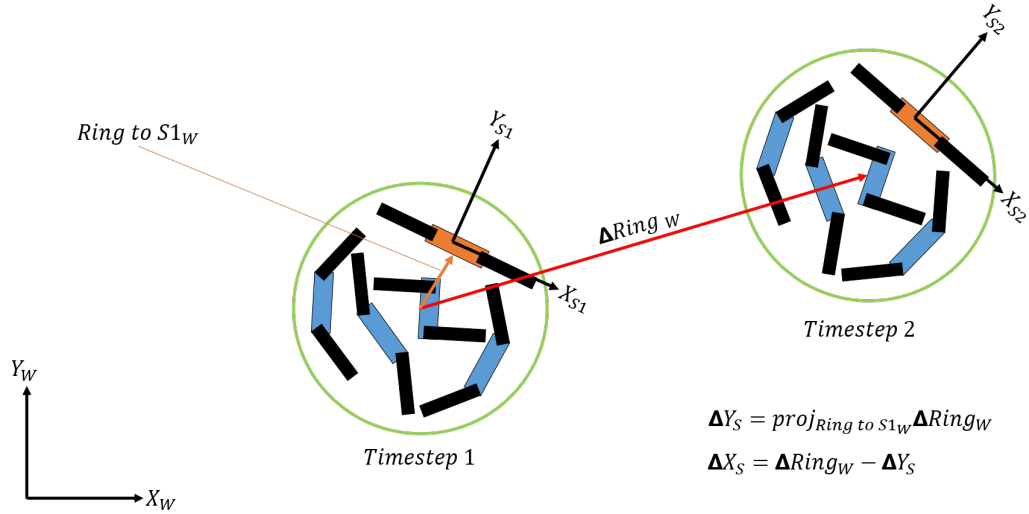


Figure 11.2: Moving from the world frame to the smarticle frame

assigned to each smarticle, such that each smarticle in the system could be inactivated by playing a unique tone while all other smarticles persisted in the active state.

The center of geometry of the rings were recorded for all trials, and for the tone-controlled systems the location of pairs of active and inactive smarticles could also be recorded. In the light controlled experiments, the position of the inactive smarticles within the ensemble were constant due to the presence of the control input being external and present on a single side of the system. In the sound-based control trials, a single smarticle was inactivated by playing a specific tone, and the smarticle was tracked over the period that the supersmarticle moved. Because the bias of the control input is not inherently biased by the geometry of the system, the inactivated smarticle is free to drift within the supersmarticle. OptiTrack markers were placed on the inactive smarticle, such that the displacement of the center of geometry of the ring could be recorded not only in the world frame of the system, but also in the frame of the inactive smarticle.

The transformation from the world frame, denoted by  $(X_W, Y_W)$  in Figure 11.2, to the inactive smarticle frame, denoted by  $(X_{S1}, Y_{S1})$ , is performed by determining the vector from the center of geometry of the ring in the world frame to the position of the inactive smarticle in the world frame. The displacement between the current time step and following

time step, denoted by  $\Delta Ring_w$ , is then decomposed into parallel and perpendicular components with respect to the vector from the center of geometry of the ring to the inactive smarticle position in the previous time step.

## CHAPTER 12

### SMARTICLE RESULTS AND DISCUSSION

Supersmarticle displacement experiments were performed using three unique control schemes. Diffusive behavior was observed in all proposed control methods, including the unbiased experiments. The presence of inactive smarticles, either in response to a light source or a sound, introduced biases in the supersmarticle diffusive behavior.

Mean squared displacement (MSD) curves have often been used to describe the types of diffusive behavior present in a dynamic ensembles of moving particles [39]. The MSD,  $\sigma^2$ , for a 2D system is defined as:

$$\sigma^2 = \langle \vec{x} \cdot \vec{x} \rangle - \langle \vec{x} \rangle \cdot \langle \vec{x} \rangle = 4Dt^\gamma$$

for  $\vec{x}$  the vector from the initial position to the current position,  $D$  the diffusion coefficient, which characterizes the rate of migration of a set of particles, and  $\gamma$  the power-law exponent for the system. Free diffusive movement is seen for values of  $\gamma = 1$ , with  $\gamma < 1$  characterizing subdiffusive behavior and  $\gamma > 1$  characterizing superdiffusive behavior, or active transport. By fitting a line to the log-log plot of the MSD curve, the slope of the resulting fit will be the diffusion exponent parameter  $\gamma$ .

The MSD curves for each set of experimental data was computed, and linear approximations were fit to the log-log plots for each trial. After completing all of the fits for all trials, the mean of the powers, MOPs, was used to quantify the average diffusive behaviors expressed by the ensemble. The MSD plots for the supersmarticle tracks presented in Figure 12.1 are presented in Figure 12.2, with the log-log scale data used for linear fitting given in Figure 12.3.

## 12.1 Flat Smarticles Controlled by Light

The manually controlled supersmarticle system consistently diffused in the direction of the light source, with an average trend in the direction of the inactivating stimuli of  $79.2 \pm 11.6\%$  across all trials. The supersmarticle tracks for all trials can be seen in Figure 12.4, with the position of the light source indicated in each subfigure. Each color represents a unique track traced by the supersmarticle over a single trial.

After performing our analyses across all data sets for the system, linear fits to the log-log plots of the MSD curves were found to have a mean slope of  $1.27 \pm 0.156m^2/s$  for the fully active system and  $1.34 \pm 0.218m^2/s$  for the manually light-directed systems. The MSD plots for the flat smarticles biased by a manually controlled light source are given in Figure 12.5, with the same data plotted on a log-log scale given in Figure 12.3. Each colored line represents the MSD plot for a single supersmarticle track, with the black line representing the mean MSD plot bounded by the gray standard deviation above and below it.

The application of the manually driven light-control algorithm introduces a bias in the diffusive behavior towards the light source, with a slight increase in  $\gamma$ , though the means of both exponents are within a standard deviation of each other.

## 12.2 Light Pipes Smarticles Controlled by Light

The individual tracks for each trial direction can be seen in Figure 12.7. The data for these smarticle cases, contrary to the previously discussed light controlled systems, move *away* from the light source with a mean of  $67.2 \pm 13.9\%$  across all trials. It has been hypothesized that the addition of the light pipes to the smarticle case introduced a new contact geometry which effectively reverses the supersmarticle diffusion behavior.

The MSD plots fits for the unbiased and biased systems yield a mean  $\gamma$  of  $1.32 \pm 0.188m^2/s$  and  $1.15 \pm 0.130m^2/s$ , such that the introduction of the inactive smarticle be-

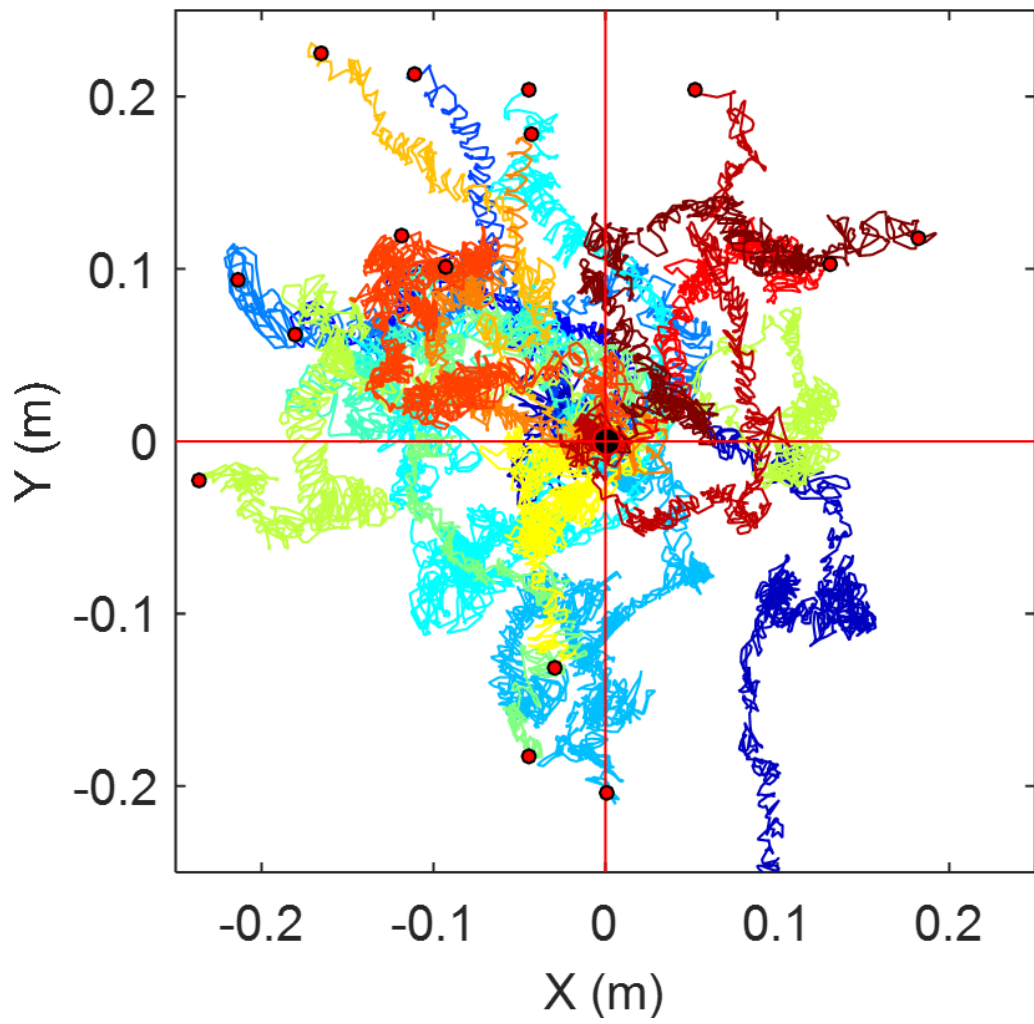


Figure 12.1: Displacement tracks for the unbiased trials with flat faced smarticles

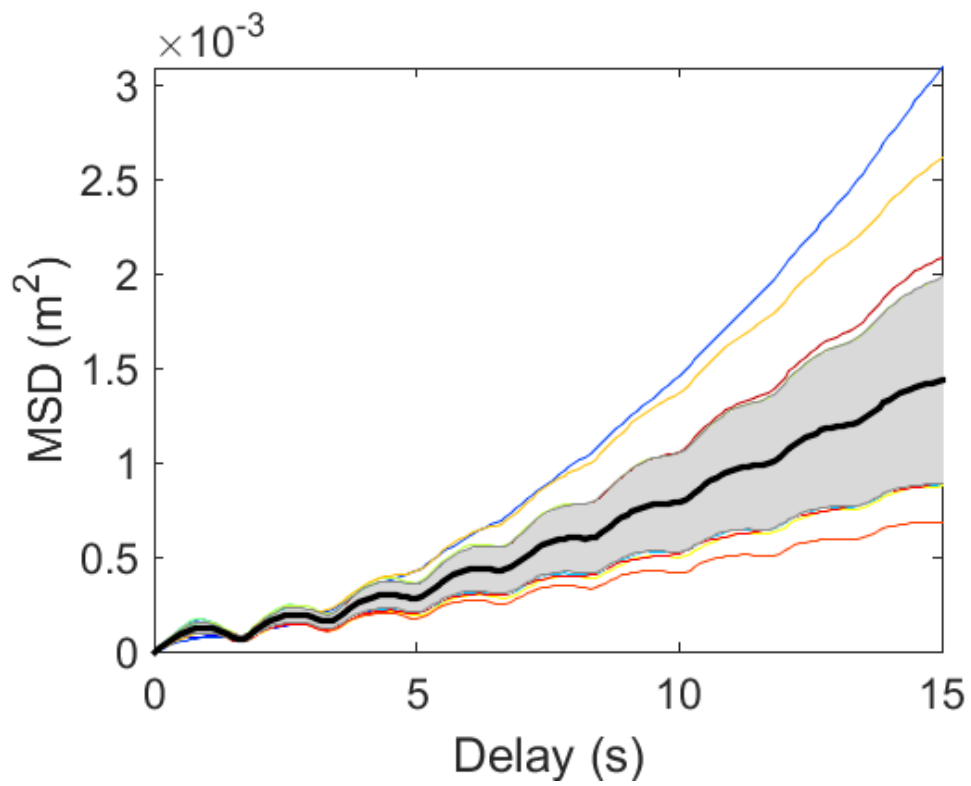


Figure 12.2: MSD plot for unbiased trials with flat faced smarticles

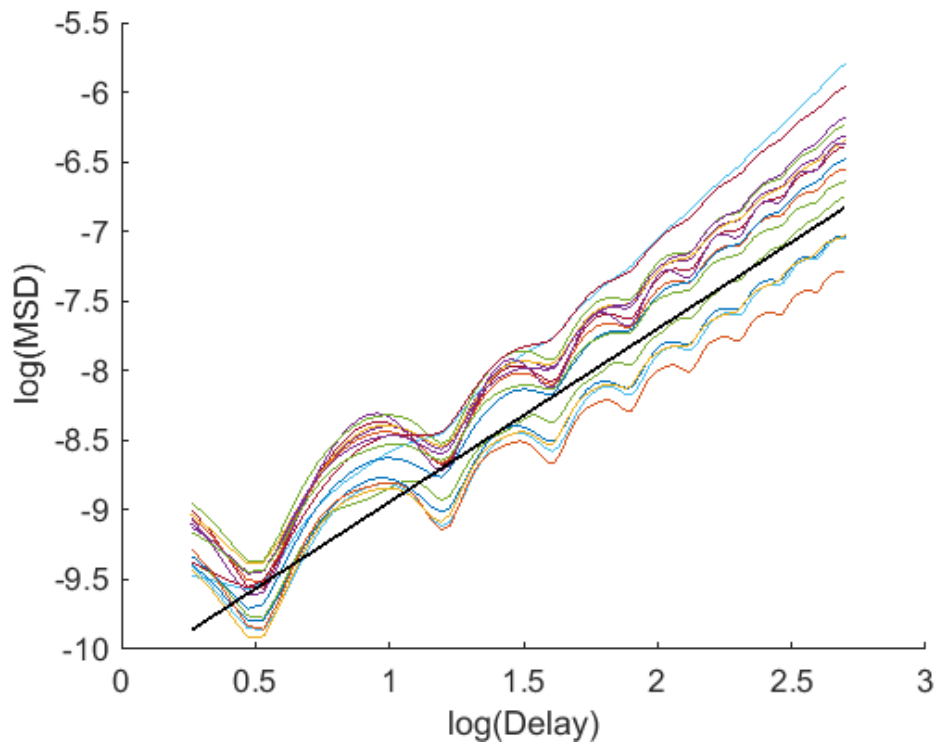


Figure 12.3: MSD log-log plot for unbiased trials with flat faced smarticles. The black line is the linear interpolation of the data; the slope of the linear fit will be the diffusion exponent parameter  $\gamma$ .

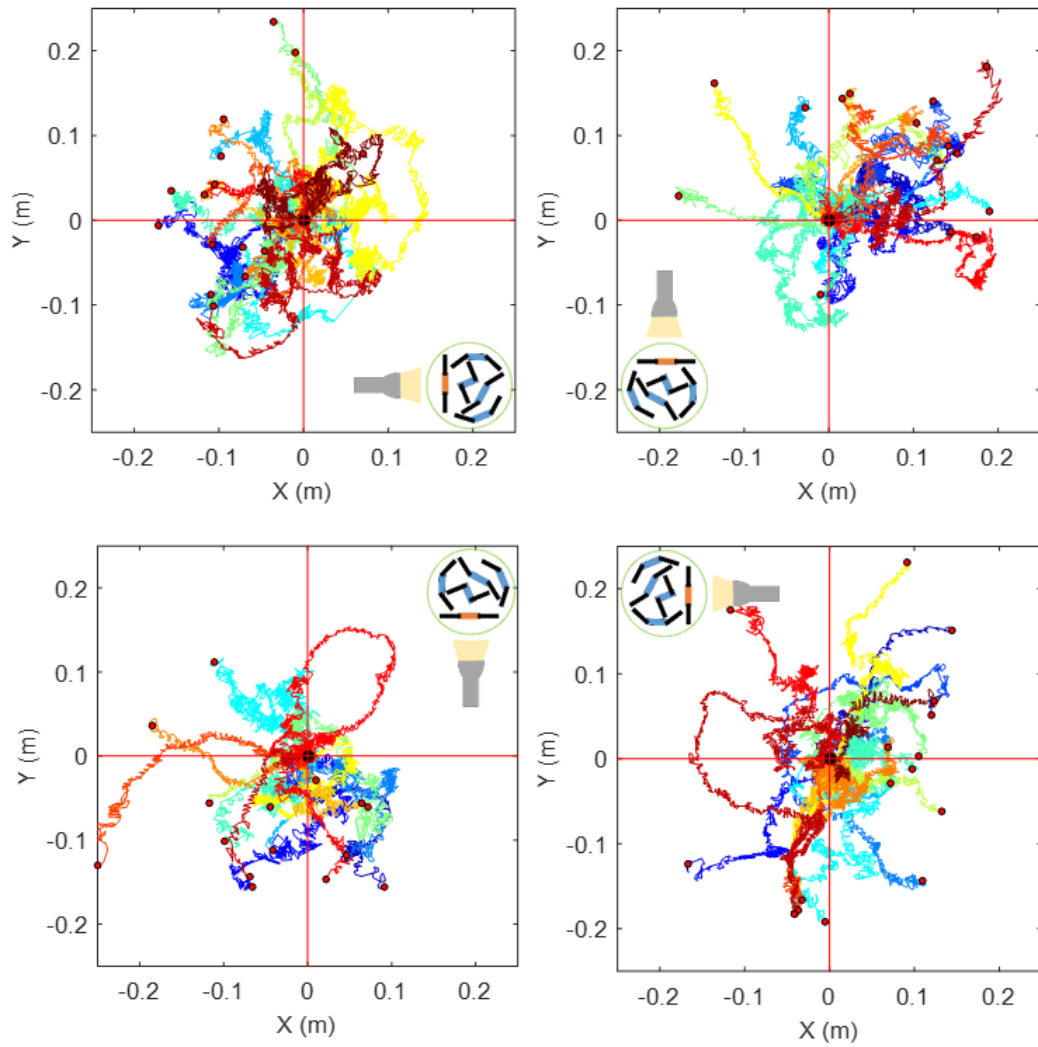


Figure 12.4: Displacement tracks for the manually biased trials with point light source located at four different locations

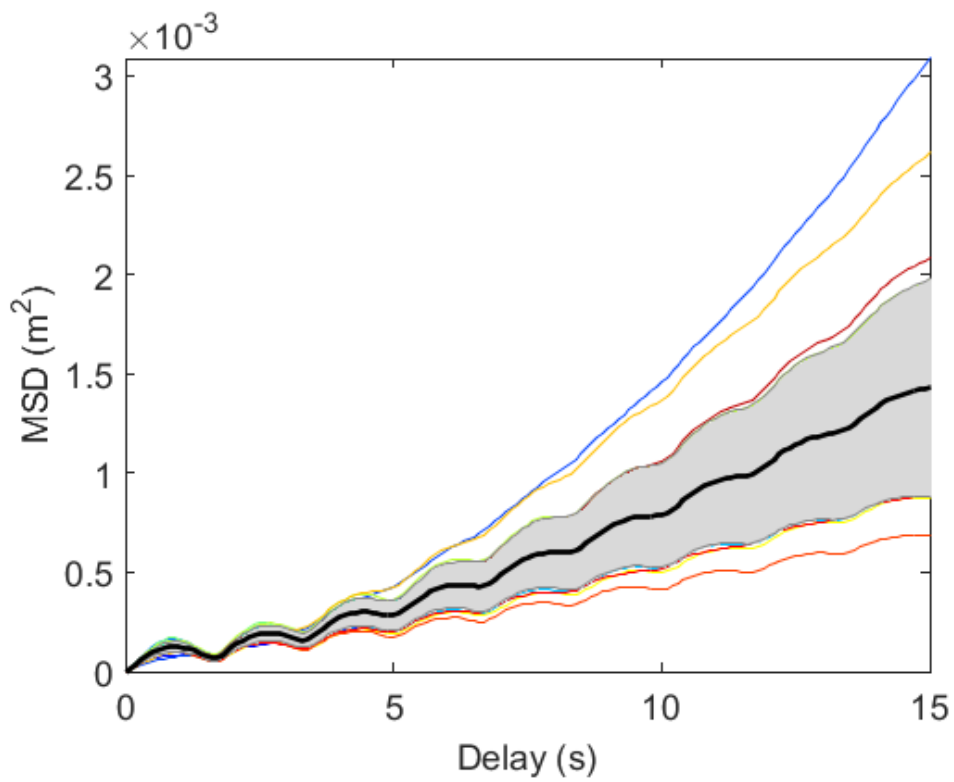


Figure 12.5: MSD plots for all manually biased trials

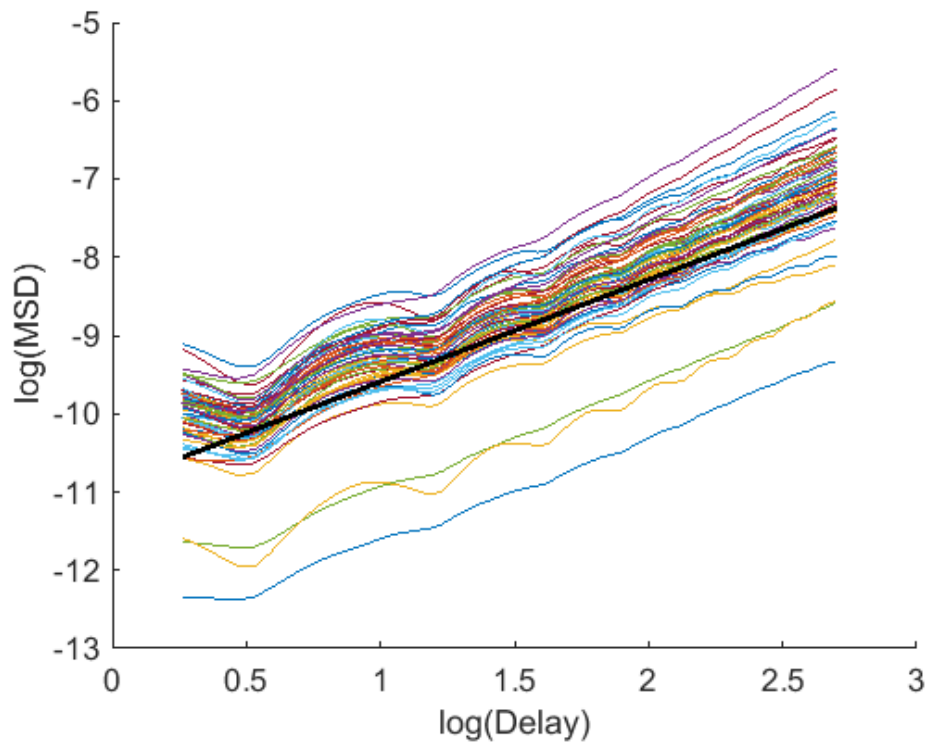


Figure 12.6: MSD log-log plots for all manually biased trials. The MOPs for the biased flat faced supersmarticle systems was found to be  $1.34 \pm 0.218m^2/s$

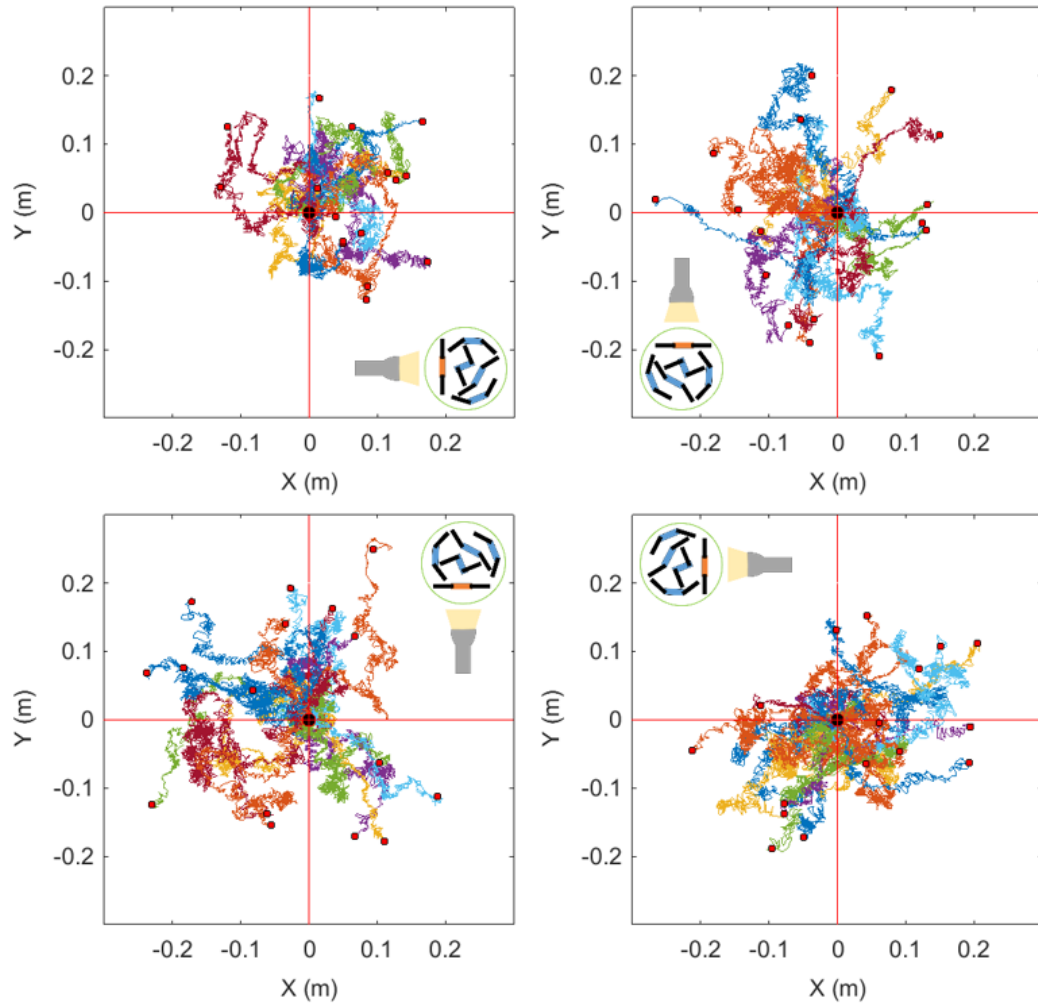


Figure 12.7: Displacement tracks for the light bar biased trials with light source located at four different locations

havior in the ensemble reduces the diffusion exponent, though the values are near a single standard deviation of one another.

### 12.3 Light Pipe Smarticles Controlled by Sound

The sound based control implementation does not provide any immediate insights with regards to consistent system controllability, due to the ability of the inactive smarticle to drift about the supersmarticle system, providing inconsistent drift biases over the course of the trial. Prior to corrections for this internal drift, the supersmarticle did not exhibit any

sort of biased drift. However, when the position of the inactive smarticle is accounted for, using the method discussed in Section 11.2, the biases introduced by the inactive smarticle become apparent. A comparison between the raw tracking data and the corrected data can be seen in Figures 12.8 and 12.9. The correction for the location of the inactive smarticle in the ring shows that the integrated path of supersmarticle in the frame of the inactive smarticle tended to move *away* from instantaneous position the inactive smarticle in 78% of the 78 trials. Furthermore, the MSD analyses were found to yield a system with a mean  $\gamma$  of  $1.27 \pm 0.180$ , such that the supersmarticle continued to exhibit superdiffusive behavior when controlled using sound as an input.

#### 12.4 Flat Smarticles Controlled by Sound

The sound based implementation did not have as profound an effect on the flat faced smarticle cases. Similar to the light pipe smarticles, no obvious biases were seen in the uncorrected tracking data. Furthermore, the implementation of the inactive smarticle frame correction does not divulge the same profound affect of the inactive smarticle seen in the light pipe system, with only a slight change in the biases diffusion statistics which may be categorized either as unbiased or very weakly biased away from the inactive smarticle. Given these results, a different interpretation of the inactive smarticle frame may be more appropriate, though no other methods have been demonstrated to consistently and accurately transform the data. MSD analyses yielded a mean  $\gamma$  of  $1.38 \pm 0.156$ .

Table 12.1: Comparison of Experimental Results

Smarticle Case	Experiment	MOP ( $m^2/s$ )	Diffusion Direction
Flat Face	Unbiased	$1.27 \pm 0.156$	Undirected
Light Pipe (4 smarticles)	Unbiased	$1.30 \pm 0.110$	Undirected
Light Pipe	Unbiased	$1.32 \pm 0.188$	Undirected
Flat Face	Light (Manual)	$1.34 \pm 0.218$	Towards Inactive
Light Pipe	Light (Bar)	$1.15 \pm 0.130$	Opposite Inactive
Flat Face	Sound	$1.38 \pm 0.156$	Opposite Inactive
Light Pipe	Sound	$1.27 \pm 0.180$	Opposite Inactive

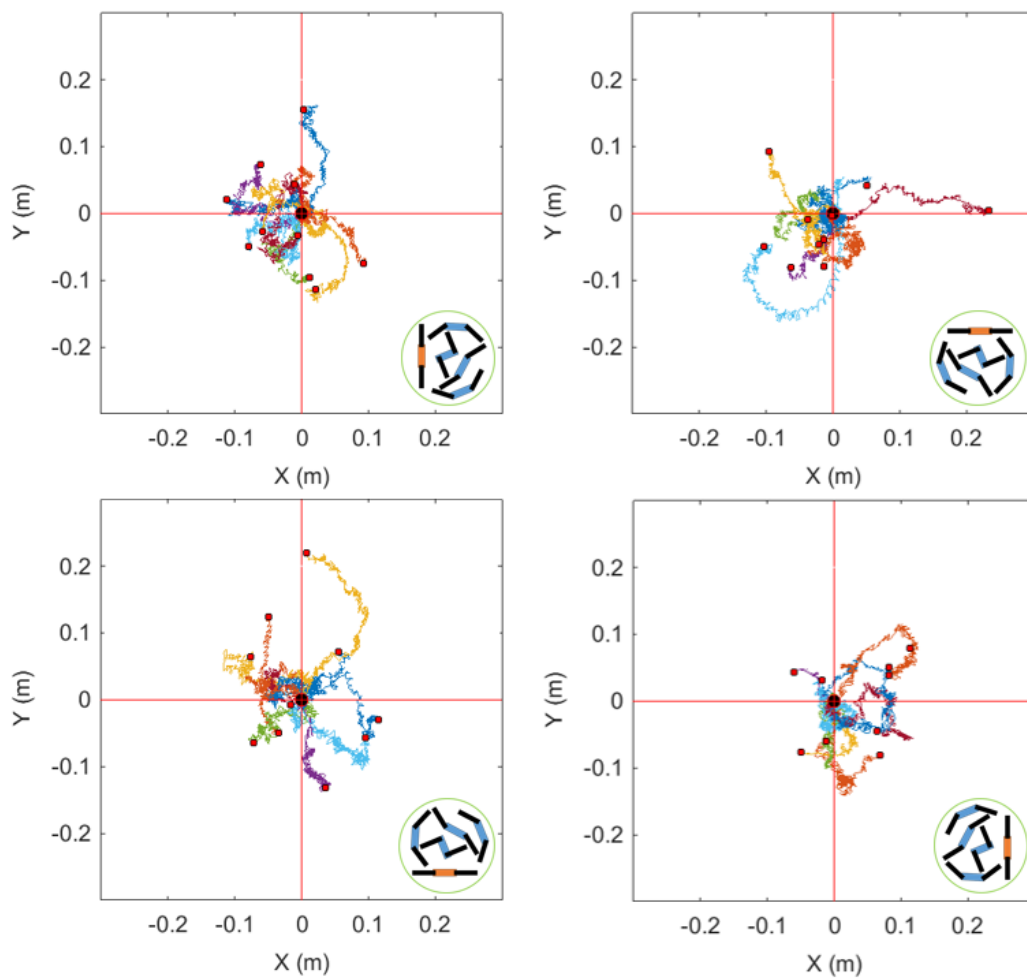


Figure 12.8: Displacement tracks for the sound biased trials with the initial position of the inactive smarticle at four different locations

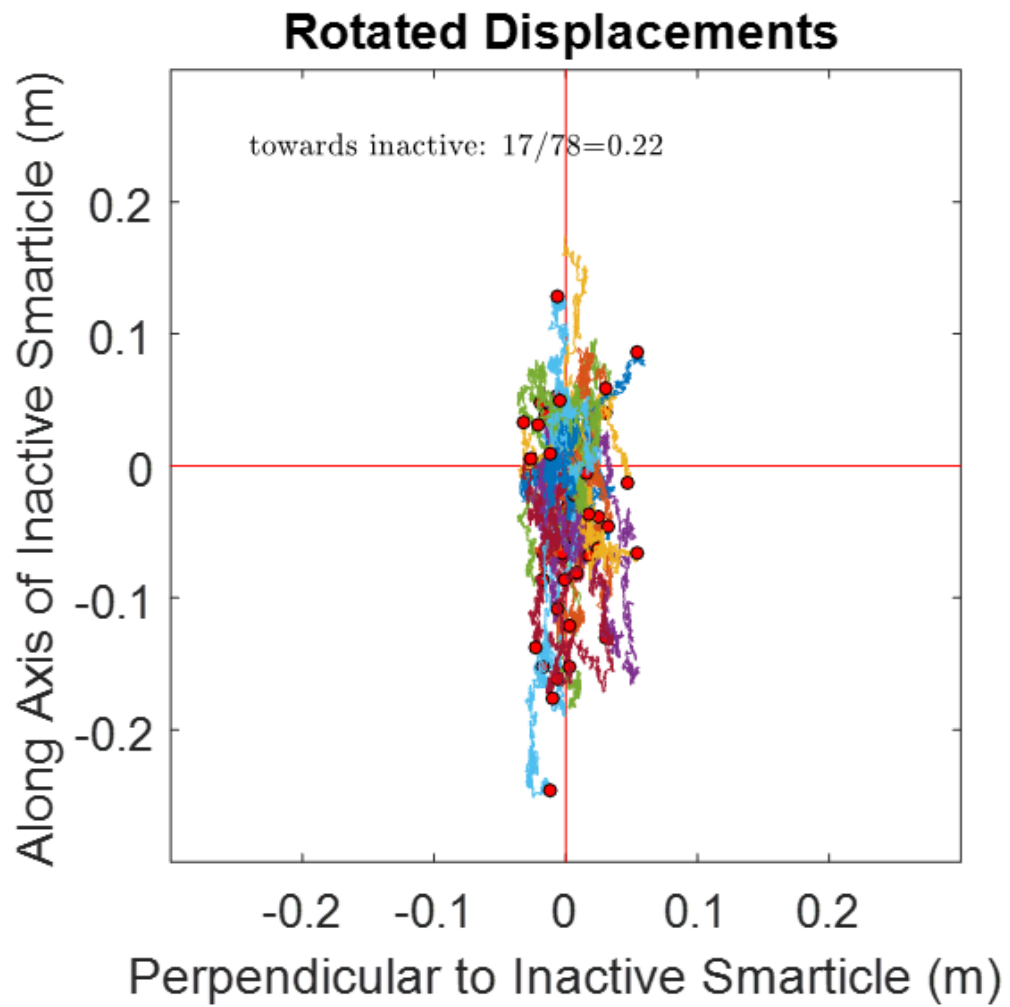


Figure 12.9: Corrected smarticle ring tracks in the frame of the inactive smarticle

## 12.5 Conclusions and Future Works

A comparison between the biased directions between all of the experiments are given in Table 12.1. In the flat face smarticle trials controlled by a manual light source, the supersmarticle systems were found to consistently move towards the light source. However, all of the other systems were found to move in the opposite direction of the inactive smarticle. The reversal in drift bias suggests that the geometry of the active matter has an important effect on the overall ensemble dynamics of the system. Furthermore, there is a difference between the direction of diffusion for the flat face smarticles guided manually by a point light source and the flat face smarticles controlled by sound. This difference is likely attributed to the control schema introduced by the human acting as the controller.

The relatively similar values in the diffusion exponents of the systems, between the unbiased, biased, and even smaller ensembles, demonstrates that the removal of a smarticle or the replacement of an active smarticle with one inactive smarticle does not have a significant effect on the active transport properties of the system, in spite of the fact that the presence of an inactive smarticle can bias the direction of the diffusion.

This second part of the thesis presented the development and use of physically immobile agents in confined active matter systems which exhibit locomotion on the collective scale. The developed smarticles were used in ensembles of confined matters, and the responses of the individuals of the system to external fields have been used to introduce asymmetries in the system, resulting in biased locomotion.

Robophysical studies of the supersmarticle system were demonstrated to probabilistically favor certain directions with respect to the inactive smarticle, which were found to be repeatably consistent for constant control schema and smarticle geometries. In spite of the consistency across trials, the physics which govern the diffusion characteristics are not fully understood. We believe that the presence of the inactive smarticle within the supersmarticle can be approximated as a loose extension of the boundary of the ring, producing

a virtual boundary within the ensemble which is characterized by a collision model that is softer than the normal rigid boundary. This hypothesis is consistent with the literature which has been published for randomly diffusing self-propelled particles [40, 41].

Current research in CRABLab has been focused on probing the underlying system dynamics to refine and develop a more comprehensive understanding of the system interactions between active and inactive particles which generate biased locomotion. Preliminary scans of physical variables such as the masses of the particles and the confining ring and the friction coefficients are have been shown to modulate the diffusive properties of the system. It has also been hypothesized that the interaction behaviors of the particles as they move through their joint space trajectories may lead to various system modes of oscillations characterized by hysteretic displacement loops which lead to the biased locomotion seen in our research.

Reduced 1D models of the supersmarticle system have been developed to explore these hypothesis regarding the physical features which govern the system dynamics. Particles in a confining ring are restricted to movement along a linear track, and reduce the complexity of the system without the loss of the drift phenomenon seen in the 2D system. This new 1D system can be studied experimentally and through physics-based simulations, such that we can sweep the physical and interaction parameter space easily in order to identify the governing variables which characterize the system dynamics and produce biased locomotion.

Other studies will be conducted which utilize the smarticle platform in alternative fashions. Active granular systems of smarticles have a unique ability to entangle and modulate the degree to which entanglement is expressed by actuating the servo arms. Studies which investigate the stress-strain curves of such “chained” ensembles will be used to probe the ability of the smarticle platform to organize into anisotropic sheets with controllable properties.

When the smarticles are oriented with the servo links actuating along an axis parallel to the ground, it is possible for the system to exhibit locomotion. The direction of locomotion

has been found to be consistent for a given given gait, though the physics of the system are not fully understood. Simulations will be developed in the future to elicit the dominating elements of the system, and can be used to inform a system of smarticles which can crawl and flow over one another.

# Appendices

**APPENDIX A**  
**ROBOTIC ANT MINIMUM PARTS LIST**

<b>Item</b>	<b>Vendor</b>	<b>Part Number</b>	<b>Qty</b>	<b>Cost (USD)</b>
Pixy Camera	Unbiased	-	1	69.00
9 DOF IMU	SparkFun	SEN-12636	1	29.95
Mini Plastic Gearmotor HP, D-Shaft	Pololu	1511	2	5.49
HS-5485HB Servo, Extended Rotation	ServoCity	35485S10	2	34.99
640 $\Omega$ resistors (100 pack)	Amazon	-	1	4.49
1.8k $\Omega$ resistors (100 pack)	Amazon	-	1	4.49
3.3k $\Omega$ resistors (100 pack)	Amazon	-	1	4.49
4.7k $\Omega$ resistors (100 pack)	Amazon	100EP5144K70	1	6.16
0.1 $\mu$ F Ceramic Capacitor	SparkFun	COM-08375	2	0.25
200 $\mu$ F Electrolytic Capacitor	RadioShack	2721029	2	0.78
5V Step-Up Voltage Regulator	Pololu	2115	2	3.95
ACS714 Current Sensor	Pololu	1185	1	9.95
MPR121 Capacitive Touch Sensor	SparkFun	SEN-09695	1	7.95
MAG3110 Triple Axis Magnetometer	SparkFun	SEN-12670	1	14.95
3400mAh 3.6V Li-On Battery (2 pack)	Amazon	-	2	26.95
Lipo Charger Basic	SparkFun	PRT-10217	1	7.95
DRV8835 Dual Motor Driver Carrier	Pololu	2135	1	4.49
Solid State Relay	DigiKey	DMO063	1	21.87
microSD Card Reader	SparkFun	BOB-00544	1	3.95
microSD Card	Amazon	-	1	4.95
Arduino Due	Amazon	-	1	44.47
Wheel 42x19mm	SparkFun	ROB-08899	1	6.95
Serial Enabled 16x2 LCD	SparkFun (3.3V)	LCD-09066	1	24.95
Force Sensitive Resistor - Square	SparkFun	SEN-09376	2	9.95
Hall effect	DigiKey	365-1001-ND	2	1.74

The net cost for all components on the new iteration of the robot ant platform is \$429.59. This does not include the cost of 3D printer material as well as other standard items such as perfboard, solder, wires, zip ties, and other small hardware.

**APPENDIX B**  
**SMARTICLE MINIMUM PARTS LIGHT**

<b>Item</b>	<b>Vendor</b>	<b>Part Number</b>	<b>Qty</b>	<b>Cost (USD)</b>
eao SPDT Switch	Mouser	123-09.03201.02	1	1.23
1 $\Omega$ resistors (100 pack)	Amazon	100EP5141R00	1	6.16
10k $\Omega$ resistors (100 pack)	Amazon	100EP51410K0	1	3.64
3.7V LiPo Battery (4 pack)	Amazon	25084X4	1	12.99
ADMP401 MEMS Microphone	SparkFun	BOB-09868	1	9.95
Arduino Pro Mini	SparkFun	DEV-11114	1	9.95
Power HD Sub-Micro Servo HD-1440A	Pololu	1040	2	5.95
Photoresistors	DigiKey	PDV-P9007-ND	2	1.78

The net cost for all components on the smarticle platform is \$59.38. This does not include the cost of 3D printer material as well as other standard items such as perfboard, solder, and wires.

## REFERENCES

- [1] N. Gravish, S. V. Franklin, D. L. Hu, and D. I. Goldman, “Entangled granular media,” *Phys. Rev. Lett.*, vol. 108, p. 208 001, 20 May 2012.
- [2] C. Anderson, G. Theraulaz, and J.-L. Deneubourg, “Self-assemblages in insect societies,” *Insectes Sociaux*, vol. 49, no. 2, pp. 99–110, May 2002.
- [3] P. W. Anderson, “More is different,” *Science*, vol. 177, no. 4047, pp. 393–396, 1972. eprint: <http://science.sciencemag.org/content/177/4047/393.full.pdf>.
- [4] J. Aguilar, T. Zhang, F. Qian, M. Kingsbury, B. McInroe, N. Mazouchova, C. Li, R. Maladen, C. Gong, M. Travers, R. L. Hatton, H. Choset, P. B. Umbanhowar, and D. I. Goldman, “A review on locomotion robophysics: the study of movement at the intersection of robotics, soft matter and dynamical systems,” *Reports on Progress in Physics*, vol. 79, no. 11, 110001, p. 110 001, Nov. 2016. arXiv: 1602 . 04712 [cs .RO].
- [5] J. Buhl, D. J. T. Sumpter, I. D. Couzin, J. J. Hale, E. Despland, E. R. Miller, and S. J. Simpson, “From disorder to order in marching locusts,” *Science*, vol. 312, no. 5778, pp. 1402–1406, 2006. eprint: <http://science.sciencemag.org/content/312/5778/1402.full.pdf>.
- [6] J. K. Parrish, S. V. Viscido, and D. Grnbaum, “Self-organized fish schools: an examination of emergent properties,” *The Biological Bulletin*, vol. 202, no. 3, pp. 296–305, 2002, PMID: 12087003. eprint: <https://doi.org/10.2307/1543482>.
- [7] M. J. B. Krieger, J.-B. Billeter, and L. Keller, “Ant-like task allocation and recruitment in cooperative robots,” *Nature*, vol. 406, no. 6799, pp. 992–995, Aug. 2000.
- [8] Y. Yang, C. Zhou, and Y. Tian, “Swarm robots task allocation based on response threshold model,” in *2009 4th International Conference on Autonomous Robots and Agents*, Feb. 2009, pp. 171–176.
- [9] K. Lerman and A. Galstyan, “Mathematical model of foraging in a group of robots: effect of interference,” *Autonomous Robots*, vol. 13, no. 2, pp. 127–141, Sep. 2002.
- [10] R. T. Vaughan, K. Sty, G. S. Sukhatme, and M. J. Mataric, “Go ahead, make my day: robot conflict resolution by aggressive competition,” in *In Proceedings of the 6th int. conf. on the Simulation of Adaptive Behavior*, MIT Press, 2000, pp. 491–500.

- [11] N. Gravish and D. I. Goldman, “Entangled granular media,” in *Fluids, Colloids and Soft Materials*. John Wiley & Sons, Inc., 2016, pp. 341–354, ISBN: 9781119220510.
- [12] J. R. Howse, R. A. L. Jones, A. J. Ryan, T. Gough, R. Vafabakhsh, and R. Golestanian, “Self-motile colloidal particles: from directed propulsion to random walk,” *Phys. Rev. Lett.*, vol. 99, p. 048 102, 4 Jul. 2007.
- [13] L. Giomi, N. Hawley-Weld, and L. Mahadevan, “Swarming, swirling and stasis in sequestered bristle-bots,” *Proceedings of the Royal Society of London A: Mathematical, Physical and Engineering Sciences*, vol. 469, no. 2151, 2013. eprint: <http://rspa.royalsocietypublishing.org/content/469/2151/20120637.full.pdf>.
- [14] N. Gravish, D. Monaenkova, M. A. D. Goodisman, and D. I. Goldman, “Climbing, falling, and jamming during ant locomotion in confined environments,” *Proceedings of the National Academy of Sciences*, vol. 110, no. 24, pp. 9746–9751, 2013. eprint: <http://www.pnas.org/content/110/24/9746.full.pdf>.
- [15] V. Linevich, “DESIGN OF A ROBOTIC ANT TO MODEL COLLECTIVE EXCAVATION,” Master’s thesis, Georgia Institute of Technology, 2015.
- [16] Arduino, *Arduino Due*, <https://store.arduino.cc/usa/arduino-due>, (Accessed June 30, 2017).
- [17] E. O. Wilson, “Chemical communication in the social insects,” *Science*, vol. 149, no. 3688, pp. 1064–1071, 1965. eprint: <http://science.sciencemag.org/content/149/3688/1064.full.pdf>.
- [18] C. Labs, *Pixy (CMUcam5)*, <http://cmucam.org/projects/cmucam5>, (Accessed June 30, 2017).
- [19] J. L. Gould, “The case for magnetic sensitivity in birds and bees (such as it is): surprising concentrations of magnetite in the tissues of some animals may explain their sensitivity to the earth’s magnetic field,” *American Scientist*, vol. 68, no. 3, pp. 256–267, 1980.
- [20] W. F. Towne and J. L. Gould, “Magnetic field sensitivity in honeybees,” in *Magnetite Biomineralization and Magnetoreception in Organisms: A New Biomagnetism*, J. L. Kirschvink, D. S. Jones, and B. J. MacFadden, Eds. Boston, MA: Springer US, 1985, pp. 385–406, ISBN: 978-1-4613-0313-8.
- [21] Y. camlitepe and D. J. Stradling, “Wood ants orient to magnetic fields,” *Proceedings of the Royal Society of London B: Biological Sciences*, vol. 261, no. 1360, pp. 37–41, 1995. eprint: <http://rspb.royalsocietypublishing.org/content/261/1360/37.full.pdf>.

- [22] E. L. Sandoval, E. Wajnberg, D. M. S. Esquivel, H. L. de Barros, and D. Acosta-Avalos, “Magnetic orientation in solenopsis sp. ants,” *Journal of Insect Behavior*, vol. 25, no. 6, pp. 612–619, Nov. 2012.
- [23] J. B. Anderson and R. K. Vander Meer, “Magnetic orientation in the fire ant, solenopsis invicta,” *Naturwissenschaften*, vol. 80, no. 12, pp. 568–570, Dec. 1993.
- [24] ST, *iNEMO inertial module: 3D accelerometer, 3D gyroscope, 3D magnetometer*, LSM9DS0, Rev. 2, Aug. 2013.
- [25] V. Technology, *FSR Integration Guide & Evaluation Parts Catalog with Suggested Electrical Interfaces*, <https://www.sparkfun.com/datasheets/Sensors/Pressure/fsrguide.pdf>, (Accessed October 17, 2016).
- [26] T. Electronics, *Hallogic Hall-Effect Sensors*, [http://www.ttelectronics.com/sites/default/files/download-files/Datasheet\\_OH090-OHS3100\\_7.pdf](http://www.ttelectronics.com/sites/default/files/download-files/Datasheet_OH090-OHS3100_7.pdf), (Accessed June 30, 2016).
- [27] F. Semiconductor, *Xtrinsic MAG3110 Three-Axis, Digital Magnetometer*, MAG3110, Rev. 9.2, Feb. 2013.
- [28] L. Allegro MicroSystems, *Automotive Grade, Fully Integrated, Hall Effect-Based Linear Current Sensor IC with 2.1 kVRMS Voltage Isolation and a Low-Resistance Current Conductor*, <https://www.pololu.com/file/0J196/ACS714.pdf>, (Accessed November 2, 2016).
- [29] F. Semiconductor, *Proximity Capacitive Touch Sensor Controller*, MPR121, Rev. 4, Sep. 2010.
- [30] P. Corporation, *120:1 Mini Plastic Gearmotor HP, 90° 3mm D-Shaft Output*, <https://www.pololu.com/product/1511/specs>, (Accessed June 30, 2016).
- [31] —, *DRV8835 Dual Motor Driver Carrier*, <https://www.pololu.com/product/2135>, (Accessed June 30, 2016).
- [32] M. T. Inc., *Miniature Single-Cell, Fully Integrated Li-Ion, Li-Polymer Charge Management Controllers*, <https://www.sparkfun.com/datasheets/Prototyping/Batteries/MCP73831T.pdf>, (Accessed June 30, 2016).
- [33] D. Monaenkova, J. Aguilar, V. Linevich, B. Dutta, M. Goodisman, N. Mazouchova, C. Li, R. Maladen, and D. Goldman, “Idle active matter: excavation by confined and crowded environments,” *Science*, In review.

- [34] P. Bardunias and N.-Y. Su, “Dead reckoning in tunnel propagation of the formosan subterranean termite (isoptera:rhinotermitidae),” *Annals of the Entomological Society of America*, vol. 102, no. 1, pp. 158–165, Jan. 2009.
- [35] U. Saranli, M. Buehler, and D. E. Koditschek, “Rhex: a simple and highly mobile hexapod robot,” vol. 20, no. 7, pp. 616–631, Jul. 2001.
- [36] G. A. D. Lopes, R. Babuka, B. D. Schutter, and A. J. J. van den Boom, “Switching max-plus models for legged locomotion,” in *2009 IEEE International Conference on Robotics and Biomimetics (ROBIO)*, Dec. 2009, pp. 221–226.
- [37] M. Hildebrand, “The adaptive significance of tetrapod gait selection,” *American Zoologist*, vol. 20, no. 1, pp. 255–267, 1980.
- [38] N. Tarantino, J.-Y. Tinevez, E. Crowell, B. Boisson, R. Henriques, M. Mhlanga, F. Agou, A. Israël, and E. Laplantine, “TNF and IL-1 exhibit distinct ubiquitin requirements for inducing NEMO–IKK supramolecular structures,” *The Journal of Cell Biology*, vol. 204, no. 2, pp. 231–245, 2014.
- [39] H. Berg, *Random walks in Biology*. Princeton, 1983.
- [40] R. W. A. P. Solon, J. Stenhammar, and M. Kardar, “Pressure and phase equilibria in interacting active brownian spheres,” *Phys. Rev. Lett.*, vol. 114, no. 19, 2015.
- [41] G. Junot, G. Briand, R. Ledesma-Alonso, and O. Dauchot, “Active vs. Passive Hard Disks Against a Membrane : Mechanical Pressure and Instability,” *ArXiv e-prints*, Mar. 2017. arXiv: 1703.04195 [cond-mat.soft].